
Construction of a Caesium Quantum Gas Microscope

Till Mitja Klostermann



München 2021

Construction of a Caesium Quantum Gas Microscope

Dissertation an der Fakultät für Physik
Ludwig-Maximilians-Universität München

vorgelegt von

Till Mitja Klostermann

aus Berlin

München, den 4. Dezember 2021

Tag der mündlichen Prüfung: 14. Februar 2022

Erstgutachter: Prof. Immanuel Bloch

Zweitgutachter: Prof. Hans-Christoph Nägerl

Weitere Prüfungskommissionsmitglieder: Prof. Jan von Delft, Prof. Alexander Högele

Zusammenfassung

In dieser Arbeit beschreibe ich den Aufbau eines neues Quantengasmikroskops. Das Ziel des Experiments ist die Simulation von topologischen Vielteilchensystemen in optischen Gittern. Als Atomspezies wurde aufgrund einer leicht zugänglichen Feshbach Resonanz bei niedrigem magnetischem Feld und seiner großen Feinstrukturaufspaltung Cäsium gewählt. Die Feshbach Resonanz erlaubt die Änderung der Wechselwirkung zwischen den Atomen. Die große Feinstrukturaufspaltung ermöglicht es die Atome in ein anti-magisches Gitter zu laden ohne in der experimentellen Versuchsdauer durch die Photonstreure rate limitiert zu sein. Durch Ramanübergänge zwischen unterschiedlichen Hyperfeinzuständen von Cäsium kann dann ein künstliches Magnetfeld simuliert werden, eine essenzielle Methode für die Realisierung von Chernisolatoren.

Die hohe numerische Apertur die für ein Quantengasmikroskop benötigt wird beschränkt den optischen Zugang zu den Atomen. Dies erschwert den Aufbau der optischen Laserstrahlen zum Kühlen und Manipulieren der Atome. Wir verwenden optischen Transport mithilfe eines laufenden optischen Gitters um die Atome nach einer Vorkühlphase in einen anderen Teil der Vakuumkammer, einer Glaszelle, zu schieben. Dies erlaubt es, die Laserstrahlen die fürs Vorkühlen benötigt werden unabhängig vom Mikroskopobjektiv auf die Atome auszurichten. Das Transportgitter wird durch die Interferenz zwischen einem Gauß-förmigen Laserstrahl und einem Bessel-förmigen Laserstrahl erzeugt. Der Besselstrahl, ein nahezu beugungsfreier Laserstrahl, erlaubt es die Atome über eine 43 cm lange Transportdistanz gegen Gravitation zu halten. Wir transportieren 3×10^6 Atome von der MOT Kammer in die Glasszelle in weniger als 26 ms, ohne dabei die Temperatur zu erhöhen. Die Transporteffizienz ist etwa 75% und durch Gravitation und Atomverluste am Anfang des Transports limitiert.

Sobald die Atome in der Glaszelle ankommen, werden sie in eine gekreuzte Dipolfalle umgeladen. Wir evaporieren indem die Falltiefe reduziert und die Falle gekippt wird. Nach der Kondensation wird das BEC in eine einzelne Ebene eines vertikalen Gitters und darauf folgend in ein horizontales Gitter geladen. Um die Atome durch das Mikroskopobjektiv abzubilden wird Fluoreszenzlicht verwendet. Während der Fluoreszenzabbildung werden die Atome durch optische Molasse gekühlt und die optischen Gitter auf etwa 120 μK vertieft damit die Atome in 1 s um die 25.000 Fluoreszenzphotonen streuen können ohne im Gitter zu tunneln.

Der in dieser Arbeit beschriebene experimentelle Aufbau wird es uns ermöglichen den Einfluss von Wechselwirkungen auf topologische Phasen mit Einteilchenauflösung zu untersuchen. Dies erlaubt es, Annahmen über die mikroskopische Dynamik in diesen Phasen zu testen und unser Verständnis zu vertiefen.

Abstract

In this work I describe the setup of a new quantum gas microscope. The goal of the experiment is the simulation of topological many-body systems in lattices. Caesium was picked as atomic species, because of its easily accessible Feshbach resonance at low magnetic fields and its large fine-structure splitting. The Feshbach resonance allows changing the interaction between atoms. The large fine-structure splitting enables loading the atoms into an anti-magic lattice without limiting the experiment duration via scattering of lattice photons. Using Raman transitions between different hyperfine states of caesium, an artificial magnetic field can be simulated, an essential method for the realization of Chern insulators.

The high numerical aperture necessary for a quantum gas microscope limits the optical access to the atoms. This complicates the setup of the optical laser beams for cooling and manipulating the atoms. We use optical transport based on a running wave optical lattice to transfer the atoms after pre-cooling into a different section of the vacuum system, a glass cell. This allows alignment of the pre-cooling laser beams independent of the microscope objective. The transport lattice is created via interference between a Gaussian laser beam and a Bessel beam. The Bessel beam, a diffractionless laser beam, enables us to hold the atoms against gravity over the transport distance of 43 cm. We transport 3×10^6 atoms from the MOT chamber to the glass cell in less than 26 ms without any temperature increase. The transport efficiency is around 75%, limited by gravity and loss at the start of transport.

After the atoms have arrived in the glass cell they are transferred into a crossed dipole trap. We evaporate the atoms by reducing the trap depth and tilting the trap. After condensation we trap the BEC in a single plane of a vertical lattice. The BEC is subsequently loaded into a 2D horizontal lattice. Fluorescence light is used to image the atoms through the microscope objective. During fluorescence imaging, the atoms are cooled using an optical molasses and the optical lattice depth is increased to around $120 \mu\text{K}$ to allow the atoms to scatter up to 25.000 fluorescence photons in 1 s without tunneling in the lattice.

The experimental setup detailed in this thesis will allow us to study the effects of interactions on topological phases of matter with single particle resolution. This paves the way to testing our assumptions and extending understanding of the microscopic dynamics in these phases.

Contents

1	Introduction	1
2	Why Caesium?	3
2.1	Berry phase	3
2.2	Dipole traps and optical lattices	5
2.3	State dependent lattice	8
2.4	Caesium for interacting topological many-body phases	9
2.4.1	State dependent lattice with Caesium	9
2.4.2	Feshbach resonance	10
3	Experimental Setup	13
3.1	Optical Setup	13
3.1.1	Master laser	14
3.1.2	Repumper laser	17
3.1.3	Raman lattice laser	19
3.1.4	Blue laser	20
3.2	Vacuum system	22
3.2.1	General considerations	22
3.2.2	Oven	23
3.2.3	Zeeman slower	24
3.2.4	MOT chamber	26
3.2.5	Bake-out	27
3.2.6	Glass cell	28
3.2.7	Magnetic field stability and stabilization	31
3.3	Metrology	33
3.3.1	Absorption imaging	33
3.3.2	Time of Flight	33
3.3.3	Trap frequency measurement	34
3.3.4	Microwave spectroscopy	35
3.4	Pre-cooling	37
3.4.1	MOT and Zeeman slower	37
3.4.2	cMOT	38
3.4.3	Molasses	39
3.4.4	Degenerate Raman sideband cooling	39

4	Optical transport	45
4.1	Transport schemes	45
4.2	Transport setup	46
4.2.1	1064 nm Lasers	46
4.2.2	Reservoir	47
4.2.3	Transport lattice	49
4.2.4	Bessel beam	52
4.2.5	Alignment of the transport lattice	57
4.2.6	Magnetic fields during transport	57
4.3	Optical transport	58
4.3.1	Round trip measurements	58
4.3.2	One-way transport	61
5	Evaporation to BEC	63
5.1	Production of a Caesium BEC	63
5.2	Gradient evaporation to BEC	64
5.2.1	Dipole trap	64
5.2.2	Gradient Evaporation	65
5.3	Shallow angle vertical lattice	69
5.4	Upgrade of the setup and new BEC sequence	71
6	Quantum Gas Microscope	73
6.1	Fluorescence imaging	73
6.2	Lattices	74
6.3	Molasses	76
6.4	Objective	77
6.5	Imaging	80
6.6	Reconstruction	82
6.7	Molasses optimization	86
7	Conclusion and Outlook	89
	Appendices	91
A	Classical transport model	91

CHAPTER 1

Introduction

The predictive power of simulation is invaluable to modern life. However, what to do when the computational requirements for simulation become impossible to satisfy? For instance, the difficulty to simulate interacting quantum systems scales exponentially in the system size. One way around this problem is to use a controllable system of quantum particles instead of a classical simulator and map the many-body system of interest on the dynamics of the particles. This approach, quantum simulation, has already yielded numerous exciting results [1–10].

One platform that offers precise control and access to the microscopic observables of the system are quantum gas microscopes [11–17]. In these, neutral atoms are trapped in optical lattices. Tunable interactions [18], control of individual atoms [19] and the potential landscape [20] allow implementation of various many-body Hamiltonians [21]. Single site resolved imaging gives direct access to the parity projected density. Doublon detection (i.e. two particles on one lattice site) has been achieved by separating the doublons into separate layers of a vertical lattice [22–24], or selectively removing singly occupied sites and a single particle from doubly occupied sites [25]. Finally, spin and density resolved imaging is achieved in Ref. [26] by splitting different spins with a magnetic field gradient in a horizontal double well. From the density, information about the dynamics [7], the entanglement [27] or correlations between atoms [12, 26] can be extracted.

Within the field of quantum simulation in general [28–35] and quantum simulation with cold atoms specifically [6, 36–46], one avenue of research that has garnered attention in the past decade is the simulation of topological phases of matter. As opposed to Landau’s theory of phase transitions, where the phases are distinct due to spontaneous symmetry breaking, topological phases are separated by non-local invariants with identical symmetries between the phases. Using ultracold atoms trapped in optical lattices, celebrated models of topological physics, such as the Harper-Hofstadter model [6, 36, 37, 42], the SSH model [38, 40, 41] or the Haldane model [39, 44] can be implemented. Adding interactions between particles to these models can transform the topological properties of these systems in non-trivial ways [43, 47–49], for example turning the collective excitations [50, 51] of the system into anyons, pseudo particles exhibiting neither fermionic nor bosonic statistics [52–55].

Both the Harper-Hofstadter [56, 57] and the Haldane model [58] require complex tunneling between lattice sites. This is often realized via Floquet engineering [59]. In resonant Floquet engineering, tunneling between sites is first suppressed, typically by tilting neighboring lattice sites. Afterwards, a periodic modulation is added to the Hamiltonian to reintroduce tunneling, with a tunneling phase controlled by the parameters of the modulation. However, adding interactions in Floquet systems leads to heating [60, 61]. Jaksch and Zoller [62] proposed a different scheme to implement complex tunneling between lattice sites (see also Refs. [63, 64]). The atoms are loaded into a state-dependent lattice, and tunneling is introduced by two-photon Raman transitions. The complex phase is controlled by the angle and wavelength of the Raman beams. This scheme avoids the heating problems associated with Floquet engineering.

In this thesis I describe the construction of a new quantum gas microscope. We use caesium, which due to a wide Feshbach resonance [18] at low magnetic fields readily lends itself for investigating the effects of interactions on many-body systems. We plan to implement a state-dependent lattice and introduce tunneling between sites with Raman beams to investigate interacting topological systems. By transporting the atoms into a different section of the vacuum system before condensing, we can place the microscope objective close to the atoms without suffering from reduced optical access. This enables a large numerical aperture [12, 15, 16, 65], even at large working distance, so no in-vacuum lenses [11], or hemispheres contacted to the vacuum viewport [13, 66] are required.

The thesis is outlined as follows:

- In the [first chapter](#), I explain why we have chosen caesium for our quantum gas microscope.
- The [second chapter](#) outlines the laser setup for pre-cooling, the vacuum system and the pre-cooling steps before the transport.
- The running wave optical transport is described in the [third chapter](#), which details the loading scheme, measurements on the Bessel beam and the control of the detuning and closes with a discussion of our transport efficiency.
- I proceed in [chapter 4](#) with the description of our evaporation sequence to BEC. Chapter 4 also gives information on our vertical lattice, that is used to constrain the dynamics of the atoms into two dimensions, and the updated evaporation sequence after the experimental setup around the glass cell was upgraded in march 2021.
- Finally, in [chapter 5](#), I discuss the first steps towards fluorescence imaging of single caesium atoms in a pinning lattice using our high resolution imaging setup.

Publications The following publications have been published in the context of this thesis:

- T. Klostermann, C. R. Cabrera, H. von Raven, J. F. Wienand, C. Schweizer, I. Bloch, M. Aidelsburger, *Fast long-distance transport of cold cesium atoms*, Arxiv 2109.03804, submitted to Physical Review A

CHAPTER 2

Why Caesium?

This chapter explains why we set up a Caesium quantum gas microscope experiment. The aim is to study 1D and 2D topological interacting lattice systems. The fact that the systems we want to study are 1D or 2D naturally lends itself to quantum gas microscope experiments [17], which typically also work with 2D lattices. The microscope will then allow direct observation of density correlations [12], from which a trove of information about the many-body system can be deduced (see e.g. Refs. [3, 5, 17, 21]).

The choice to use Caesium has more to do with wanting to study topological and interacting systems [34, 43, 67, 68]. For the latter, Caesium offers tunable interactions even at low magnetic fields using a broad magnetic Feshbach resonance [69]. Concerning the former, some topological systems require time reversal symmetry to be broken (e.g. the quantum Hall effect) [43]. In systems of ultra cold atoms trapped in a lattice, time reversal symmetry can be broken by making the tunnel coupling between lattice sites complex valued. We plan to use a novel scheme to create and control the phase of the tunnel coupling [62–64], utilizing an anti-magic lattice with Raman-assisted tunneling. This makes Caesium an attractive choice, having the largest finestructure splitting among the alkalis.

2.1 Berry phase

The introduction in this subsection largely follows Ref. [43], Section II.B and II.C. Bloch's theorem states that the eigenstates in a crystal can be decomposed into a plane wave with quasi momentum q and a periodic function $u_q^{(n)}$, which has the same periodicity as the unit cell. Here n labels the band index. The Bloch periodic functions $u_q^{(n)}$ are the eigenstates of a Hamiltonian \hat{H}_q , parameterized by the quasi momentum. The eigenvalues $E_q^{(n)}$ of \hat{H}_q form the energy bands of the crystal. If the lowest band remains gapped, a continuous, adiabatic variation of the quasi momentum will transform an eigenstate $u_{q_i}^{(n)}$ at quasi momentum q_i into one at q_f , $u_{q_f}^{(n)}$. If $q_i = q_f$, i.e. traversing the Brillouin zone along a closed contour, the final state differs from the initial one only by a phase factor

$$u_{q_f}^{(n)} = \exp \left[i \left(\phi_{\text{dyn}}^{(n)} + \phi_{\text{geo}}^{(n)} \right) \right] u_{q_i}^{(n)}, \quad (2.1)$$

with dynamical phase $\phi_{\text{dyn}}^{(n)} = -\frac{1}{\hbar} \int_{t_i}^{t_f} E_q^{(n)}(t') dt'$ and geometric or Berry phase $\phi_{\text{geo}}^{(n)} = \oint u_q^{(n)} \partial_q u_q^{(n)} dq$. The Berry phase [70, 71] allows the distinction between different topological phases, as illustrated below. The Berry phase can be rewritten as the integral over the Berry connection $\mathbf{A}^{(n)} = i u_q^{(n)} \partial_q u_q^{(n)}$ or, provided that the Brillouin zone is two dimensional, the flux of the Berry curvature $\Omega_{ij}^{(n)} = \partial_{q_i} A_j^{(n)} - \partial_{q_j} A_i^{(n)}$ through the area bounded by the loop.

The quasi momentum is periodic, i.e. $\hat{H}_q = \hat{H}_{q+G}$ with G a reciprocal lattice vector. In 1D the transformation $q \rightarrow q + G$ therefore corresponds to a closed loop and the Berry phase along the loop is called Zak's phase $\phi_{\text{Zak}} = \int_q^{q+G} i u_q^{(n)} \partial_q u_q^{(n)} dq$. Zak's phase [38, 72] can for instance be used to

characterize the different phases of the 1D SSH model [73, 74]. The 1D SSH model is a tight binding model with two sites (orbitals) per unit cell (and subsequently two bands¹)

$$\hat{H}_{\text{SSH}} = - \sum_j \left(J' \hat{a}_j^\dagger \hat{b}_j + J \hat{a}_j^\dagger \hat{b}_{j-1} + \text{h.c.} \right). \quad (2.2)$$

The sum runs over all sites j of the 1D chain. It exhibits two topologically distinct phases, depending on the ratio of J/J' , with the transition at $J = J'$. At the transition point the band gap closes, so an adiabatic transformation of the Berry phase becomes impossible. This is a generic feature of topological insulators, and allows the definition of an equivalence partition, with two Hamiltonian being topologically equivalent if they can be transformed into each other by varying their parameters without closing the energy gap. In the case of the 1D SSH model, Zak's phase differs by π between the two phases. Because the value of Zak's phase in the 1D SSH model depends on the choice of basis for the sub lattice, only differences between topological phases for a given sub lattice basis are physically meaningful, and it is not meaningful to distinguish a topologically trivial phase from a non-trivial one [38]. This distinction becomes possible when the SSH chain has a finite length, as in this case the system has a boundary with a topologically trivial phase (the vacuum). Generically, at the boundary between two topologically distinct phases, edge modes occur [75]. So the existence or lack of an edge mode localized to the boundary of the chain allows the differentiation between the topologically trivial and non-trivial phase [41, 45, 73, 76]. The SSH model has been implemented in cold atoms using, for example, optical super lattices [38], momentum space lattices [41], chirped amplitude lattices [40] and tweezer arrays [45]. Ref. [38] measured the Zak phase difference between the two distinct phases. Ref. [41] observe the edge mode at the corners of the SSH model, while the authors of Ref. [40] create an interface between the two SSH model phases and observe the edge mode at the interface. Finally, Ref. [45] studies the bosonic many-body SSH-model and observes symmetry protected topological edge modes.

In two dimensions, it becomes possible to define the Berry curvature. The integral of the Berry curvature over the full Brillouin zone is quantized in multiples of 2π [77], i.e.

$$\mathcal{C}^{(n)} = \frac{1}{2\pi} \int_{\text{BZ}} \Omega^{(n)}(\mathbf{q}) d^2q \in \mathbb{Z}. \quad (2.3)$$

$\mathcal{C}^{(n)}$ is called the Chern number, defined for each band n . In two dimensions, the Chern number is zero if the Hamiltonian is time-reversal symmetric. For charged particles magnetic fields can be used to break time reversal symmetry, as is done for example in the quantum Hall effect. However, as ultra-cold atoms are charge neutral this is not an option. Instead, artificial magnetic fields can be created by making the tunneling between sites complex valued. The complex phase of the tunnel coupling is analogous to Peierls phases [78, 79] of electrons in a solid subject to a magnetic field [57]. The dynamics of non-interacting atoms in a lattice with complex tunneling is described by the (Harper-)Hofstadter Hamiltonian (Ref. [56, 57], given here in tight binding formulation as in [43], Eq. 45):

$$\hat{H}_{\text{HH}} = -J \sum_{j,m} \left(e^{2\pi i \alpha m} a_{j+1,m}^\dagger a_{j,m} + a_{j,m+1}^\dagger a_{j,m} + \text{h.c.} \right) \quad (2.4)$$

with the phase $2\pi\alpha$ picked up while tunneling around a plaquette and j, m labeling sites in the x, y direction. Adding on-site interactions the resulting Hamiltonian becomes the Harper-Hofstadter-Hubbard Hamiltonian. The Hofstadter Hamiltonian may be thought of as a lattice analog of quantum Hall liquids, with the topological insulator phases referred to as Chern insulators. Similarly, adding on-site interactions is believed to result in fractional Chern insulators, lattice analogs of fractional quantum Hall states [80–82].

¹This is the minimum number of bands/orbitals required for a non-zero Berry phase.

λ (nm)	767	1064	1534	871.1, π -pol	871.1, σ^+ -pol
$-\frac{\alpha}{2\epsilon_0 c} \left(\frac{\text{nK}}{\text{W/cm}^2} \right)$	3.4	-2.4	-1	-7.5	1.5

Table 2.1 | Example polarizabilities of the $|F = 3, m_F = 3\rangle$ state of Caesium. 1064 nm is the laser wavelength used for the dipole traps in the experiment and the running wave lattice. 767 nm and 1534 nm lasers are planned for superlattice potentials and 871.1 nm is planned to be used for an antimagic lattice. A negative sign indicates atoms are trapped in intensity maxima

To induce complex tunnel couplings in optical lattices, Floquet engineering can be used (e.g. Refs. [6, 36, 37, 44, 46]). One issue with Floquet engineering of topological band structures is that interactions tend to lead to heating [83, 84]. We hope to address this issue by engineering the complex tunneling using a state dependent lattice and Raman transitions between different spin states [62].

2.2 Dipole traps and optical lattices

Ref. [62] proposes to trap atoms in an anti-magic optical lattice. Before the scheme is described in detail in section 2.3, I briefly want to explain how optical lattices are created. Given an electric field $E = E_0 \cos(kz - \omega t) = E_0^+ e^{i(kz - \omega t)} + E_0^- e^{-i(kz - \omega t)}$, with intensity $I = 2\epsilon_0 c |E_0^+|^2 = \frac{1}{2}\epsilon_0 c |E_0|^2$ the dipole potential seen by an atom is given by $V = -\alpha \frac{I}{2\epsilon_0 c}$ [85], with α the polarizability of the atoms at the laser wavelength λ , ϵ_0 the permittivity of vacuum and c the speed of light. For alkali atoms, with the detuning from resonance $\Delta = \omega_L - \omega_0$ much larger than the hyperfine splitting of the excited state ($\Delta \gg \Delta'_{HFS}$), the polarizability of a ground state atom in $|F, m_F\rangle$ is given as [85]

$$\alpha = -\frac{\pi\epsilon_0 c^3 \Gamma}{\omega_0^3} \left(\frac{2 + \mathcal{P}g_F m_F}{\Delta_{2,F}} + \frac{1 - \mathcal{P}g_F m_F}{\Delta_{1,F}} \right). \quad (2.5)$$

Here g_F is the Landé factor ($g_{F=3} = -1/4$ and $g_{F=4} = 1/4$ for the ground state of Cs), \mathcal{P} is the laser polarization ($\mathcal{P} = 0, \pm 1$ for π, σ^\pm light), Γ the linewidth and $\Delta_{2,F}$ and $\Delta_{1,F}$ are the detuning from the D2 and D1 line respectively (see Table 2.1 for explicit values of the polarizability for some wavelengths relevant for the experiment). For a Gaussian laser beam with waist in the focus w_0 , wavelength λ and Rayleigh range $z_R = \frac{\pi w_0^2}{\lambda}$, the intensity in the focus is given by $I_0 = \frac{2P}{\pi w_0^2}$. Close to the center, the radial profile is approximately quadratic in r . Atoms trapped in the focus of a Gaussian laser beam therefore experience a harmonic confinement with trap frequency

$$\omega = \sqrt{\frac{-2\alpha I_0}{\epsilon_0 c m \omega_0^2}}. \quad (2.6)$$

Optical Lattices Two counter-propagating laser beams at the same wavelength interfere and create an optical lattice. For atoms trapped in this lattice, the potential is given by

$$V = \frac{\alpha}{2\epsilon_0 c} \left| \sqrt{I_1} e^{i(kz - \omega t)} + \sqrt{I_2} e^{i(-kz - \omega t)} \right|^2 = \frac{\alpha I_1}{2\epsilon_0 c} + \frac{\alpha I_2}{2\epsilon_0 c} + 2 \frac{\alpha \sqrt{I_1 I_2}}{2\epsilon_0 c} \left(1 - 2 \sin^2(kz) \right) \quad (2.7)$$

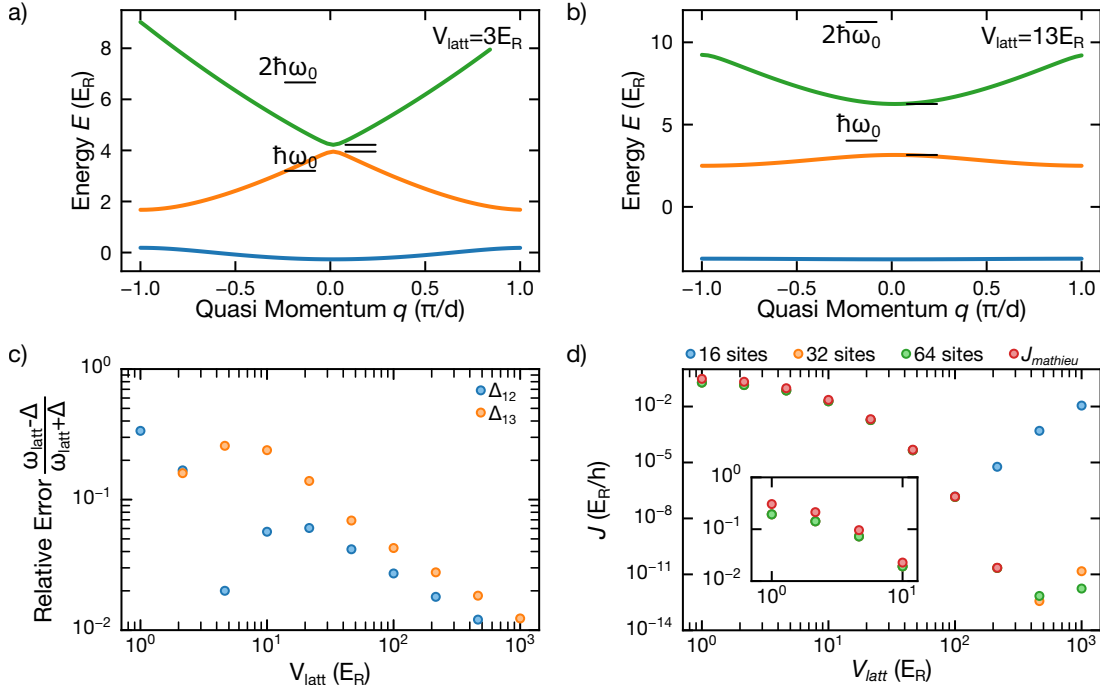


Figure 2.1 | a) Bandstructure for $V_{\text{latt}} = 3E_R$ and b) for $V_{\text{latt}} = 13E_R$. The first and second excited state from the harmonic oscillator approximation ω_{latt} (see Equation 2.8) are quite different to the energy difference at $q = 0$. c) Relative error $\varepsilon = 2((n-1)\omega_{\text{latt}} - \Delta_{1n})/((n-1)\omega_{\text{latt}} + \Delta_{1n})$, with ω_{latt} computed according to Equation 2.8 and $\hbar\Delta_{1n}$ the energy difference between the first and n th band at $q = 0$. Note that ω_{latt} underestimates Δ_{12} for low lattice depth and overestimates it for large ones. d) Tunnel coupling J extracted from the numerically computed bandwidth for different sizes of \hat{H}_{FT} (Equation 2.10, sampling per site = number of sites). Red shows the tunnel coupling estimate from the Mathieu equation. For large trap depth, the size of \hat{H}_{FT} becomes critical. At this point, the approximation of J via the Mathieu equation is fairly accurate and faster.

with $k = 2\pi/\lambda$ the lattice wavevector. The lattice depth V_{latt} and lattice trap frequency ω_{latt} are given by

$$V_{\text{latt}} = 4 \frac{\alpha}{2\epsilon_0 c} \sqrt{I_1 I_2}, \quad \omega_{\text{latt}} = \sqrt{\frac{2V_{\text{latt}} k^2}{m}}. \quad (2.8)$$

Note that for small trap depths, the anharmonicity of the sinusoidal potential becomes important and the energy spacing between bands deviates from $\hbar\omega_{\text{latt}}$ (Figure 2.1). Figure 2.1c shows the relative error $(n\omega_{\text{latt}} - \Delta_{1n})/(n\omega_{\text{latt}} + \Delta_{1n})$ between the harmonic approximation to the trap frequency ω_{latt} and the band gap Δ_{1n} at $q = 0$. $n = 2, 3$ labels the excited band. For small lattice depths ($V_{\text{latt}} < 10E_R$) the difference is on the order of 6-30%. The comparison is with the bandgap at $q = 0$ because this is the modulation frequency relevant for amplitude modulation to measure lattice depths (subsection 3.3.3). An optical lattice is also created if the lasers interfere at an angle. With α the half opening angle between the beams, k in the equations above should be replaced with $k = 2\pi \sin(\alpha)/\lambda$, which gives a lattice spacing of $d_{\text{latt}} = \sin(\alpha)\lambda/2$.

Degenerate atoms loaded into an optical lattice can be used to simulate the low-energy physics of condensed matter models. To this end, the full dynamics of the system get approximated by a tight binding model. This model captures the essential features of the system relevant at low energies e.g. tunneling between lattice sites or interaction between atoms on the same site. Numerical values for the coupling between sites or the on-site interaction can be extracted from the Schrödinger equation for non-interacting atoms trapped in an optical lattice. This system is identical to that of non-interacting

electrons trapped in a solid. As such, we can use Bloch's theorem to separate the wavefunction into a plane wave of quasi momentum q and a Bloch periodic function $u_q^{(n)}$, labeled by the quasi momentum and the band index n . The band structure of the optical lattice $E_q^{(n)}$ can then be determined by solving the Schrödinger equation for the Bloch periodic function u_q . Following the derivation given in Ref. [86] Section 3.1.3 we write:

$$\hat{H}_q u_q^{(n)} = \left(\frac{(\hat{p} - q)^2}{2m} - \frac{1}{4} V_{\text{latt}} (2 + e^{i2kz} + e^{-i2kz}) \right) u_q^{(n)} = E_q^{(n)} u_q^{(n)}. \quad (2.9)$$

Discrete Fourier transformation of the equation above yields

$$\hat{H}_{FT} c^{(n,q)} = E_q^{(n)} c^{(n,q)}, \quad (2.10)$$

with \hat{H}_{FT} an $N \times N$ matrix having the ℓ -th entry on the diagonal $(2\ell + q/\hbar k)^2 E_R$ and first off diagonal entries $-1/4V_{\text{latt}}$. Note that the dimension of \hat{H}_{FT} implicitly discretizes a single lattice period into N points. Numerically diagonalizing Equation 2.10 for all q gives the Bloch bands $E_q^{(n)}$. With increasing lattice depth, N has to be increased for accurate determination of the band structure (Figure 2.1d). The Bloch periodic function $u_q^{(n)}$ is related to $c^{(n,q)}$ via an inverse Fourier transformation. From the Bloch periodic function $u_q^{(n)}$, the Wannier function centered on site i can be found as $w(x - x_i) = \mathcal{N} \sum_q e^{iq(x-x_i)/\hbar} u_q^{(n)}$ with \mathcal{N} chosen such that $|w(x - x_i)|^2 = 1$.

From the ground state energy band, the tunneling matrix element J between adjacent sites i and j can be computed from the first energy band's width W or the Wannier function $w(x - x_i)$ as [86, 87]

$$J = \int w(x - x_i) \left(\frac{p^2}{2m} + V(x) \right) w(x - x_j) dx = \frac{W}{4} \approx \frac{4E_R}{\sqrt{\pi}} \left(\frac{V_{\text{latt}}}{E_R} \right)^{3/4} \exp \left[-\sqrt{\frac{4V_{\text{latt}}}{E_R}} \right]. \quad (2.11)$$

The approximation in Equation 2.11 is due to the Mathieu equation and becomes accurate for large lattice depth (Figure 2.1d). $E_R = \hbar^2 k^2 / 2m$ in Equation 2.11 is the lattice recoil energy, where $k = 2\pi \sin(\alpha) / \lambda$ (see paragraph below Equation 2.8). The onsite interaction can be computed as

$$U = \frac{4\pi\hbar^2 a}{m} \int |w_x(x) w_y(y) w_z(z)|^4 dx \approx \sqrt{\frac{2m\hbar a^2}{\pi}} \sqrt{\omega_{\text{latt}}^{(x)} \omega_{\text{latt}}^{(y)} \omega_{\text{latt}}^{(z)}}, \quad (2.12)$$

with $\hbar\omega_{\text{latt}}^{(i)}$ the energy difference between first and second band along axis i and a the scattering length. $w_i(x)$ is the Wannier function in the direction i , centered on an arbitrary site. For a 2D lattice these will be different in the horizontal and vertical direction. $w_i(x)$ is reasonably well approximated by a harmonic oscillator wavefunction (Ref. [87] Table I) with Δ_{12} the excitation frequency from the first to the second band as the oscillator frequency.

Using J and U , we can rewrite the Hamiltonian for the low temperature dynamics of the atoms using a single-band tight binding model (i.e. no atomic internal degrees of freedom or sub-structure to the unit cell). For the specific example given here, this tight binding model corresponds to the Bose-Hubbard model [1, 88]

$$\hat{H}_{\text{Hubbard}} = -J \sum_{\langle i,j \rangle} \hat{a}_i^\dagger \hat{a}_j + \frac{U}{2} \sum_i \hat{n}_i (\hat{n}_i - 1) - \sum_i (\epsilon_i - \mu) \hat{n}_i \quad (2.13)$$

with $\langle i, j \rangle$ indicating that the sum should be over nearest neighboring sites, \hat{a}_i^\dagger (\hat{a}_i) the creation (annihilation) operator on site i , $\hat{n}_i = \hat{a}_i^\dagger \hat{a}_i$ the number operator and ϵ_i an energy offset on site i and μ the chemical potential. In the experiment, the energy offset is given by the harmonic confinement of

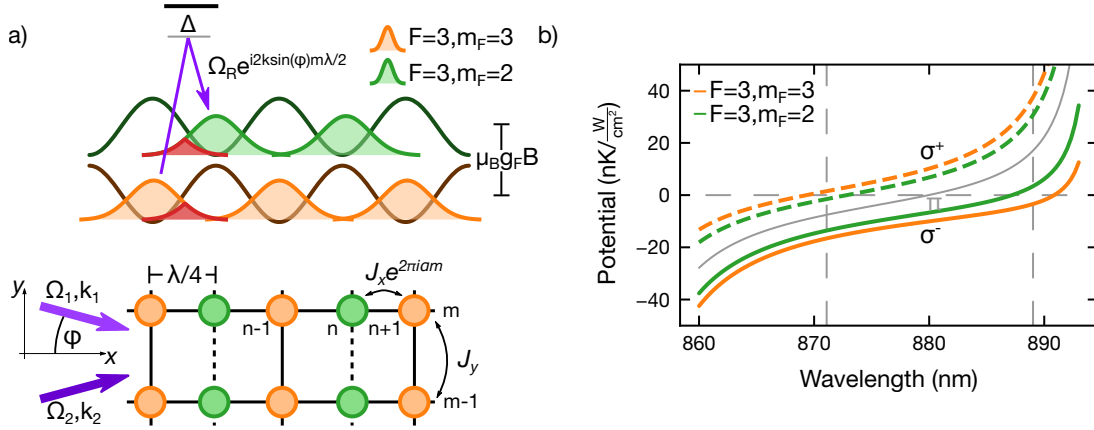


Figure 2.2 | a) Sketch of Raman induced tunneling in an anti-magic wavelength lattice (wavelength λ). Atoms in $|F = 3, m_F = 3\rangle$ (orange) and $|F = 3, m_F = 2\rangle$ (green) sit in the minima and maxima of the optical lattice respectively. Tunneling between nearest neighbor sites can be induced using microwaves or a pair of Raman beams (detuning Δ) to drive transitions (Rabi frequency Ω_R) between the different internal states. The figure illustrates the case of Raman induced tunneling. While hopping, the atoms gain a phase $2\pi am = 2k \sin(\varphi)m\lambda/2$ dependent on the wavelength of and angle φ between the Raman beams (Ω_1, k_1 and Ω_2, k_2). The tunneling amplitude J_x depends on the overlap between adjacent sites (red). Contrary to Ref. [62], there is no tilt of the lattice. b) Light shift of $|F = 3, m_F = 3\rangle$ (orange) and $|F = 3, m_F = 2\rangle$ (green) for different wavelengths and polarization. The grey vertical dashed lines indicate the anti-magic wavelengths for σ^+ (green and orange dashed lines) and σ^- (green and orange solid lines). The grey solid line between the curves corresponds to the light shift with π -polarized light.

the atoms in the lattice. Let $\epsilon_i = 0$ for now and the mean density in the lattice be $n \in \mathbb{N}$ atoms per site. In this case the model exhibits a phase transition when varying J/U . For large J/U , the system is superfluid, for small J/U the system becomes a Mott insulator [1, 12, 89, 90]. In the Mott insulator phase, the fluctuations in the on-site occupation are suppressed and each site is occupied by n atoms. To observe this transition, precise tuning of the chemical potential to reach n would be required. In the experiment, the harmonic confinement ϵ_i leads to a smooth variation of the local chemical potential. As a result, the Mott insulator becomes observable as a density plateau of constant filling without precise tuning of μ . For dense clouds, multiple shells of constant filling become observable, with decreasing site occupation towards the edges. Each shell is separated from the others by a superfluid layer. These superfluid layers are also where the entropy of the system is concentrated.

2.3 State dependent lattice

From Equation 2.5 it is clear that the dipole potential of an atom depends on its internal state (F, m_F), i.e. different ground states experience different light shifts. Given two different internal ground states $|g_1\rangle$ and $|g_2\rangle$, the wavelength can be chosen such that the light shift for one ground state disappears (*tune out wavelength*), the light shift is the same for both states (*magic wavelength*) or the light shift is exactly opposite (*anti-magic wavelength*). We are planning to implement an optical lattice at the anti-magic wavelength in our experimental setup. This allows us to induce tunneling between adjacent lattice sites using microwaves or Raman transitions ([62], Figure 2.2a). During the Raman induced tunnelling, the atom gains a phase factor, which is given by the wavelength and angle between the two Raman beams. This phase factor is analogous to a Peierls phase that tight binding electrons gain when hopping in a lattice pierced by a magnetic flux. Therefore, using Raman-assisted tunneling, artificial magnetic fields can be introduced into the system. More precisely, let the Raman coupling between the anti-magic

lattices sites be $\Omega_R = \frac{\Omega_1\Omega_2}{\Delta} e^{i(\mathbf{k}_1-\mathbf{k}_2)\mathbf{x}} = \frac{\Omega_1\Omega_2}{\Delta} e^{iqy}$, where $\Omega_{1,2}$ is the Rabi frequency of the first (second) Raman beam, Δ the detuning of the lasers from the excited state and we have chosen the angles between the beams and the lattice such that the wavevector difference projected along the anti-magic lattice axis is zero ($(\mathbf{k}_1 - \mathbf{k}_2)\mathbf{x} = qy$, as in Ref. [62]). The tunneling matrix element between the sites is given by $\langle n-1, m | \Omega_R | n, m \rangle = \frac{1}{2} \int \mathbf{w}^*(\mathbf{x}-\mathbf{x}_{n-1,m}) \Omega_R \mathbf{w}(\mathbf{x}-\mathbf{x}_{n,m}) d^3x$. Since the optical lattice potential separates ($\mathbf{w}(\mathbf{x}-\mathbf{x}_{n-1,m}) = w_x(x-x_{n-1})w_y(y-y_m)w_z(z)$, tunneling along x), this can be rewritten as [62]:

$$\langle n-1, m | \Omega_R | n, m \rangle = \frac{1}{2} \Omega_R \Gamma_y(\alpha) \Gamma_x e^{2\pi i \alpha m} = J_x e^{2\pi i \alpha m}, \quad (2.14)$$

with $\alpha = q\lambda/4\pi$ and

$$\Gamma_x = \int w_x^*(x) w_x(x - \lambda/4) \quad (2.15)$$

$$\Gamma_y(\alpha) = \int w_y^*(y) w_y(y) \cos(4\pi\alpha y/\lambda). \quad (2.16)$$

The complex tunneling phase $2\pi\alpha m$ can be tuned by varying \mathbf{q} , the wavevector difference between the two Raman beams (Figure 2.2a).

While the setup described above in shown in Figure 2.2a allows complex tunneling with a tunable phase, it does not implement the Harper-Hofstadter-Hamiltonian (Equation 2.1). The same Raman laser pair driving transitions from $n \rightarrow n+1$ also drives transitions from $n+1 \rightarrow n+2$. However, the phase picked up during tunneling from n to $n+1$, $\phi_{n \rightarrow n+1}$ is the negative of the one picked up when tunneling from $n+1$ to $n+2$, i.e. $\phi_{n \rightarrow n+1} = -\phi_{n+1 \rightarrow n+2}$, or $\phi_{\text{even} \rightarrow \text{odd}} = -\phi_{\text{odd} \rightarrow \text{even}}$. Intuitively, this is because the order of the virtual Raman lasers is reversed. The one driving the virtual excitation in case of a transition from even to odd sites drives the virtual deexcitation for the odd to even transition. This role reversal inverts the sign of q and thereby α and ϕ . The flux, the phase difference picked up while traveling around a plaquette, implemented with the scheme is called staggered, i.e. it reverses sign between even and odd columns. A system with staggered flux has zero Chern number. For a non-zero Chern number, the flux needs to be rectified [6]. To rectify the flux and have $\phi_{\text{even} \rightarrow \text{odd}} = \phi_{\text{odd} \rightarrow \text{even}}$, Ref. [62] proposes to tilt the potential, while Ref. [64] proposes using a superlattice (implemented for instance in [6] with Floquet engineering to produce the complex tunneling). Finally, Ref. [63] suggests using three internal states instead of two. Notably, all the schemes have in common that at least two pairs of lasers, driving independent Raman transitions are required.

2.4 Caesium for interacting topological many-body phases

2.4.1 State dependent lattice with Caesium

Off-resonant photon scattering in an optical lattice leads to heating and limits the lifetime of the atoms in the lattice. The off-resonant photon scattering Γ_{sc} can be expressed in terms of the dipole potential depth V as $\Gamma_{\text{sc}} \propto \Delta^{-1}$ with the detuning from the resonance Δ [85]. At constant trap depth, the scattering rate decreases with increasing detuning. For an anti-magic lattice, this detuning cannot be chosen, since the wavelength is fixed by the anti-magic condition of the polarizability. For the alkali-metal atoms, the anti-magic wavelength will typically lie between the D_1 and D_2 transition. The maximum detuning Δ therefore depends on the finestructure splitting between the D_1 and D_2 line, which increases with the charge of the nucleus. For this reason, the finestructure splitting is largest in Caesium among the alkali-metal atoms. Specifically, the splitting is 42 nm (17 THz) in Caesium, compared to 15 nm (7 THz) in ^{87}Rb .

This makes Caesium a very attractive choice for an anti-magic lattice experiment. Specifically,

we are planning to use the hyperfine states $|F = 3, m_F = 3\rangle$ and $|F = 3, m_F = 2\rangle$, because they have a small differential Zeeman shift and are thus less susceptible to magnetic field fluctuations. The anti-magic wavelength for these states is at 871 nm for σ^+ -polarized light and at 889 nm for σ^- -polarized light (Figure 2.2b). There is no anti-magic wavelength for π -polarized light, as the light shift is identical for the two states (for π -polarized light $\mathcal{P} = 0$ in Equation 2.5). Among these two wavelengths, 889 nm provides a stronger lightshift, so less power would be required for the same lattice depth. However, the associated scattering rate is also necessarily stronger, which is why we plan to use 871 nm for our state dependent lattice.

Using 871 nm light with a laser power of 100 mW and waists of $300 \times 45 \mu\text{m}^2$ gives an optical lattice with bare ($F = 3, m_F = 3 \rightarrow F = 3, m_F = 3$) tunneling of $J = 2\pi \times 1$ Hz and a lattice depth of $30 E_R$. The off-resonant scattering rate is around 500 mHz. With a pair of Raman beams detuned from the $6S_{1/2}, F = 3 \rightarrow 6P_{3/2}, F = 2$ transition of 500 GHz, a power of 20 mW and a circular waist of $250 \mu\text{m}$ gives an induced coupling between the $F = 3, m_F = 3$ and $F = 3, m_F = 2$ states of 430 Hz. The off-resonant scattering rate is 2 Hz. Working with the Raman beams closer to the D_1 line (500 GHz from $6S_{1/2}, F = 3 \rightarrow 6P_{1/2}, F = 2$ transition) gives comparable coupling (460 Hz) with lower off-resonant scattering rate (0.5 Hz). This coupling can be compared to tunneling achieved in Floquet systems. Ref. [6] realizes the Hofstadter model with Floquet engineering. The induced coupling is 75 Hz. Ref. [59] reports an induced coupling of 270 Hz in a ladder system and Ref. [44] uses induced couplings on the order of 500 Hz to study the Haldane phase.

A different kind of state dependent lattice is used in Refs. [91, 92]. The experiments use Caesium in states $|F = 4, m_F = 4\rangle$ and $|F = 3, m_F = 3\rangle$. The wavelength is chosen such that it is a tune-out wavelength for $|F = 4, m_F = 4\rangle$ when the light is σ^- polarized and close to a tune-out wavelength for $|F = 3, m_F = 3\rangle$ if the light is σ^+ polarized². In the experiments, this kind of lattice is used to simulate quantum random walks. Note that a similar lattice has also been implemented for ^{87}Rb [94]. A magic-wavelength dipole trap [95] for Caesium in any of the $S_{1/2}$ or $P_{3/2}$ states was implemented in Ref. [96].

2.4.2 Feshbach resonance

Apart from the large fine structure splitting, Caesium is also interesting because it allows tuning the interacting strength between the atoms using a Feshbach resonance. In this subsection, I give a very brief introduction into Feshbach resonances [18]. At low temperatures the scattering cross section σ between bosons is determined by the s-wave scattering length a : $\sigma = 8\pi a^2$. Odd partial wave contributions vanish for bosons and higher even partial waves (e.g. d and g) do not contribute because the centrifugal barrier prevents collisions [69]. The value of the scattering length a_{bg} (in the absence of a Feshbach resonance) depends on the depth of the (s-wave) molecular potential between the scattering atoms [97], and diverges if the potential has a depth that admits a bound state at the continuum threshold.

Feshbach resonances allow tuning of the interaction between atoms. They occur when the unbound, scattering atoms (open channel) have an energy close to a bound molecular state (closed channel) of a different internal state configuration [18, 69]. If the free atoms couple to the molecular state, for example via relativistic spin-spin interactions, the scattering length diverges when the energy difference between the bound state and the scattering state is zero (Figure 2.3a–b). While the open channel is limited to only s-waves due to the low temperature, the closed channel can be made of higher partial waves of even symmetry.

The scattering length of Caesium at low magnetic fields is dominated by a large s-wave Feshbach resonance at -11.7 G [18] with the zero crossing of the resonance at 17.12 G [98]. This enables easy tuning of the scattering length over a range of a few hundred Bohr radii a_0 at low magnetic fields. In addition,

²This is possible for these states since they are close to stretched states, i.e. $|F = 4, m_F = 4\rangle$ has $m_J = 1/2$ and $|F = 3, m_F = 3\rangle$ has mostly $m_J = -1/2$. See Ref. [93], section 5.1 for a more detailed explanation

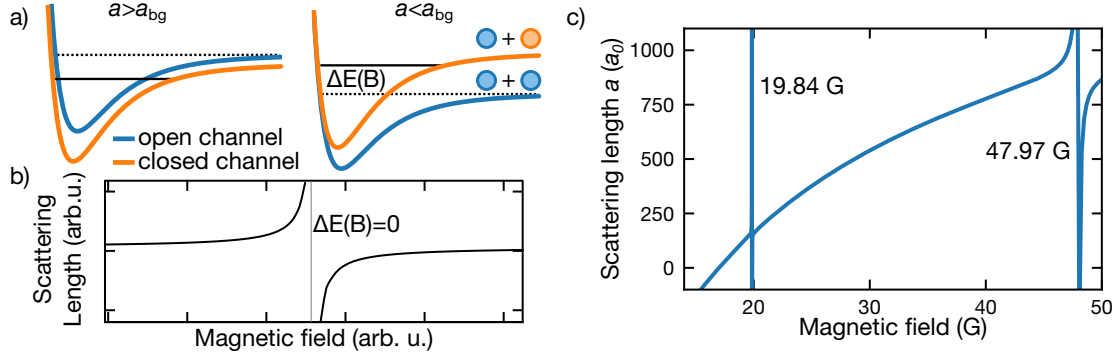


Figure 2.3 | **a)** Energy of the scattering channel (blue) and a molecular bound state (orange) versus magnetic field. Insets show the molecular potentials. The dotted line in the inset is the energy of the scattering atoms, the solid line the energy of the bound state. **b)** At the energy crossing of the scattering channel and the molecular state the scattering length diverges. **c)** Scattering length versus magnetic field for the $|F = 3, m_F = 3\rangle$ state of Caesium. The magnetic fields of the Feshbach resonances are indicated. At 17.12 G the scattering length is zero [98]. The resonances at 19.84 G and 47.97 G are listed in Ref. [18], Table IV.

two narrower resonances at magnetic fields relevant to our experiment, at 19.84 G (g-wave molecular potential) and 47.97 G (d-wave molecular potential) exist (see Ref. [18], Table IV and Figure 2.3c).

We condense Caesium in its absolute ground state ($F = 3, m_F = 3$), where two-body inelastic collisions are forbidden. As a result, the dominant loss channel in our experiment are three-body collisions. For large scattering length and low temperatures, a universal relation between the three-body recombination coefficient α_{rec} and the scattering length a exists (Ref. [99], Sec. 5.2.2). This relation is typically expressed in terms of the three-body loss rate³:

$$L_3 = n_l \alpha_{\text{rec}} = n_l C(a) \hbar a^4 / m, \quad (2.17)$$

and was measured in experiment in Refs. [100–102]; n_l is the number of atoms lost in a recombination process and usually $n_l = 3$ is assumed [103]. The factor $C(a)$ modifies the regular $L_3 \propto a^4$ scaling of the loss rate and is due to Efimov physics [104, 105] (see e.g. Ref. [103] for a measurement of Efimov resonances using Caesium and Refs. [106–109] for more recent experiments). The Efimov physics lead to an enhanced three-body loss rate at certain negative scattering lengths and a reduction of the loss rate at certain positive scattering lengths. The first of these minima is at $B \approx 21$ G where $a = 210 a_0$. This minimum of the scattering length is important during evaporation of Caesium (see chapter 5).

The expression for L_3 becomes invalid for very large and very small absolute values of the scattering lengths [105]. At very large values, the recombination rate (and scattering cross section) is limited by unitarity [18]. At very small values, comparable to the range of the two-body potential, the scattering properties depend sensitively on the precise form of the scattering potential. This range is typically given as the van der Waals length $\ell_{\text{vdW}} = \frac{1}{2} \left(\frac{2mC_6}{\hbar^2} \right)^{1/4}$ (see Ref. [18] section B.1). The van der Waals length is larger in Caesium ($\ell_{\text{vdW}} = 101 a_0$, [18], Table I) than in other alkali atoms, which implies that the scaling of the L_3 coefficient starts to deviate from the expected scaling at higher scattering lengths. The result is an unusually large three-body loss rate at low scattering lengths ($L_3 \approx 3 \times 10^{-28} \text{ cm}^6/\text{s}$), which makes condensation more difficult.

³Or the three-body recombination rate $K_3 = 2\sqrt{3}\alpha_{\text{rec}} \approx 3.5\alpha_{\text{rec}}$

CHAPTER 3

Experimental Setup

This chapter gives an overview of the experimental setup up to the optical transport. It starts out by detailing the laser setup for pre-cooling in [section 3.1](#). [Section 3.2](#) describes the full vacuum system, including the glass cell. [Section 3.3](#) explains some of the ways in which we measure observables in our system. Finally, the chapter closes in [section 3.4](#) with a description of the pre-cooling before transport.

3.1 Optical Setup

We have three lasers used for pre-cooling, running on the D2 line of Caesium ($6S_{1/2} \rightarrow 6P_{3/2}$, [Figure 3.1](#)). The master laser is locked to the $F = 4 \rightarrow F' = 5$ transition, the repumper is detuned by close to 9.2 GHz and repumps atoms from $F = 3$ during the MOT, compressed MOT and molasses phases and to polarize the atoms during the degenerate Raman sideband cooling (dRSC) stage. The repumper is offset-locked to the master. An additional injection locked laser system creates the light for the Raman lattice used during dRSC, one free-running grating based external cavity diode laser (ECDL) with a small linewidth but low power and another high power laser diode that is injection locked by the low power ECDL. These lasers and their optical setup are described in detail in the following.

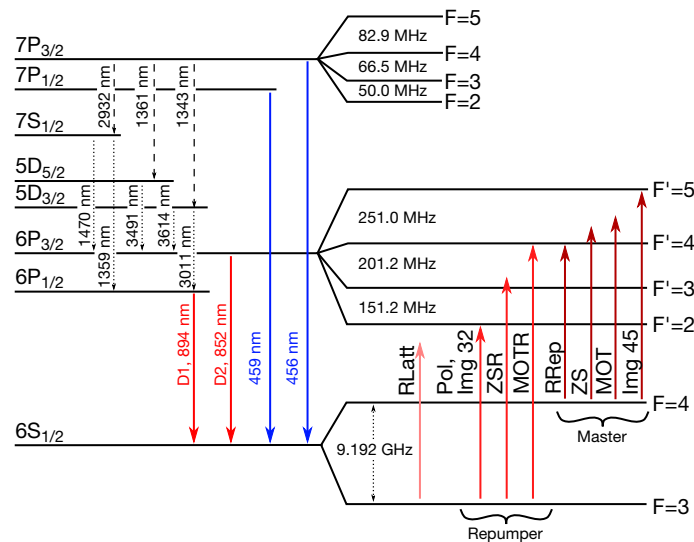


Figure 3.1 | Level scheme of Caesium up to the $7P_{3/2}$ manifold [110, 111]. RLatt = Raman Lattice, Pol = Polarizer, ZSR = Zeeman slower repumper, MOTR = MOT Repumper, RRep = Raman Repumper, ZS = Zeeman slower cooler, MOT = MOT cooler, Img = Imaging

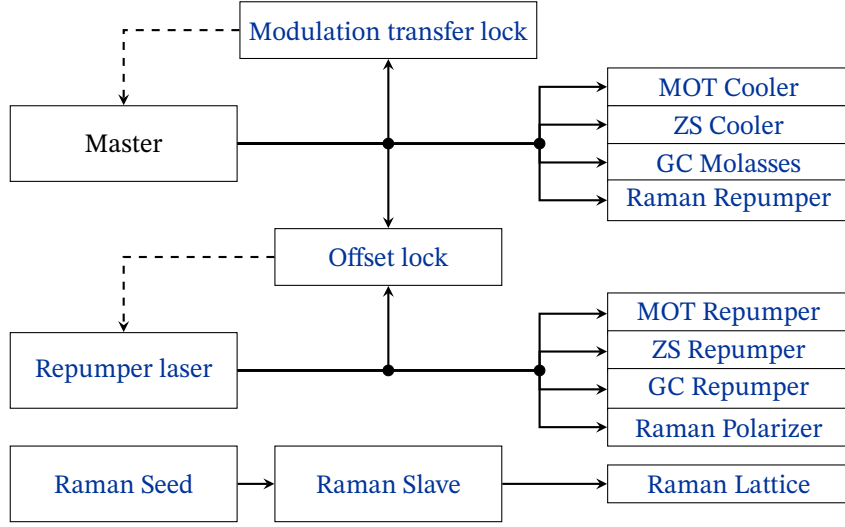


Figure 3.2 | Overview of the lasers used for pre-cooling and imaging of the atoms. GC = Glass cell

3.1.1 Master laser

Figure 3.3 sketches the setup for the master laser used for the cooling in the Zeeman slower and the MOT, and repumping during dRSC. For the master laser we use a Toptica DLPro laser¹. The laser has an output power of around 50 mW and an elliptical beam profile. After removing the ellipticity using a cylindrical telescope, the power is split into four arms, one for locking the laser to a spectroscopy cell, one for a repumper running on $F = 4 \rightarrow F' = 4$ used during dRSC, one for imaging on the $F = 4 \rightarrow F' = 5$ transition and one to seed a tapered amplifier (TA).

Modulation transfer lock, $F = 4 \rightarrow F' = 5$

We lock the laser to a Cs spectroscopy cell using modulation transfer spectroscopy [112–114], with our setup in particular described in [115]. Similar to saturated absorption spectroscopy, we split the beam in two and send the two beams, called pump and probe, through the spectroscopy cell from opposite directions. The probe is then focused on a photodiode. Contrary to regular saturated absorption spectroscopy, we send the pump through an electro-optic modulator (EOM)² driven with a 3 MHz RF signal before it passes through the spectroscopy cell. The EOM generates sidebands on the pump beam at $f \pm 3$ MHz. On an atomic resonance, four-wave mixing replicates these sidebands on the probe (hence modulation transfer spectroscopy) [116]. Focusing the probe on a photodiode leads to a beat of the probe with its sidebands.

The phase of the 3 MHz beat signal encodes information about the detuning of the probe from resonance. Therefore, a phase detection circuit may be used to produce an error signal [113–115]. To this end we high-pass filter the photodiode signal to remove the DC signal, send it through a delay line (in this case a 10 m coaxial cable) and mix it with a copy of the 3 MHz RF signal that was sent to the EOM. This gives a DC signal which around the resonance has a linear, negative slope ideal for locking the laser via a PID controller.

The modulation transfer only happens when the sub-Doppler resonance condition [114], $v = \Delta\omega/2k$, is satisfied, where $\Delta\omega$ is either zero on an atomic transition or the frequency difference between two

¹Laserdiode: EYP-RWE-0860-06010-1500-SOT02-0000, EYP

²EO TFL3-NIR, Qubig

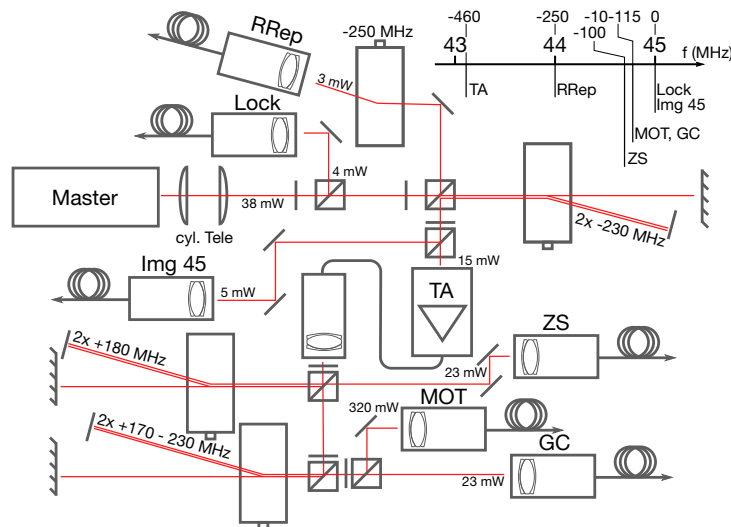


Figure 3.3 | Sketch of the master laser setup. The top right inset shows the relative frequency detuning of the different lasers generated from the master laser. Some representative laser powers at different positions throughout the setup are indicated. These were taken in November 2021.

transitions on a crossover peak. Therefore, the background of the error signal is flat. The non-linear four-wave mixing is strongest on the closed $F = 4 \rightarrow F' = 5$ resonance, where the master laser is locked.

Figure 3.4 shows a sketch of the setup used to create the modulation transfer locking signal and the inset in the same figure shows both the saturated absorption signal as well as the modulation transfer signal after phase detection. The laser is locked to the zero crossing of the modulation transfer signal.

The 3 MHz frequency signal is delivered from a DDS chip (Direct Digital Synthesis Chip³). The 3 MHz are split for the delay line lock and the EOM and the EOM signal is amplified by a 28 dBm gain RF amplifier⁴.

Raman repumper, $F = 4 \rightarrow F' = 4$

The Raman repumper is used to repump atoms from $F = 4$ back into $F = 3$ during the degenerate Raman sideband cooling (dRSC) stage (see subsection 3.4.4). It runs on the $F = 4 \rightarrow F' = 4$ resonance, which is -200 MHz detuned from the $F = 4 \rightarrow F' = 5$ resonance the laser is locked to. We bridge the frequency gap using a 200 MHz acousto-optic modulator (AOM)⁵. During dRSC only very little repumper light is required, typically less than 1 mW is sufficient. Increasing the repumper power does not decrease the atom number or increase the temperature after dRSC. Note that even without the repumper dRSC works, but slightly worse, i.e. afterwards fewer atoms remain.

The frequency for the AOM is supplied by a DDS chip (as is the case for almost all AOMs used in the lab). This frequency is then amplified with an in-house developed RF amplifier box housing a Minicircuits amplifier and additional electronics to toggle the output and control the RF power sent to the AOM. Up to 2 W of RF power can be supplied by the AOM driver. This is lower than the optimum for the used AOM model, but sufficient for us.

³AD9910, Analog Devices

⁴ZFL-1000H, Minicircuits

⁵MT250-B100A0,5-800, AA Opto-Electronic

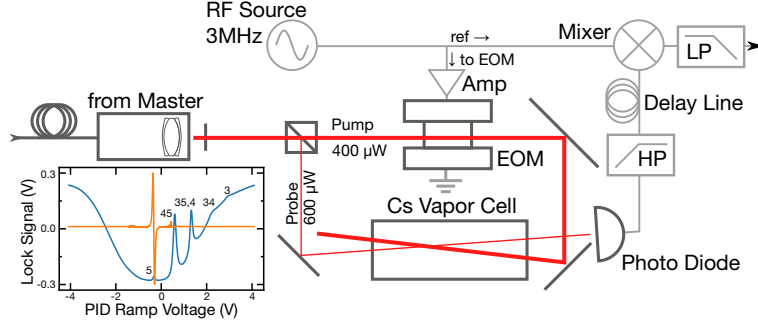


Figure 3.4 | Sketch of the master locking setup. The pump passes through the EOM. On resonance the modulation gets imprinted on the probe in the Cs vapor cell. The photodiode records the modulation and via a delay line and mixer the lock signal (orange curve in inset) is generated. The blue curve in the inset shows the saturated absorption signal. The Lamb dip of the $F = 4 \rightarrow F' = 5$ transition is barely visible. The PID Ramp Voltage is proportional to the master laser frequency. The labels next to the absorption signal peaks indicate the associated resonance, with crossover resonances labeled as 34, 35 and 45. The 35 and $F = 4 \rightarrow F' = 4$ resonances overlap in the plot. The lock signal voltages refer to the orange lock signal. The powers indicated for pump and probe were optimized for the best lock signal and measured in November 2021. LP = low pass filter, HP = high pass filter.

Imaging light, $F = 4 \rightarrow F' = 5$

Due to the transport we need imaging light at different positions around the experiment table. It has also proven to be invaluable to have imaging along more than one axis, preferably two perpendicular ones. Additionally, we want to be able to image at zero magnetic field (during time of flight for instance) but also at high magnetic fields (for in-situ imaging of the BEC for example). Due to the Zeeman shift of the atomic states, we therefore need to be able to tune the imaging frequency over a range of tens of MHz. We use a set of two double-pass AOMs (DPAOMs, [117]) for this. The first one shifts the frequency by 2×-230 MHz, the second one shifts it back close to the $F = 4 \rightarrow F' = 5$ resonance.

In the double pass AOM setup the first diffracted order is retro reflected back through the AOM. A lens between the AOM and the retro mirror (not shown in Figure 3.3), placed a distance of one focal length from each, compensates changes in the diffraction angle with RF frequency. By overlapping the first diffracted order of the retro-reflection with the incoming beam, the AOM frequency can be tuned over a wide range without significant changes in the pointing of the first diffracted order of the retro-reflected beam. The frequency shifted beam can therefore be fiber coupled and sent to the experiment chamber, and the frequency can be tuned over a range of tens of MHz without complete loss of the fiber coupling⁶.

Because we want to be able to image atoms in both $F = 3$ and $F = 4$ states, we overlap the $F = 4 \rightarrow F' = 5$ imaging light with $F = 3 \rightarrow F' = 2$ light before splitting that light into different paths. Each path is fiber coupled and serves as a separate imaging path in either the MOT chamber or the glass cell. The optical power available for the $F = 4 \rightarrow F' = 5$ imaging light is limited to a few mW. To still have sufficient power on the atoms for each imaging path, we use $\lambda/2$ waveplates mounted in piezo-driven sliders⁷ to shift the light into the appropriate path for the imaging axis we want to use (Figure 3.5).

Tapered Amplifier

The master laser outputs about 50 mW, which is insufficient for all its applications. We use a tapered amplifier (TA⁸) to increase the available power and use the amplified light for the MOT and Zeeman slower cooling beams. The tapered amplifier is seeded with about 15 mW, that has been frequency

⁶The resonance frequency shift with magnetic field for the $F = 4 \rightarrow F' = 5$ transition is 1.4 MHz/G

⁷ELL-6k, Thorlabs

⁸BoosTA pro, Toptica

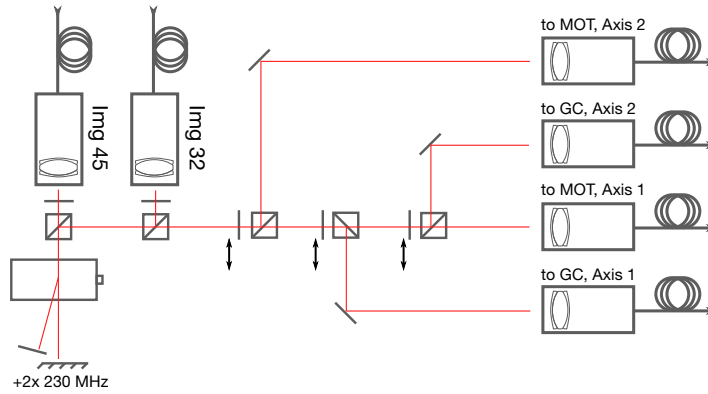


Figure 3.5 | Setup used to overlap $F = 4 \rightarrow F' = 5$ imaging light with $F = 3 \rightarrow F' = 2$ light and subsequently choose the imaging axis by moving waveplates in and out of the beam path (movement indicated by arrows).

shifted beforehand by passing through a DPAOM (the same one as the first DPAOM used for the imaging light). The output of the TA is fiber coupled and at a current of 3 A, about 1 W of power exits the fiber.

We originally used a self-built TA⁹. This TA was replaced because more power was needed behind the fiber coupler and because the TA output was very sensitive to the current and input coupling. At non-optimal current or coupling, the output power would fluctuate rapidly and randomly, reminiscent of mode hops.

MOT and Zeeman slower paths, $F = 4 \rightarrow F' = 5$

The MOT and Zeeman slower paths are replicas of each other. After splitting the light, each passes through a DPAOM which shifts the light back close to the $F = 4 \rightarrow F' = 5$ resonance and are subsequently fiber coupled to send the light to the experiment table. The Zeeman slower is detuned from resonance by -100 MHz, the detuning of the MOT light varies during the different cooling stages.

3.1.2 Repumper laser

As for the Master laser, the repumper laser light is provided from a Toptica DLPro¹⁰. Contrary to the Master setup, the beam output is circularized using an anamorphic prism pair and then fiber coupled before splitting it into different arms for the laser cooling stages. This leads to some power loss, as an additional fiber coupling is inserted between the laser output and the atoms, but eases the replacement of the laser diode compared to the master laser as only a single fiber coupling has to be recovered instead of three.

We have not had to replace the laser diodes of either laser so far. However, we started to observe horizontal drifts of the laser head output after about two years of continuous operation¹¹. These could be related to the aging of the laser diodes, or changes in the environment, e.g. the humidity. The fiber directly behind the repumper laser head made recovery from such drifts particularly easy.

After the fiber the light is split into five arms for locking, Zeeman and MOT repumpers, the polarizer for degenerate Raman sideband cooling and imaging on the $F = 3 \rightarrow F' = 2$ transition (see Figure 3.6 for a sketch).

⁹TA chip: TPA-0850-02000-4006-CMT04, EYP

¹⁰EYP-RWE-0860-06010-1500-SOT02-0000, EYP (Laser diode)

¹¹These drifts were also observed for the master laser

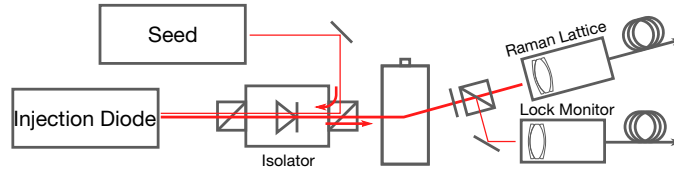


Figure 3.7 | Setup of the Raman lattice injection lock. The seed is sent into a second laser diode (injection diode) with higher power output. The injected light forces the second laser diode to lase at the same wavelength. An optical isolator allows injection of the second diode without feedback from the second diode into the seed. An AOM is used to intensity stabilize the power of the Raman lattice, and a separate monitoring fiber is used to confirm if the injection lock is working.

Polarizer and Imaging light, $F = 3 \rightarrow F' = 2$

The polarizer and imaging light share a double-pass AOM setup that brings the frequency close to the $F = 3 \rightarrow F' = 2$ resonance. The double pass AOM allows us to use different frequencies during imaging and dRSC, and in principle also allows imaging at high fields, where the Zeeman shift of the hyperfine states leads to a change in the resonance frequency. However, the $F = 3 \rightarrow F' = 2$ resonance is not closed, as atoms from $F = 2, m_F = 2$ can decay into $F = 3, m_F = 1, 2, 3$. Therefore imaging at high fields should preferably be performed on the $F = 4 \rightarrow F' = 5$ resonance, which does have a closed transition ($|F = 4, m_F = 4\rangle \rightarrow |F' = 5, m_F = 5\rangle$ and $|F = 4, m_F = -4\rangle \rightarrow |F' = 5, m_F = -5\rangle$).

3.1.3 Raman lattice laser

The Raman lattice laser is used to trap the atoms and induce spin flips via Raman transitions during the degenerate Raman sideband cooling phase of pre cooling. It is detuned by around -20 GHz from the $F = 3 \rightarrow F' = 4$ transition. This is sufficiently far detuned that small drifts of the laser frequency are not critical to the cooling performance and we can use an unlocked external cavity diode laser (ECDL)¹⁵ to injection lock a separate, high power laser diode¹⁶.

In an injection lock, the seed (in our case the ECDL) forces a second laser diode to lase at the same frequency as the seed [118–121]. This works within a small capture window of temperature and current of the second laser diode, where the injected diode would lase close to the seed frequency in any case. Once injected, the second laser diode outputs light of the same linewidth as the seed. This setup therefore allows easy amplification of narrow linewidth lasers.

To check whether the injected diode is locked, we pick off some of its light and measure its frequency with a wavemeter. We vary the current to the injected diode while monitoring the frequency. Once the diode is injected, the frequency on the wavemeter jumps to the frequency of the seed and remains there within a small range of currents, before falling out of lock and jumping back to the free-running frequency of the diode. The range of the currents for which the injected diode remains locked depends not only on the injected diode's current and temperature settings but also on the coupling and power of the seed.

Before coupling the output of the injected diode into a fiber to send to the MOT chamber, it is sent through an AOM, which is used to stabilize the intensity of the Raman lattice. A photodiode on the experiment table measures the power of the lattice light arriving at the MOT chamber. This power is stabilized using a PI loop box which feeds back to the RF amplitude of the AOM. This intensity stabilization also allows us to vary the power of the Raman lattice during a sequence by varying the setpoint of the PI loop. While this feature is not too important for dRSC, it is indispensable for the optical dipole traps used in later stages of the experiment. Note that because the light for the Raman lattice

¹⁵Housing: DLPro, Toptica; Laserdiode: EYP-RWE-0860-06010-1500-SOT02-0000, EYP

¹⁶Laser diode: 854 ± 7 nm, Part No. 22045504, Lumentum

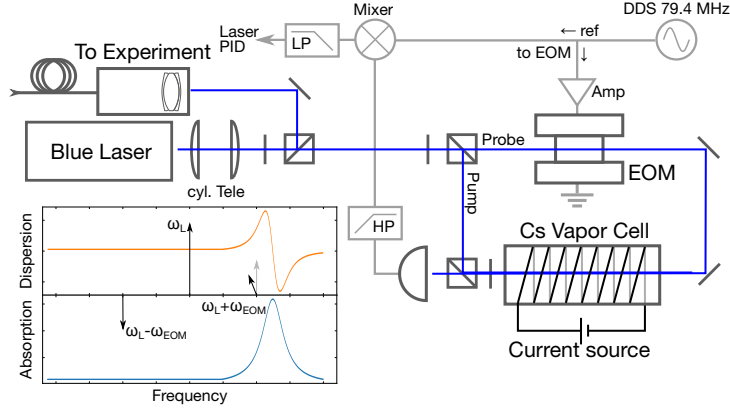


Figure 3.8 | Setup of the blue laser. The Cs vapor cell used for locking is heated with a current source to increase the signal. Inset illustrates frequency modulation spectroscopy. One sideband $\omega_0 + \omega_{\text{EOM}}$ experiences dispersion and absorption due to an atomic resonance (rotation and shortening of the arrow).

is split on the experiment table and fiber coupled again before it is sent through the MOT chamber, only one axis (the y axis) is properly intensity stabilized.

3.1.4 Blue laser

We want to reach single site resolution in optical lattices with relatively small spacings (e.g. $767/2\text{nm}$), which is difficult to reach with the usual imaging wavelength of 852 nm . For instance, with the NA of our objective of 0.8 , the Abbe radius of the point spread function for 852 nm , i.e. the resolution according to the Rayleigh criterion is around $d = 0.61\lambda/\text{NA} = 650\text{ nm}$. Post-processing and techniques from super resolution microscopy might still be able to provide single site resolution at 852 nm [122, 123]. However, another method would be to use a different imaging wavelength. The next obvious choice for Caesium is to use the $6S \rightarrow 7P$ transition instead of the usual $6S \rightarrow 6P$ one. The wavelength of the $6S_{1/2} \rightarrow 7P_{3/2}$ transition is 456 nm , which would reduce the Abbe radius by almost a factor of 2.

Using this transition for imaging brings its own problems [121]. Unlike the $6P$ transition, the $7P$ transition can not only decay back into the ground state manifold $6S$, but also into the $7S$ and $5D$ manifolds (cf. Figure 3.1). This creates two problems; one, not every emitted photon actually has a wavelength of 456 nm and two, the decay over these other states might bring about other sources of heating.

For example, the lifetime of the $5D$ state is on the order of a few μs [124, 125], about 100 times longer than the $6P$ states. The long lifetime can cause heating due to the motion of the atom in the lattice potential while in an excited state. The lattice potential will generally be different for an excited state atom than for the ground state. Assuming the atom is in both the internal and motional ground state, excitation will first project the motional state onto the (different) motional states of the internal excited state. The inverse happens during the decay back to the internal ground state. Provided the decay is fast, the projection back to the motional states of the internal ground state will lead to very small occupation in higher energy motional states and the associated heating will be negligible.

However, if the decay is long and the potentials experienced by internal ground and excited state atoms is very different, the projection of the motional state during decay to the ground state will lead to non-negligible occupation of the excited motional degrees of freedom and thus to heating. This and other possible heating processes have been analyzed theoretically in Refs. [121, 126].

Nevertheless, we decided to setup a laser system for imaging on the blue line (Figure 3.8). The light is provided by a Toptica DLPro. We lock the laser to the $5S_{1/2} \rightarrow 7P_{3/2}$ resonance using frequency modulation spectroscopy [127]. We chose to use frequency modulation spectroscopy as opposed to

modulation transfer spectroscopy because modulation transfer spectroscopy works best with a modulation frequency close to the linewidth of the transition [114]. In addition, the modulation transfer is strongest on closed transitions, which does not exist for the $5S_{1/2} \rightarrow 7P_{3/2}$ resonance. In frequency modulation spectroscopy the probe (as opposed to the pump) passes through an EOM. The sidebands modulated onto the probe are split by more than the transition linewidth. Only one of the sidebands will typically be overlapped with a resonance, leading to an imbalance in phase and amplitude of the sidebands (see inset of Figure 3.8). This can be detected by beating the sidebands with the carrier on a photodiode, and demodulating the signal in the same way as in the modulation transfer spectroscopy setup. The details of the locking of the blue laser are described in [121].

To prevent the atoms from decaying slowly via the 5D manifold, we have bought DFB lasers running at the 5D \rightarrow 7P lines, 1340 nm¹⁷ and 1360 nm¹⁸. These are intended for repumping atoms that decayed into the 5D manifold. Currently, a master student in our lab is setting up the repumping setup [128].

¹⁷NLK1B5E, NTT

¹⁸NLK1E5G, NTT

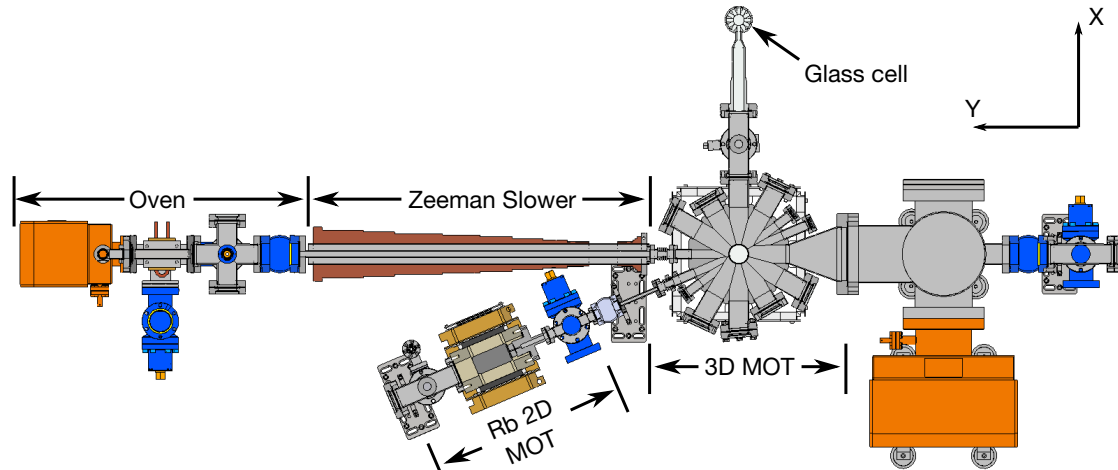


Figure 3.9 | Cut through the vacuum system after the oven upgrade (see subsection 3.2.2). The oven serves as the atomic source, the Zeeman slower slows the atomic beam from the oven into the 3D MOT chamber, where the atoms are pre-cooled and subsequently transported optically to the glass cell. The final evaporation and experiments happen in the glass cell. The Rb 2D MOT is intended for possible future dual species experiments and will not be described in detail in this thesis.

3.2 Vacuum system

This chapter describes the vacuum system. The system consists of an oven, a Zeeman slower, a MOT chamber and a glass cell. Initial capture and pre-cooling of the atoms happens in the MOT chamber. The atoms are then transported to the glass cell, where they are condensed and loaded into lattices for 2D physics experiments. Figure 3.9 shows a cut through the chamber from the oven through the Zeeman slower to the MOT chamber, and Figure 3.10 shows a more technical drawing of the vacuum system.

3.2.1 General considerations

The experiment has to occur at ultra high vacuum conditions (low 1×10^{-11} mbar), as collisions between trapped atoms and the background gas (in thermal equilibrium with the chamber) will lead to atomic loss and heating. This ultimately limits the lifetime of the trapped atoms. In principle, one way to reach low pressures is to actively cool the vacuum system itself, for example by running liquid nitrogen across the outside of the chamber. This makes the setup more complex, so we decided not to pursue this kind of vacuum system. To still reach low pressures, all vacuum components have to be cleaned prior to assembly (residual contaminants on the chamber surface will outgas, making the background pressure worse) and the chamber has to be baked to remove adsorbed water in the steel chamber (see subsection 3.2.5).

Finally, to reach low pressures in the MOT chamber and glass cell, high vapor pressure sections (e.g. oven) are separated from low pressure sections with differential pumping tubes (e.g. Ref. [129], Sec. 4.1). Differential pumping tubes are small diameter connections between different vacuum sections. The low transmission probability (conductivity) of atoms through these tubes leads to a low flux of atoms between the sections. A vacuum pump connected behind the tube can then lead to a lower pressure behind the tube than before it. For the low pressures we are working at, one can typically assume that the mean free path of the atoms is large compared to the diameter of the tubes connecting two sections of the vacuum system, so any atom is more likely to hit a wall than to hit another atom. In this case, the conductivity is given by $C = \frac{\pi d^3}{12l} \langle v \rangle (T)$. In case multiple differential pumping sections follow after one another, the total conductivity is given as $1/C = 1/C_1 + 1/C_2$. The pressure drop

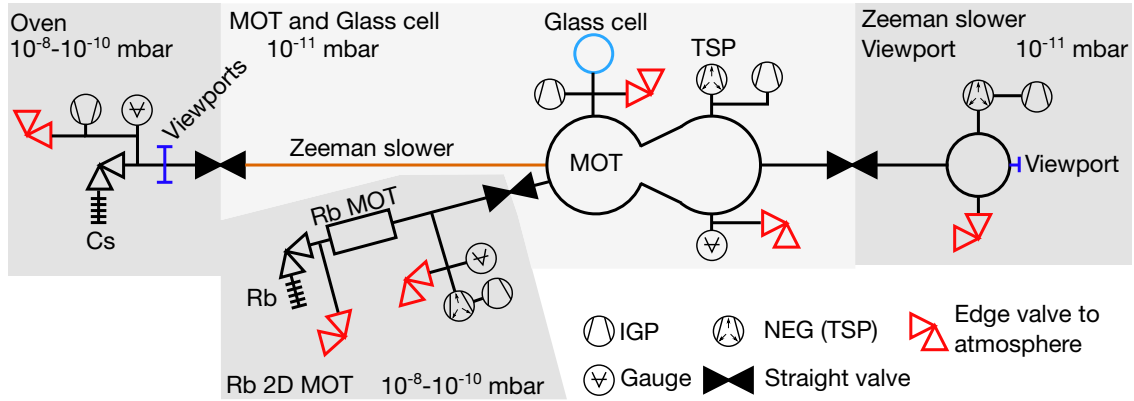


Figure 3.10 | Schematic of the full chamber, with pumps, connections to the outside for evacuating the system and straight valves indicated, after the oven upgrade (see subsection 3.2.2)

across the differential pumping sections is given by the ratio of the conductivity to the pumping speed C_{pump} of the vacuum pump behind the tube: $p_{\text{out}} = \frac{C}{C_{\text{pump}}} p_{\text{in}}$.

3.2.2 Oven

The oven serves as the source for Caesium atoms. In the oven Caesium atoms are heated to 60-100 °C, temperatures at which Caesium is gaseous. The hot atoms escape the oven through a collimator, generating an atomic beam with low transverse velocities. Initially we used a microchannel plate [130, 131], an array of steel tubes with small diameter¹⁹, in the hope to create a bright atomic beam to facilitate fast loading of the MOT (Figure 3.11a-b).

The microchannels were mounted inside a CF40 double blind flange with a hexagonal cut out. The hexagonal cut out enforces tight packing of the microchannels [132]. In our case the hexagon had a sidelength of 2.7 mm resulting in 217 microchannels ($N_{\text{tot}} = 3N_{\text{side}}(N_{\text{side}} - 1) + 1$, $N_{\text{side}} = 9$). The oven flux can be estimated from $\Phi_{\text{tot}} = N_{\text{ch}} \frac{\pi d^3}{12l} n(T) \langle v \rangle (T)$ [131, 133] assuming a large ratio of channel length l to channel diameter d . Here $n(T)$ is the vapor density at temperature T and $\langle v \rangle (T) = 2\sqrt{2k_B T / \pi m_{\text{Cs}}}$ the mean thermal velocity. For 80 °C the flux amounts to around 2×10^{12} atoms/s. The actual flux of the oven was reduced by a differential pumping piece ($d = 8$ mm, $l = 100$ mm) between the oven tank and the Zeeman slower (Figure 3.11a). The microchannel oven has a large flux at low divergence. The divergence is low because of the large ratio of channel length to diameter, and the flux can be increased by adding more channels. We wanted a large loading rate of the MOT, so the large expected flux is why we opted for the more difficult to machine microchannel plate over a more conventional oven design.

Unfortunately, we never observed a clear signal of a collimated atom beam exiting the microchannel plate. In addition, the section behind the microchannel plates quickly filled with Caesium. The Caesium deposited on the ion pump (IGP) and ion gauge and eventually lead to failure of both. This failure telegraphed itself by the steady increase of the pressure reading of both IGP and vacuum gauge. This increase was attributed to Caesium covering the electrodes of both devices and leading to increased currents between them. Also, we saw what looked like corrosion on the seals of the CF40 viewports. Because of these issues, we rebuilt the oven section in July 2020 (Figure 3.11c). At that time we also replaced the microchannel plate with a different design adapted from the Chin group [134] (Figure 3.11d). This new design consists of two plates with 2 mm holes separated by a distance of 144 mm. The plates are heated while the tube between them is cooled as much as possible. Any Caesium atoms hitting

¹⁹EN 1.4301, Rohrschnitte Ø 0,30 x 0,20 x 10 mm, Robert Helwig GmbH

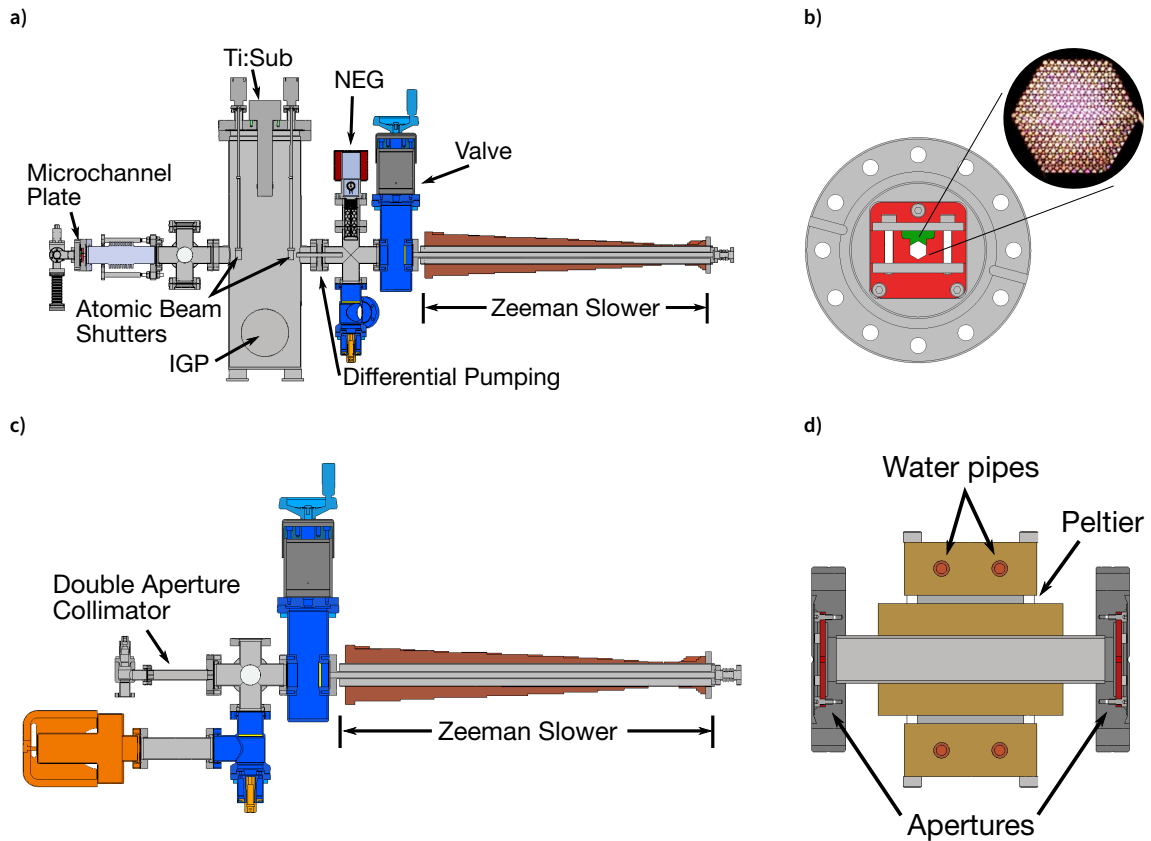


Figure 3.11 | **a** Sketch of the old oven section. Ti:Sub: Titanium Sublimation Pump, Gamma Vacuum, Partnr. 360819; NEG: Non-evaporable getter, SAES NexTorr D 200-5; IGP: Ion getter pump, Gamma Vacuum, 75S TiTan CV; Valve: VAT, All-Metal Gate Valve, Series 48.1; Atomic Beam Shutters: Magidrive, MD16N **b** Drawing and picture of the assembled micro channel plate, **c** Sketch of the new oven section with the **d** double aperture oven. The section between the two apertures (red) is cooled with peltier elements and water.

this middle tube section get adsorbed to the wall and do not leave the oven section, where it could potentially contaminate the ion pump and gauge.

The new oven section has a single IGP²⁰. From the temperature of the oven (80 °C) we expect a vapor pressure inside the oven of around 2×10^{-4} mbar. Assuming that the vacuum conductivity through the oven collimator can be approximated by a single tube of diameter 2 mm and length 144 mm ($C = \frac{\pi d^3}{12l} \langle v \rangle (T)$) and neglecting the conductivity to the IGP, the expected pressure in the section behind the oven is around $p = \frac{C}{C_{\text{pump}}} p_{\text{oven}} \approx 2 \times 10^{-8}$ mbar. This is close to the pressure read by the gauge at the time of writing but off by more than one order of magnitude from the pressure read by the IGP (5×10^{-10} mbar). In the new oven section, we have placed a glass ampule of 1 g Caesium²¹. The ampule was placed in a CF16 bellow and broken by bending the bellow. The breaking was tricky, because the ampule was only slightly longer than the non-flexible end piece of the bellow.

3.2.3 Zeeman slower

The atomic beam is slowed by a spin-flip Zeeman slower [135, 136]. A spin-flip Zeeman slower flips the direction of the magnetic field, hence the spin, over the slowing distance. It aims to combine

²⁰ 25 L/s, DI element, 25SDI2VSCNN, Gamma Vacuum

²¹ 1g 99.98% Caesium, Alfaesar, Articlennr. 10146

the benefits of a decreasing field slower and an increasing field slower. The decreasing field slower has the highest field at its entry and goes to zero at its end. The low field at the exit of the slower causes less interference with the magnetic fields in the MOT chamber. However, the atoms at the exit remain in resonance with the Zeeman slower light, which can interfere with the MOT operation. The inverted configuration, the increasing field Zeeman slower has the largest field at the exit, so the slowed atoms are not on resonance with the cooler light outside the solenoid anymore, however the magnetic field might interfere with the MOT.

In the case of a spin-flip Zeeman slower, the field minimum is somewhere in the middle of the solenoid, so the atoms exiting the solenoid are off-resonance, but the magnetic field is not as high as in the increasing field slower.

In our case, the solenoid is 66 cm long and is wound from rectangular ($4 \times 3 \text{ mm}^2$) copper wire with a hollow core (2 mm dia)²². The copper wire has a Kapton sheathing. The hollow core allows us to cool the solenoid by letting water run through. To find a good winding configuration, we first compute the ideal Zeeman slower field and then try to approximate it as well as possible with copper wire loops we can make from the rectangular wire.

The deceleration of the slower is limited by the saturation of the atomic transition, with a maximum acceleration given by $a_{\text{max}} = -\frac{\hbar k \Gamma}{2m \lambda}$. Typically, the Zeeman slower is designed assuming a slightly lower acceleration than this maximum to allow for imperfections. Here, $a = 0.64a_{\text{max}} \approx 37 \text{ km/s}^2$. In addition, we choose a length of the Zeeman slower of $l = 60 \text{ cm}$ and a MOT capture velocity of $v_{\text{MOT}} = 40 \text{ m/s}$. These were chosen based on reported values from other Caesium experiments [98, 137]. For a decreasing field Zeeman slower, these parameters set the capture velocity v_{ZS} of the slower and the detuning δ_0 of the laser via $v_{\text{ZS}} = \sqrt{2al + v_{\text{MOT}}^2}$ and $\delta_0 = \omega_0/(1 - v_{\text{MOT}}/c)$. v_{ZS} is fixed by the constant deceleration the atoms experience over a distance l and δ_0 by the Doppler shift at the exit of the Zeeman slower. Similarly, the magnetic field at the entry of the Zeeman slower is set via the resonance condition $\delta_0 + kv_{\text{ZS}} - \mu B_0/\hbar = 0$. Here $\mu = \mu_B(5g_{F=5} - 4g_{F=4})$ captures the differential Zeeman shift of the coupled states, $|6^2S_{1/2}, F = 4, m_F = 4\rangle$ and $|6^2P_{3/2}, F = 5, m_F = 5\rangle$. The magnetic field along the solenoid then varies as $B(z) = B_0\sqrt{1 - z/l}$. For a spin-flip Zeeman slower, this relation is modified according to $B(z) = B_0\sqrt{1 - z/l} - B_{\text{exit}}$, where B_{exit} determines the position along the solenoid where the magnetic field crosses zero. Here, we chose $B(\frac{5}{6}l) = 0 \text{ G}$. See Ref. [135] for a more in-depth discussion on optimal Zeeman slower design. The parameters for our Zeeman slower are $v_{\text{MOT}} = 40 \text{ m/s}$, $l = 60 \text{ cm}$, $v_{\text{ZS}} = 215 \text{ m/s}$, $B_0 = 150 \text{ G}$, $B_{\text{exit}} = 46 \text{ G}$.

Once $B(z)$ has been fixed, we iteratively add or subtract windings at possible positions along the Zeeman slower axis starting from an initial guess that simply uses the mean magnetic field value B_{mean} at each axial winding position. The magnetic field of a current loop of radius R is $B = \mu_0 I/2R$ with current I . The initial guess for the number of radial windings is then $B/B_{\text{mean}}/4$, with R chosen to be the minimal radius of a winding. The factor 1/4 is phenomenological, giving a better initial guess in our case.

As shown in Figure 3.12a, we find good agreement between the expected and measured magnetic fields from the Zeeman slower. The field was measured using a flux gate sensor²³ and at reduced current. The measured field was scaled to the same current that was used in the coil design to compare with the expected field.

The Zeeman slower is wound on a steel pipe that is slid over the Zeeman slower vacuum tube ($d = 10.3 \text{ mm}$, $l = 66 \text{ cm}$) before full assembly of the vacuum system. The tube is only rigidly connected to the oven section. A CF16 bellow (43 mm long) between the Zeeman slower and the MOT chamber allows stress relief in case the oven and MOT section expand differently during bake-out or are misaligned with respect to each other.

²²OF-OK®oxygen free copper, Hollow Conductor OD 4x3/ID Ø2 mm, Luvata tool # 8329, Luvata

²³Mag-03MC100, Bartington

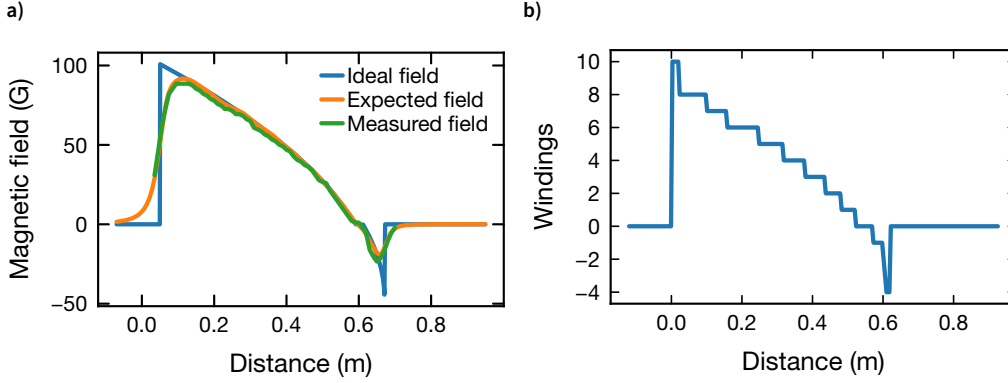


Figure 3.12 | **a** Comparison of ideal, theoretical and measured Zeeman slower. The blue curve follows $B(z) = B_0\sqrt{1 - z/l} - B_{\text{exit}}$. The orange curve was computed from the expected field profile using the optimized windings shown in **b** and using the formula for the on-axis magnetic field of a current loop [138] Eq. 30. **b** Number of windings of the Zeeman slower.

3.2.4 MOT chamber

In the MOT chamber the atoms from the Zeeman slower are captured and pre-cooled before being transported to the glass cell. The MOT chamber has 9 CF40 and 3 CF16 viewports to enable access for the many different beams we need for cooling and trapping of the atoms (cf. Figure 3.20). Most of the CF40 viewports are angled by 5° to avoid backreflections hitting the atoms. In addition to the Zeeman slower input (CF16) and output (CF64) ports, we also have an input port (CF16) for a Rb 2D MOT. The Rb 2D MOT has not been used to far, but was included in the design to enable future experiments with two different atomic species. Additionally, we have six viewports, two along z and four in the horizontal plane for the 3D MOT beams, four (2 CF40, 2 CF16) additional horizontal viewports for dipole traps and Raman sideband cooling and two ports for the transport axis (cf. Figure 3.20). We had ordered coated viewports from Lesker with a low magnetic permeability (316L, $\mu_r < 1.01$). The CF40 viewport were coated for 750-900 nm and 1064 nm the CF16 ones only for 750-900 nm. Upon arrival, we found a higher than expected relative magnetic permeability ($\mu_r \approx 1.4$) of the CF40 viewports. We were worried that they could create unwanted magnetic fields around the experiment chamber. Therefore, we replaced them with different viewports. Because these were the only components missing to assemble the vacuum chamber up to the MOT we chose to use stock viewports from different companies²⁴. Most of the viewports are uncoated, except the top and bottom viewports²⁵ and the CF16 viewports²⁶.

The exit of the Zeeman slower axis is connected to a large steel tank in which we have installed an ion pump and a Ti:Sub for pumping the MOT chamber. In addition a straight valve separates the Zeeman slower entry window from the MOT chamber. The Zeeman slower window may get contaminated with Caesium over time. Deposited Caesium can corrode the seal of the viewport (cf. subsection 3.2.2) and reduce the Zeeman slower power via absorption. Therefore, we added this separate section to allow exchanging the viewport without venting the full vacuum system. In the Zeeman slower window section, we have added a NEG+IGP pump²⁷. Around the MOT chamber we set up both horizontal and vertical breadboards for installation of the required optics.

To generate magnetic fields, we have two pairs of coils along the z -axis of the chamber, one connected in Helmholtz and one in anti-Helmholtz configuration (cf. ??). The coils are wound from hollow core

²⁴VPCF40DUVQ-L-BBAR650/950-NM and VPCF40UVQ-L-NM, Vacom; SFQ 40T/29, VAB; VPZL-SPL194, Lesker

²⁵VPCF40DUVQ-L-BBAR650/950-NM, Vacom

²⁶VPZL-SPL194; VPU3036064, Lesker, 750-900 nm

²⁷NexTorr D 200-5, SAES

Coil	Field	Windings	inner Radius	Distance between coils
MOT Offset	2.261 G/A	4 × 5	72 mm	55.2 mm
MOT Gradient	1.328 G/cm/A	8 × 5	40 mm	55.2 mm
MOT Compensation, z	1.5 G/A	20	77.5 mm	113 mm
MOT Compensation, x, y	0.5 G/A	20	45 × 100 mm	240 mm

Table 3.1 | Coils around the MOT chamber, see Ref. [139] for more precise information.

copper wire²⁸, with a $3 \times 4\text{mm}^2$ cross section and a 2 mm diameter hole. Water is run through the hollow core to cool the copper coils²⁹. The Helmholtz coils produce an offset field of 2.261 G/A at the atoms, the anti-Helmholtz coils produce a gradient of 1.328 G/cm/A at the atoms (Table 3.1, see Ref. [139] for details). We use MOSFETs to quickly switch off the coils.

For switching the coils on or changing the field we are limited by the current supplies³⁰. Originally we thought that switching times on the order of a few ms (e.g. 5 ms at 10 % load for SM 18-50) would be sufficient for the cooling stages in the MOT. As we were worried that at low loads the fast version of the power supplies would have increased noise, we chose to buy the regular PSU version. This turned out to limit the speed with which we could start degenerate Raman sideband cooling (dRSC) after the molasses phase as the offset coil needed around 10 ms to reach the desired field, i.e. longer than the actual dRSC duration. We therefore use a different power supply³¹ and the z-axis compensation coils for the offset field during dRSC.

Apart from the compensation coils along the z-axis, we also have compensation coils in the x and y direction, which we use to remove the background magnetic field at the position of the atoms (Table 3.1, see Ref. [139] for details). The coils are wound from 1 mm diameter copper wire and produce magnetic fields of 500 mG/A in the x and y axis and 1.5 G/A along the z-axis. The current in the x and y coils are not varied during the sequence. As mentioned already, we use the z-axis compensation coil to tune the offset field during dRSC, and also to produce a larger offset field during loading of the reservoir dipole trap (see subsection 4.2.2). The power supply connected to the z-axis coils allows switching of the current in a few μs as measured using a current clamp.

3.2.5 Bake-out

To reach the ultra high vacuum conditions required in our setup, we need to bake the assembled vacuum system. This bake-out serves to remove water adsorped to the steel components, that would otherwise gas out continuously and create a constant gas load that would limit the minimum pressures attainable. Typical temperatures for a bake-out are around 150°C . In principle, by baking at higher temperatures, other contaminants such as hydrogen can be desorped and pumped from the chamber. However, those higher temperatures would damage the viewports connected to the vacuum system, so this was not possible with the assembled system. Some of the custom components we ordered for the vacuum system have been baked at higher temperature by the manufacturer³².

Prior to assembly all vacuum components were cleaned in an ultrasonic bath, first filled with deionized water and in a second step in acetone to remove contaminants (e.g. oil, hydrocarbons) from the steel surfaces [140, 141]. They were subsequently wrapped in aluminium foil until everything was ready for assembly. Because the glass cell was not finished at the time we had all components for the chamber up to the MOT chamber we decided to assemble the MOT chamber first, and attach the glass cell separately once it arrives.

²⁸OF-OK®oxygen free copper, Hollow Conductor OD 4x3/ID Ø2 mm, Luvata tool # 8329, Luvata

²⁹Kühlmobil 101-WW-B400-SA-16D Gr. 00, Van der Heijden Labortechnik GmbH

³⁰Gradient: SM 15-100-P001, 100 A output, Offset: SM 18-50-P001, 50 A output, both Delta elektronika

³¹BCS 5/5, High Finesse

³²VAB, who produced our MOT chamber, Oven tank and MOT tank

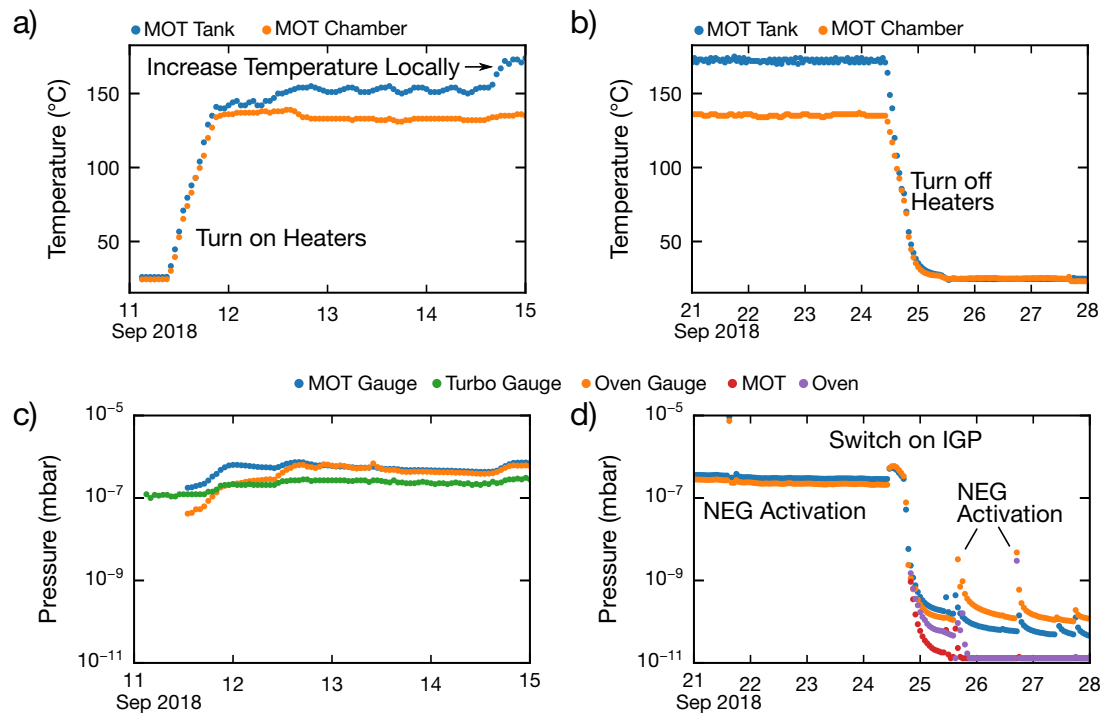


Figure 3.13 | a)-b) Exemplary temperatures at the beginning and the end of the bakeout of the MOT chamber. In total 16 temperature sensors were connected to the chamber during bakeout. c)-d) Pressure at the beginning and the end of the bakeout of the MOT chamber.

After assembly, a turbo pump was connected to the vacuum system and started. In preparation for the bake-out, temperature sensors³³ were connected to the vacuum system and it was wrapped in aluminium foil and heating tapes. While the sensors were stuck to the chamber directly using Kapton tape or copper wire, we added a layer of aluminium foil before adding the heating tapes³⁴. The full chamber was subsequently wrapped in more aluminium foil. Once wrapped, we started slowly ramping up the temperature taking care to avoid large temperature gradients across the chamber (Figure 3.13a,b). We kept a heating rate of $\approx 10^\circ\text{C}/\text{h}$, well below the maximum recommended heating rate for the viewports ($2\text{--}3^\circ\text{C}/\text{minute}$ according to Lesker, $25^\circ\text{C}/\text{minute}$ according to VACOM). Once the pressure had settled we activated the NEG and TSP pumps. After waiting once again for the pressure to settle, we turned on the IGP. As suggested by Edwards Vacuum [142], we closed the edge valves to the turbo pump once the voltage of the IGP settles and start cooling down the system slowly afterwards (Figure 3.13c,d). After the bake-out we reached pressures of 1×10^{-11} mbar once the system was fully cooled down.

3.2.6 Glass cell

The glass cell (Figure 3.14a,c) has twelve sides with two viewports above and below. One of the twelve sides is occupied by the glass to metal transition, the rest are covered by 11 mm diameter fused silica viewports. The fused silica viewports above and below the glass cell have a T-cross section with a larger diameter of 30 mm and a smaller one of 21 mm³⁵. All viewports are optically contacted to the glass cell body by Precision Glass Blowing. Additionally, all viewports have a nano-structured coating on

³³K-type thermocouple, readout with TC-08, Pico technology

³⁴VOLTRON-PLUS, Omnilab; KM-HT-BS30, SAF Wärmetechnik

³⁵Lasercomponents, Thickness tolerance ± 0.01 mm, < 5 arcsec parallelism, L/10 surface irregularity, 10-5 S/D

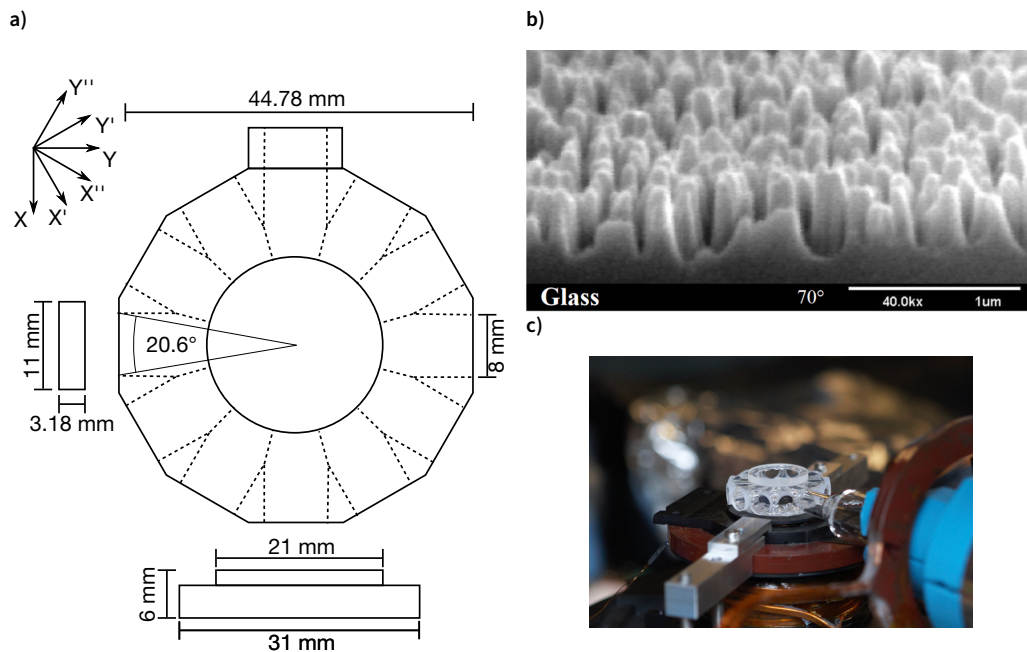


Figure 3.14 | **a** Drawing of the glass cell, **b** Structure of the nano textured window, **c** Photo of the glass cell. Figure **b** was taken from Ref. [147]

the in and outside made by TelAztec (Figure 3.14b). The nano-structured coating is etched into the fused silica. It works analogous to a moth eye. The spikes of subwavelength size and spacing effectively produce a gradient of the refractive index. This promises extremely low reflectivity [143–145], low dependence on the angle of incidence and very high resistance to temperatures. However, the coating may not be physically touched, so cleaning is only possible with solvents and without tissues. Note that the reflectivity increases as the wavelength increases as the ratio of spike depth to wavelength decreases so the index gradient effect is reduced [146]. This, combined with the increased reflectivity at large angle of incidence (AOI) leads to a reflectivity of about 3 % for 1064 nm at 60° AOI.

The glass cell was installed after the main vacuum system had already been installed and pumped to vacuum. We baked the glass cell separately from the main system and attached it to the main chamber afterwards. During the installation we filled both vacua with Argon. After removing the viewports sealing both chambers we ensured a constant flow of Argon out from the systems to avoid contamination of the chamber with water. We used Argon because we had a vacuum compatible pressure reducer for an Argon bottle but not for a Nitrogen bottle. After attaching the glass cell we tried to pump the system but found that we did not reach sufficiently low pressures. We concluded that the Argon flow during reattachment was insufficient, that the vacuum system had been contaminated and had to be rebaked.

After rebaking we reached acceptable pressures in the MOT and glass cell of close to 4×10^{-11} mbar and 2×10^{-11} mbar respectively. This is larger than we had after the initial bake-out of only the MOT chamber. However, we hoped that it is sufficiently low for our purposes and proceeded with setting up the experiment. Lifetime measurements in the glass cell upwards of 20 s³⁶ eventually confirmed that the pressure was acceptable.

After having used the glass cell for a while with temporary coils and breadboards, we installed the final coils and breadboards around the glass cell in April 2021. During the time we checked the glass cell viewports again, more carefully perhaps than during the initial installation. We observed milky

³⁶Thermal cloud in dipole trap. 60 s lifetime in magnetic trap of $|3, -3\rangle$ atoms in the MOT chamber. 11 s BEC lifetime.

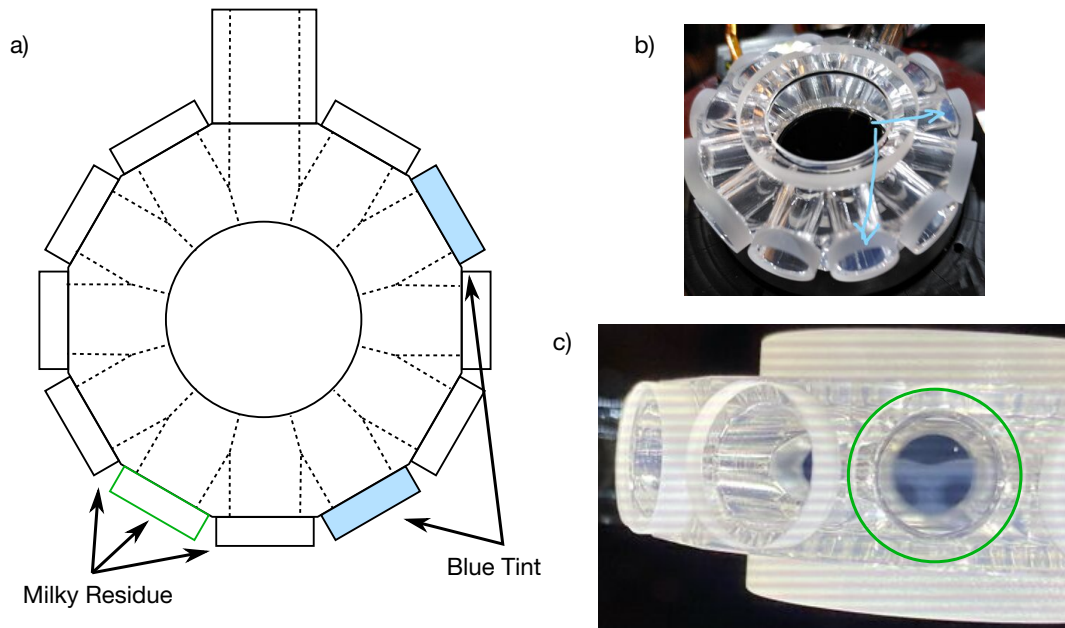


Figure 3.15 | a) Locations of viewports where contamination was observed. For some we observe milky residue similar to what is seen in c), for some we observe a bluish tint compared to other viewports as shown in b). In a) the green box marks the same viewport as the one marked in c)

spots on some of the viewports (Figure 3.15) and a bluish tint of two viewports. It is unclear if these discolorations have been present before the initial installation or if they are residue from working around the glass cell since installation. We did not attempt to clean the viewports since the most likely result would have been to make it worse as touching the viewports would break the coating and simply letting solvent drip over the surface would leave solvent residue. We have checked an identical replacement glass cell for similar blemishes and did not find any.

Around the glass we have two pairs of coils in the z -direction, to produce offset and gradient fields, another two pairs of coils in the Y' direction and one coil pair in the X' direction (see Table 3.2 and Ref. [139]). The z -axis gradient coil produces a field of 0.34 G/cm/A and is driven by the same power supply as the MOT gradient coils. Switching between them is achieved via MOSFETs. An additional set of MOSFETs in the gradient coil's path also allows us to switch the gradient direction. This allows us to levitate the atoms by compensating the force of gravity, or increasing the combined force due to gravity and the magnetic field by a factor of two depending on the direction of the gradient.

Coil	Field	Windings	inner Radius	Distance between coils
GC z Offset	2.06 G/A	2×5	48 mm	39 mm
GC z Gradient	0.34 G/cm/A	9	40 mm	44 mm
GC X'	0.966 G/A	2×5	55 mm	94 mm
GC Y' , outer	1.19 G/A	4×4	63 mm	136 mm
GC Y' , inner	uncalibrated	2×2	$40 \times 50 \text{ mm}$	94 mm

Table 3.2 | Coils around the glass cell chamber, see Ref. [139] for more precise information.

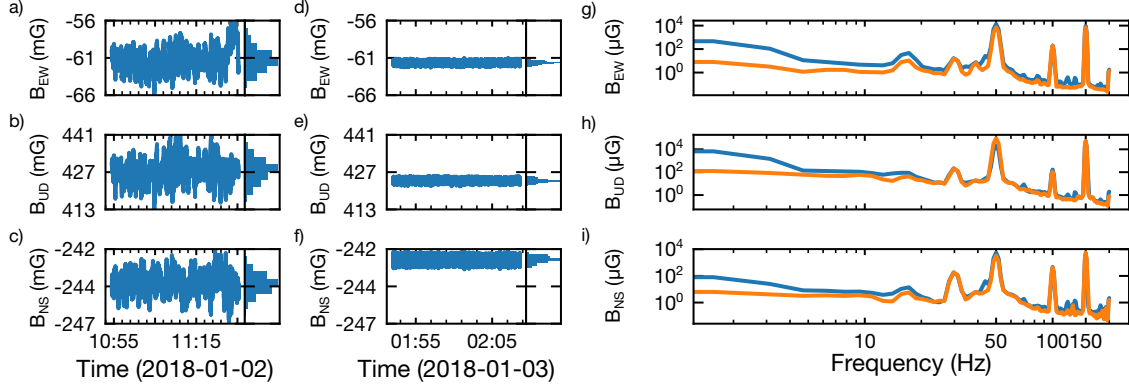


Figure 3.16 | Magnetic field stability measured in the lab during the day (a–c) and at night (d–f). The DC variation is significantly larger during the day due to the subway. The horizontal axis ticks in the figure are located at the scheduled arrival times of the subway. B_{EW} is the magnetic field in the east-west direction, B_{UD} the magnetic field in the up-down direction and B_{NS} the magnetic field in the north-south direction. The magnetic field was measured with a flux gate sensor from Sensys (FGM3D). (g–i) Fourier transform of the magnetic field measurement shown in (a–f). Blue is the daytime measurement, orange the nighttime measurements. The noise due to electronics is barely changed between day and nighttime, only the DC component is decreased significantly.

3.2.7 Magnetic field stability and stabilization

For experiments in the anti-magic wavelength lattice, hopping between the states is induced via a two photon Raman transition between the two hyperfine states $|F = 3, m_F = 3\rangle$ and $|F = 3, m_F = 2\rangle$. To understand how magnetic field fluctuations affect the Hamiltonian, it is helpful to consider the effective Hamiltonian coupling two states $a = |3, 3\rangle$ and $b = |3, 2\rangle$ via a Raman transition in a Λ -system [148]:

$$H_{\text{eff}} = -\hbar \begin{pmatrix} \frac{\delta}{2} + \frac{|\Omega_a|^2}{4\Delta} & \frac{\Omega_R^*}{2} \\ \frac{\Omega_R}{2} & -\frac{\delta}{2} + \frac{|\Omega_b|^2}{4\Delta} \end{pmatrix}. \quad (3.1)$$

Here, δ is the energy difference between a and b in the absence of coupling, $\Omega_R = \Omega_a \Omega_b^* / 2\Delta$ is the Raman coupling, $\Omega_{a(b)}$ is the Rabi coupling of $a(b)$ to the excited state and Δ is the detuning Raman beams to a third excited state. From this Hamiltonian, one can see that to first order magnetic field fluctuations enter the Hofstadter Hamiltonian as an energy offset between even and odd sites ($\hat{H} = \delta/2 \sum (-1)^i \hat{n}_i$), which can inhibit hopping between sites if the differential Zeeman shift $\delta = g_{F=3} \mu_B B$ becomes comparable to the tunnel coupling. For this reason, the magnetic field has to be actively stabilized during the experiment.

As a first step, we characterized the magnetic field fluctuations we observe in the lab. We find strong drifts of the magnetic field associated with the subway close to the lab (Figure 3.16a–c), and oscillations at 50 Hz and harmonics thereof due to the mains line and electronic equipment around the lab (Figure 3.16g–i).

The peak variation in the offset field of 28 mG during the day is in the up-down direction. During the night, i.e. without the subway running, the root mean square error (rmse) of the magnetic field amplitude is $500 \mu\text{G}$. This corresponds to an energy difference between $m_F = 2$ and $m_F = 3$ atoms of 175 Hz, comparable to typical hopping rates in lattice experiments.

To address the fluctuations of the environment magnetic field, we have installed a commercial magnetic field cancellation system³⁷ (A more detailed explanation of the stabilization setup and performance, with the experimental coils running, will be given in Ref. [139]). The cancellation system uses

³⁷MK5, IDE (Integrated Dynamics Engineering)

flux gate sensors to measure the magnetic field and feedbacks to a compensation coil cage mounted around the glass cell. The sensors need to be placed as close as possible to the glass cell so the field measured by the sensors and the field at the atoms is not too different. As the sensors saturate at 1 G, they have to be placed such that they do not measure the magnetic field due to the offset coils around the glass cell. The sensor is therefore split into three³⁸, one for each axis, and each sensor is placed at a zero crossing of the magnetic field coils.

The compensation cage for the stabilization has a side length of around 2 m, with the glass cell in the center. Each axis has 10 windings. Because of a large offset field along the z direction, we have an additional coil pair³⁹ along that axis, which is not driven by the cancellation system (see also Ref. [139]). The large side length ensures that the magnetic field due to the compensation coils is homogeneous around the glass cell. The power supply driving the compensation coils can compensate an offset field of a few 100 mG, with a bandwidth of around 500 Hz. The compensation uses three separate PID loops internally. One to compensate slow drifts up to a few 10 Hz, another faster one spanning up to 500 Hz and up to 7 small bandwidth loops that stabilize oscillations at a specific frequency such as 50 Hz. With all three loops enabled, we reach a rmse of the magnetic field amplitude of around 134 μG or 49 Hz energy difference between $m_F = 2$ and $m_F = 3$ atoms measured with the in-loop sensor.

³⁸Mag-03MC100, Bartington

³⁹11 windings, 1 mm² cross section, copper, driven by Rhode und Schwarz HMP4040

3.3 Metrology

3.3.1 Absorption imaging

Absorption imaging [149, 150] is used for most of the data taken throughout the course of this thesis. In absorption imaging, atoms are illuminated with resonant light and the transmitted light is imaged on a CCD. Some of the light will be absorbed by the atoms. Provided the intensity is much smaller than the saturation intensity, the reduction in transmitted light can be mapped to the column density $n(x, y)$ of the atoms along the imaging direction via Lambert-Beers law [149, 150]

$$I = I_0 e^{-\sigma n(x,y)}, \quad (3.2)$$

with the scattering cross section $\sigma = \frac{\sigma_0}{1+4(\Delta/\Gamma)^2+I/I_{\text{sat}}}$ and the resonant cross section $\sigma_0 = \hbar\omega_0\Gamma/2I_{\text{sat}}$; I_{sat} is the saturation intensity, Γ the linewidth, I the intensity and Δ the detuning from resonance. For Caesium, with isotropically polarized light resonant on the $F = 4 \rightarrow F' = 5$ transition the saturation intensity is given by $I_{\text{sat}} = 2.7 \text{ mW/cm}^2$ and the resonant cross section $\sigma_0 = 1.4 \times 10^{-9} \text{ cm}^2$ [111]. For σ^+ polarized light, resonant with the cycling transition $F = 4, m_F = 4 \rightarrow F' = 5, m_{F'} = 5$, $I_{\text{sat}} = 1.1 \text{ mW/cm}^2$ and $\sigma_0 = 3.5 \times 10^{-9} \text{ cm}^2$.

In the experiment, to improve the signal to noise ratio three images are taken, one with the atoms (absorption image I_A), one without atoms (bright image I_B) and one without atoms or light (dark image, I_D). The images are used to compute the optical density (OD)

$$\text{OD}_{ij} = \ln\left(\frac{I_B - I_D}{I_A - I_D}\right), \quad (3.3)$$

where the indices i, j run over the camera pixels. The atom number can be estimated from the OD by integration. This requires knowledge of the size of one camera pixel at the position of the atoms Δx_{px} . The total atom number is given as

$$N = \frac{\Delta x_{\text{px}}}{\sigma} \sum_{ij} \text{OD}_{ij} \quad (3.4)$$

This bare pixel sum is sensitive to noise and offsets of the computed OD. To avoid these errors, we typically fit a 1D normal distribution $\mathcal{N}(x, \sigma_x) + O$ to the OD summed along one of the pixel axes. Provided a proper normalization of the distribution ($\int \mathcal{N}(x, \sigma_x) dx = 1$), the total atom number is then simply the fitted amplitude A .

3.3.2 Time of Flight

In time of flight, the atoms are released from a trap and absorption images are taken at different times t_{tof} after the release. For a thermal cloud in free fall the expansion of the cloud follows [98]

$$\sigma(t_{\text{tof}}) = \sqrt{\sigma_0 + \frac{k_B T}{m} t_{\text{tof}}^2} \quad (3.5)$$

with initial size σ_0 . The free fall of the cloud may also be used to calibrate the magnification of the imaging system, as the cloud's center will follow

$$x(t_{\text{tof}}) = x - \frac{1}{2} g t_{\text{tof}}^2. \quad (3.6)$$

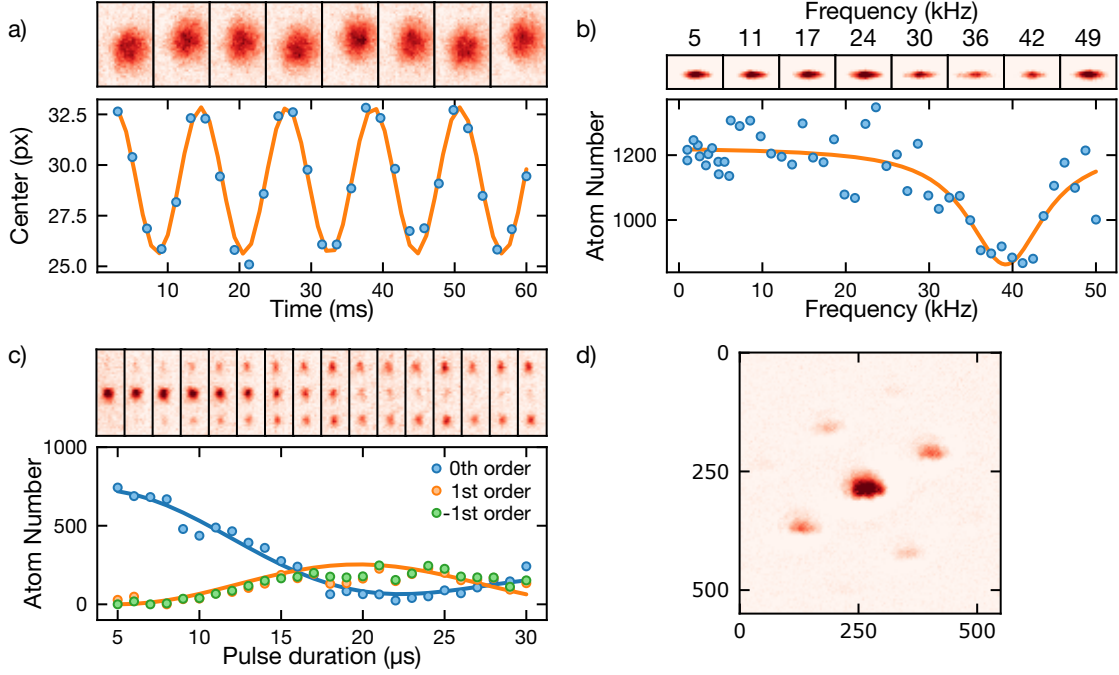


Figure 3.17 | **a)** Center of mass oscillation of the cloud in a dipole trap versus time. The fitted trap frequency is 80 Hz. **b)** Parametric heating at the frequency corresponding to the bandgap between the first and third band of an optical lattice leads to loss of atoms. Here the resonance is at 39 kHz, in a 767 nm lattice, corresponding to a lattice depth of $24 E_R$. **c)** Pulsing the lattice for a short duration leads to Kapitza-Dirac scattering. The population in the n -th band approximately follows a Bessel function of the n -th order [152]. From the fit, a lattice depth of $16 E_R$ is extracted. **d)** Interference pattern of a BEC loaded into a 2D 767 nm optical lattice. The lattice was loaded at low power (200 mW, $10 E_R$, $J = 50$ Hz) with an exponential ramp of 100 ms duration and 20 ms time constant. After holding the atoms for 100 ms the lattice power was increased to full power in 1 ms to compress the Wannier functions in each lattice site and increase the amplitude of the interference peaks.

In case of levitation using a magnetic field gradient, the harmonic anti-confinement due to the gradient leads to a modification of the horizontal expansion of the cloud according to (Ref. [151], Eqs. 3.12, 3.13)

$$\sigma(t_{\text{tof}}) = \sqrt{\sigma_0^2 \cosh^2(\omega_{\text{lev}} t_{\text{tof}}) + \frac{k_B T}{m} \frac{\sinh^2(\omega_{\text{lev}} t_{\text{tof}})}{\omega_{\text{lev}}^2}}. \quad (3.7)$$

with $\omega_{\text{lev}} = -\sqrt{m_F \mu_B g_F \partial B^2 / m B_0}$, where ∂B is the magnetic gradient along the expansion direction and B_0 the magnetic offset field. An anti-Helmholtz coil pair aligned along axis z produces a gradient of $\partial_z B / 2$ along x and y . For an offset field of 20 G and a gradient of 31.3 G/cm along z the anti-harmonic confinement along x and y is $\omega_{\text{lev}} \approx -2\pi \times 3$ Hz

3.3.3 Trap frequency measurement

We measure trap frequencies either using parametric heating or exciting a center of mass oscillation of the cloud [149]. We typically use center of mass oscillations for the dipole traps and parametric heating for the optical lattices. To excite the center of mass of the atoms, we briefly switch off and on one of the dipole traps. This typically causes the cloud to start sloshing in the dipole potential. For sufficiently weak excitation, the oscillation will be dominated by the dipole mode at the trap frequency ω_{trap} (Figure 3.17a).

We hold the atoms in the dipole trap for a variable amount of time t_{hold} and subsequently measure the position of the cloud after a fixed time of flight t_{tof} . The position versus t_{hold} oscillates with ω_{trap} .

Alternatively, in parametric heating experiments, we modulate the intensity of the optical potential at varying frequency ω_{mod} (Figure 3.17b). The amplitude modulation couples quantum states of the same parity, i.e. atoms in the ground state can only be excited to the second excited level, not the first [153]. At $\hbar\omega_{\text{mod}} = \hbar\Delta\omega_{13}$, the energy difference between ground state and second excited state, atoms are excited, the system heats up and, if the driving is sufficiently strong, atoms are lost from the trap. Note that in a lattice ω_{mod} is the difference between the first and third band, which depending on the lattice depth may be quite different from $2\Delta\omega_{12}$.

The lattice depth can be independently calibrated using Kapitza-Dirac scattering (Figure 3.17c). Here, the lattice is pulsed for a brief period of time τ . The atoms diffract off the standing wave and populate higher momentum states spaced by $2\hbar k$ with k the lattice wavevector. If the pulse duration is short compared to the harmonic oscillator frequency of a lattice site [152] (Raman-Nath regime), the population of the n -th momentum state follows $P_n = J_n^2(\frac{V_0\tau}{2\hbar})$ with J_n Bessel functions of the first kind. By varying τ , and measuring the change in the momentum state occupation, the lattice depth V_0 can be extracted.

To test the coherence of atoms loaded into a lattice, one can measure their momentum distribution. Abrupt release of the atoms from the lattice leads to interference between atoms released from different lattice sites [86, 154, 155]. This interference, analogously to double slit interference, reveals itself as sharp peaks at $2n\hbar k$, similar to Kapitza-Dirac scattering (Figure 3.17d). In the double slit analogy, the slits are lattice sites and the slit width are the size of the Wannier functions on each site. Therefore, the size of the Wannier function is related to the number of observable interference peaks, since its Fourier transform acts as an envelope on the interference pattern. Compressing the Wannier function increases its Fourier transform's width and thereby the amplitude of the interference peaks. To compress the Wannier function, the lattice depth is increased, which however also reduces the tunneling between sites and thereby the extent of coherence between lattice sites. Therefore, in the sequence, to observe the superfluid interference peaks, we load the atoms into the lattice at low power and just before detection rapidly increase the lattice depth. If the lattice depth ramp is fast compared to the tunneling time, the coherence should not be affected much and if it is slow compared to the lattice trap frequency, the local Wannier orbitals will follow the potential adiabatically and compress.

3.3.4 Microwave spectroscopy

Microwaves can be used to drive atoms between the different hyperfine states of the ground state manifold. Since both hyperfine states are stable, the resolution with which the resonance frequency can be determined is limited by the microwave pulse duration or the time between the two pulses in a Ramsey sequence (i.e. the linewidth is Fourier limited⁴⁰). The resonance frequency is dependent on the magnetic field due to the Zeeman effect. Therefore, microwaves can be used to calibrate the magnetic field at the position of the atoms. Starting with atoms in $|F = 3, m_F = 3\rangle$, we use microwaves to excite them into $|F = 4, m_F = 4\rangle$. We can detect the excited atoms by using absorption imaging on the $F = 4 \rightarrow F' = 5$ transition. The excitation frequency required can be computed from the Breit-Rabi formula [111]. At 100 G the energy shift computed with the Breit-Rabi formula (ΔE_{BR}) differs from the one computed within the anomalous Zeeman effect ($\Delta E = \mu_B g_F m_F B$ ⁴¹) by around $(\Delta E_{\text{BR}} - \Delta E)/h \approx -1$ MHz for the $|F = 3, m_F = 3\rangle$ state (Figure 3.18a). The exact frequency shift according to the Breit-Rabi formula at 100 G is -106.2 MHz.

To use microwaves to calibrate the magnetic field coils, we search for the resonance that excites the

⁴⁰assuming perfectly stable magnetic fields

⁴¹ $g_F \mu_B = \pm h \times 350$ kHz/G for $F = 3$ (-) and $F = 4$ (+)

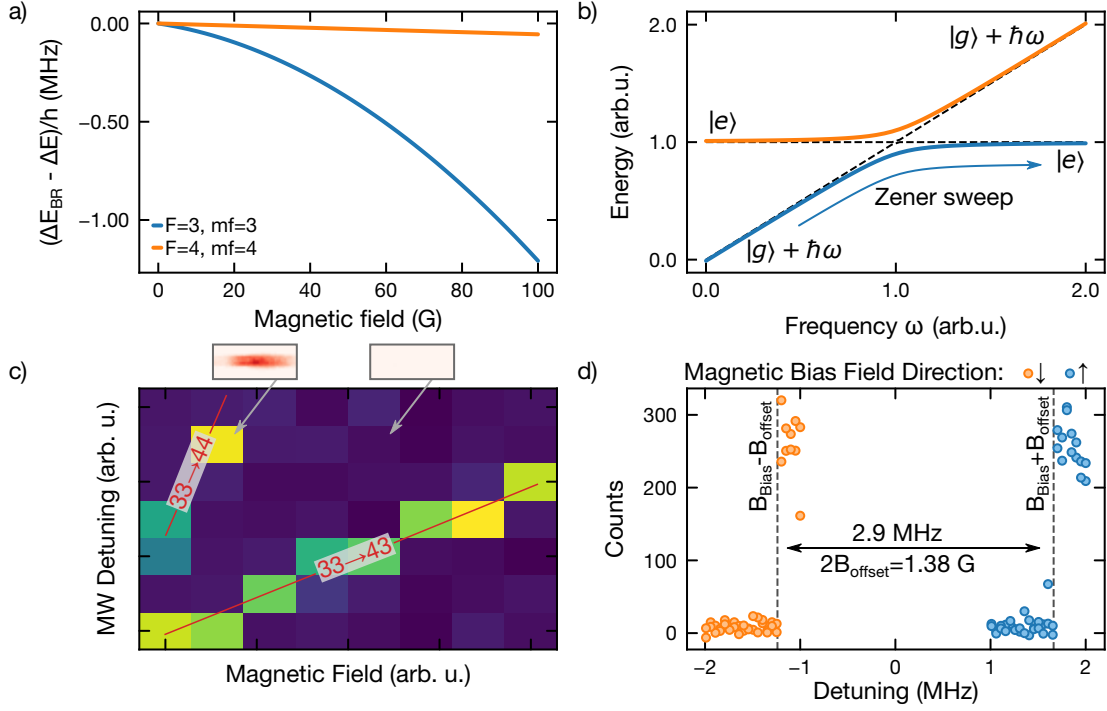


Figure 3.18 | **a)** Energy difference between the Breit-Rabi resonance frequency ΔE_{BR} and the anomalous Zeeman shift ΔE for $|F = 3, m_F = 3\rangle$ and $|F = 4, m_F = 4\rangle$. **b)** Sketch of the level scheme for Zener sweeps. In the dressed picture, increasing the microwave photon energy shifts the energy of ground state $|g\rangle$ plus photon field $\hbar\omega$ w.r.t. the energy of the excited state $|e\rangle$. The coupling between the states via the microwave field leads to an avoided crossing. Adiabatically sweeping the frequency across the resonance transfers atoms from $|g\rangle$ to $|e\rangle$. **c)** Transfer of population from $|3, 3\rangle$ to $|4, 3\rangle$ and $|4, 4\rangle$ versus center frequency of the microwave Zener sweep and magnetic field. The insets above the figure show absorption images of atoms in $F = 4$ for two sample pairs of center frequency and magnetic field, once with and once without any state transfer. As the magnetic field changes, the resonance frequency shifts according to the Breit-Rabi formula. The offset field can be extracted from the resonance frequency extrapolated to zero magnetic field. **d)** Offset calibration by inverting the magnetic bias field direction. The resonances are offset by $2B_{\text{offset}}$, projected along the bias field axis (provided that $B_{\text{bias}} \gg B_{\text{offset}}$). For the plotted measurement, the offset field points in the same direction as the bias field for the blue data points.

atoms from $|F = 3, m_F = 3\rangle$ to $|F = 4, m_F = 4\rangle$ and find the magnetic field that corresponds to this frequency difference between the levels. For excitation we use Zener sweeps, where the microwave frequency is swept over the resonance and population is adiabatically transferred from the ground into the excited state (Figure 3.18b). Repeatedly finding the resonance for different currents sent through the magnetic field coils allows reconstruction of the magnetic field generated per ampere of current and the magnetic background field along the bias field direction (Figure 3.18c). Note that the applied bias field should be much greater than the background offset field, since only in this case the measured offset field corresponds to its projection along the bias field axis. Alternatively, the offset field can be found by finding the microwave resonance frequency for opposite polarizations of the bias field. The frequency difference corresponds to twice the offset field, projected on the bias field axis (Figure 3.18d). The second method gives more accurate results from our experience, though the first was sufficient for the molasses phase in the MOT chamber (subsection 3.4.3). The accuracy of the magnetic background field measurement is limited by its random fluctuations. In our case, without the active magnetic field stabilization enabled, we find fluctuations of the background magnetic field on the order of 25 mG (cf. subsection 3.2.7 and Ref. [139]).

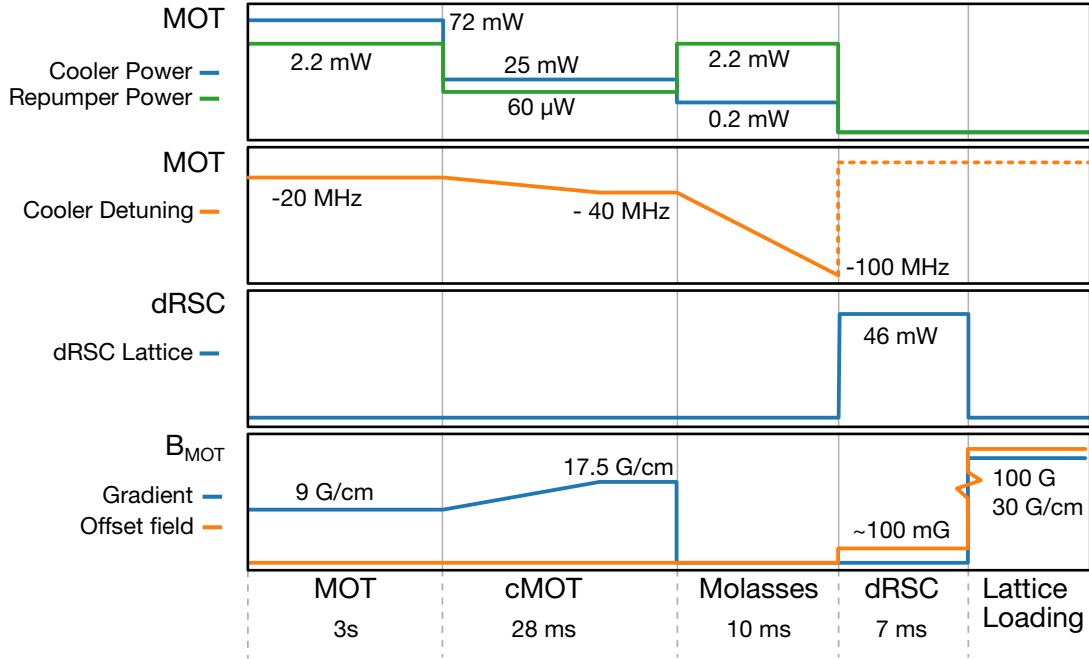


Figure 3.19 | Summary of the sequence up to and including dRSC. After completing dRSC, the atoms are ready to be loaded into the transport lattice

3.4 Pre-cooling

This section describes the pre-cooling sequence up to the transport. In brief, we collect atoms in a MOT, compress them, and after a short molasses phase capture them in an optical lattice for degenerate Raman sideband cooling. At the end of pre-cooling, 2×10^7 atoms at $<1 \mu\text{K}$ and a density of $3 \times 10^{10} \text{ cm}^{-3}$ are ready to be loaded into the transport lattice. [Figure 3.19](#) summarizes the pre-cooling steps, giving the step durations and parameter values. The full pre-cooling sequence takes 3.045 s, with most of the time spent loading the MOT. [Figure 3.20](#) and [Figure 3.21](#) show the optical setup around the MOT chamber and how the different cooling lasers are oriented with respect to each other.

	Atom number	Temperature (μK)	Density ($1/\text{cm}^3$)
cMOT	3×10^7	30-40	5×10^{10}
Molasses	3×10^7	10	3×10^{10}
dRSC	2×10^7	<1	3×10^{10}

Table 3.3 | Atom numbers, temperatures and densities during the pre-cooling stages

3.4.1 MOT and Zeeman slower

For slowing the atoms in the Zeeman slower we use around 5 mW of light detuned by -100 MHz from the $F = 4 \rightarrow F' = 5$ transition and 4.5 mW repumper light running on the $F = 3 \rightarrow F' = 4$ transition. The beam is expanded to 9 mm beam diameter and slightly converging towards the oven chamber. At 5 A current and -100 MHz detuning from the $F = 4 \rightarrow F' = 5$ transition atoms are slowed from around 200 m/s to around 40 m/s, sufficient to capture the atoms in the 3D MOT.

To align the cooling beam through the chamber we use a webcam with the IR filter removed, first aligning the beam through the MOT chamber and then aligning the beam on the oven output by

looking at the fluorescence signal from the atomic beam at the viewports close to the oven output. The final alignment optimization, as well as the power, detuning and current optimization is done with the MOT fluorescence signal.

For our MOT cooling we use 16 mm diameter beams. The horizontal beams are retro reflected, along the vertical direction we have two independent beams. This makes it easier to add additional beams along the vertical axis, required for e.g. Raman sideband cooling. We initially used dielectric mirrors which prevented us from observing a MOT signal, because dielectric mirrors can distort the circular polarization required for a MOT due to different reflectivities for s and p polarized light. Therefore we replaced any mirror behind the $\lambda/4$ waveplate with 2" gold mirrors, which don't distort the polarization. The beams have powers of 50 mW along X' , 7 mW along Y' and beams coming from the top and the bottom have 6 mW and 9 mW respectively. For initial alignment we center the incoming beam on the retro mirror and align the retro mirror such that the beam gets coupled back into the input fiber. If the polarization of the beams is correct, this alignment should be sufficient to capture some atoms in a MOT. We find that perfect retro reflection makes the MOT unstable. Hence, the retro beam is slightly misaligned from the incoming.

Once there is a signal, we optimize the Zeeman slower alignment, current, detuning, polarization and power to maximize the fluorescence. A photodiode records the fluorescence of the MOT versus time. By blocking one of the MOT beams, the MOT is destroyed and a new loading curve can be taken. After optimization, we tune the alignment, polarization of the MOT beams and the balance between them to again maximize the fluorescence signal. For MOT optimization a CCD is useful as it also allows us to optimize for the shape of the cloud. The beam balance and magnetic field compensation can be optimized by suddenly switching off the gradient and observing the subsequent expansion of the atomic cloud on the CCD. By switching off the gradient, one effectively creates a molasses. Therefore, ideally the atoms should spread slowly and symmetrically once the gradient has been turned off. Note that all these parameters also affect the position of the MOT. With the subsequent stages in mind, the MOT position should be close to the zero of the gradient field, which can be found by increasing the gradient and trying to minimize the change in position of the atomic cloud. Finally, we optimize the gradient field, detuning and total power of the beams using absorption imaging.

After optimization, we load around 3×10^7 atoms in 3 s with a gradient of 9 G/cm and a cooler detuning of -20 MHz.

3.4.2 cMOT

After the MOT loading we switch off the Zeeman slower light and compress the atomic cloud by ramping up the magnetic field gradient and cooler detuning. At the same time we reduce the repumper and cooler powers. In our compressed MOT we reach peak densities of a few 10^{10} cm^{-3} (Table 3.3) with negligible atom loss. The detuning and gradient are ramped to -40 MHz and 17.5 G/cm in 20 ms. The cooler and repumper power are reduced to 25 mW and $60 \mu\text{W}$. After the ramp we hold all parameters fixed for another 10 ms before continuing with the molasses phase.

While optimizing the cMOT, we found that detuning and gradient are coupled, similar to [156]. A higher detuning can compensate for a lower gradient and vice versa. We eventually settled on scanning both parameters simultaneously, sometimes even together with the repumper power as well. The signal was then optimized on the atomic density after short time of flight, not the atom number or temperature, because the cMOT phase is intended for compression only. Due to the high density, most light typically gets absorbed, making optimization impossible. To alleviate this, we detune the imaging beam from resonance. The resulting atom numbers are inaccurate, however it still allows relative comparison for optimization.

Beam	Power	Diameter	Intensity
MOT X	50 mW	16 mm	50 mW/cm ²
MOT Y	7 mW	16 mm	7 mW/cm ²
MOT Ztop	6 mW	16 mm	6 mW/cm ²
MOT Zbot	9 mW	16 mm	9 mW/cm ²
MOT Total	72 mW	16 mm	71.6 mW/cm ²
MOT Rep	2.2 mW	6 mm	15.6 mW/cm ²
cMOT Total	25 mW	16 mm	24.8 mW/cm ²
cMOT Rep	60 μ W	6 mm	0.4 mW/cm ²
Molasses Total	0.2 mW	6 mm	0.2 mW/cm ²
dRSC Y	31.2 mW	2.2 mm	1567.1 mW/cm ²
dRSC X	8.3 mW	2.2 mm	417.9 mW/cm ²
dRSC Z	6.9 mW	2.2 mm	348.2 mW/cm ²
dRSC Total	46.4 mW	2.2 mm	2333.2 mW/cm ²
dRSC Pol	650 μ W	2.2 mm	32.7 mW/cm ²
dRSC Rep	25 μ W	2.2 mm	1.3 mW/cm ²
ZS	5 mW	9 mm	15.7 mW/cm ²
ZS Rep	4.5 mW	9 mm	14.1 mW/cm ²

Table 3.4 | Powers, waists and intensities of the beams used for pre-cooling in our setup.

3.4.3 Molasses

After the compressed MOT we have a short molasses phase. For the molasses, we ramp the repumper back to full power, increase the detuning of the cooler to -100 MHz and switch off the gradient. The molasses cools the atoms to a few μ K (2μ K with good magnetic field compensation) in a few ms.

For the molasses to work well, the background magnetic field has to be compensated to high (better than ≈ 50 mG) precision. We measure the background magnetic field by driving Landau-Zener transitions between the $F = 3$ and $F = 4$ hyperfine groundstates using microwaves. The different sign of the Landé factor for $F = 3$ and $F = 4$ leads to a magnetic field dependence of the energy splitting of the two states. For all magnetic fields we are using in our lab the energy of a given hyperfine states scales approximately linearly with magnetic field ($E_{F,m_F} = \mu_B g_F m_F B$). However, for calibration we use the more exact Breit-Rabi formula (Eq. 26 in [111]) to compute the energy shift. If one irradiates the atoms with microwave radiation tuned to resonance, atoms are transferred from one hyperfine state to the other. In the case of a Zener sweep, the microwave frequency is swept over the resonance, which, if slow enough, transfers the population from one hyperfine state into the other.

To measure the background magnetic offset field, we send different currents through the magnetic field coils and find the resonance. The offset can be extracted from the offset of a linear fit to the resonance frequency versus current. With this method, we were able to compensate the field in the MOT chamber sufficiently to reach 2μ K temperatures after the molasses phase. Without magnetic field compensation, the molasses phase typically reached only 10 - 20μ K. In principle it is possible to reach even lower temperatures with molasses (Ref. [157] reports 0.7μ K), but because we follow the molasses stage up with degenerate Raman sideband cooling the temperatures we reach after molasses are not too critical (some Caesium experiments skip the molasses stage entirely [158]).

3.4.4 Degenerate Raman sideband cooling

After molasses we perform an additional cooling stage, degenerate Raman sideband cooling (dRSC), as is typical for Caesium BEC experiments [98, 137, 159]. During degenerate Raman sideband cooling the atoms are loaded into a 3D optical lattice (Figure 3.22). By appropriate choice of the lattice beam's polarizations, the lattice itself can induce Raman transition between different, degenerate m_F states. By

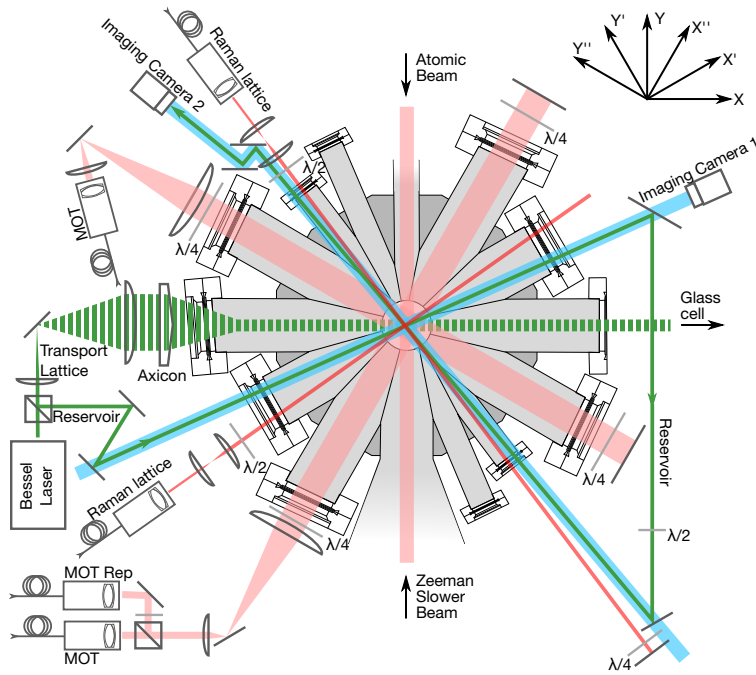


Figure 3.20 | Sketch of the laser beam setup around the MOT chamber. The view shows a crosscut through the chamber from the top. The axes orientations are indicated in the top right. The glass cell is located towards the right, the oven towards the top. We have retro reflected MOT (light red) beams along Y'' and X'' , both of which are expanded with a telescope to 16 mm beam diameter. The MOT repumper, running on the $F = 3 \rightarrow F' = 4$ transition, is overlapped with the MOT beam along the X'' direction. Two of the Raman lattice arms (darker red) are oriented along the Y' and X' axes. Only the beam along the Y' axes is retro reflected. The reservoir dipole trap (solid green) used for loading the atoms after degenerate Raman sideband cooling is oriented along the same axes as the Raman lattice arms. It is split from the Bessel beam laser output via a motorized waveplate. The Bessel beam for the transport lattice (dashed green) is expanded to 5 mm before passing through the axicon. Imaging axes are indicated with light blue colors, and are oriented along the X' and Y' direction. In both cases, the beams are overlapped with the reservoir dipole traps. The reservoir dipole trap light is filtered from the imaging light using dichroic mirrors and line filters.

applying a small magnetic field, it is possible to tune the resonance such that different vibrational states are degenerate. Here, the states that are brought into degeneracy are $|m_F, \nu\rangle, |m_F - 1, \nu - 1\rangle$. By adding a σ^+ polarized repumper, the atoms in $m_F < 2$ are pumped to the excited state ($6P_{3/2}, F = 2$). During the decay from the excited state the vibrational quantum number remains unchanged, leading to cooling in the case that the decayed state magnetic quantum number m_F is larger than the initial one. This cycle of Raman transition and repumping eventually stops when all atoms end up in $|m_F = 3, \nu = 1\rangle, |m_F = 2, \nu = 0\rangle$ or $|m_F = 3, \nu = 0\rangle$. To repump the last atoms remaining in $|m_F = 3, \nu = 1\rangle$ and $|m_F = 2, \nu = 0\rangle$ one adjusts the polarization of the repumper to also include some π component. This ideally results in all atoms in the $|F = 3, m_F = 3, \nu = 0\rangle$ state, i.e. a fully polarized sample in the ground state of the lattice well. For this reason the repumper is sometimes also called polarizer.

The Raman lattice is generated from three linearly polarized beams, one of which (Y' in our case) is retro reflected after passing through a $\lambda/4$ waveplate. The X' (Z) lattice beam's polarization is chosen such that they are aligned with the propagation direction of the Z (X') beam to prevent interference between the two. The Y' beam and its retro reflection interfere with each other and the X' and Z beams (cf. inset of Figure 3.22). The polarization of the Y' beam and its retro reflection typically subtend an angle of a few tens of degrees, however we have found that the cooling efficiency is not very sensitive to

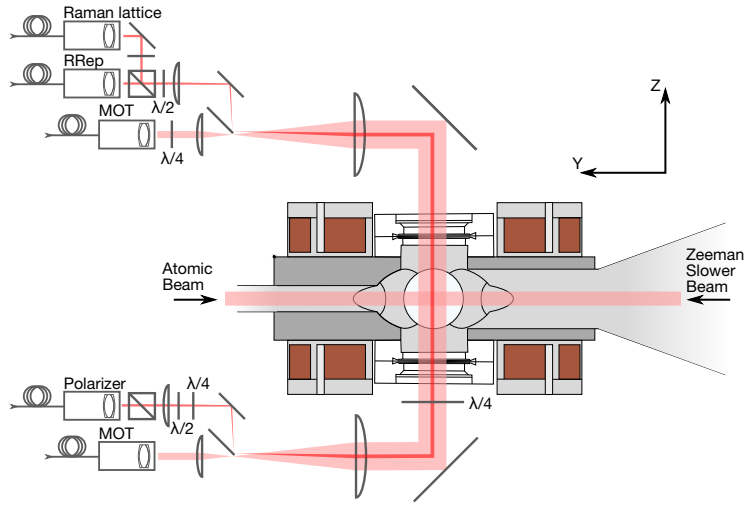


Figure 3.21 | Sketch of the laser beam setup around the MOT chamber, viewed from the side. The axes orientations are indicated in the top right. The oven is located towards the left. The orange squares above and below the chamber indicate the offset and gradient coils. There are two counter propagating MOT cooler beams (light red). The lower one passes through its waveplate after being expanded, the upper one is expanded after setting the polarization. Both are expanded to 16 mm. For degenerate Raman sideband cooling (darker red), one lattice arm and the Raman repumper (RRep) are first overlapped with each other and subsequently expanded to 2.2 mm beam diameter. The foci of the Raman and top MOT telescopes are overlapped to align the Raman beams along the MOT axes. The Raman polarizer is sent through the chamber from below. To align the polarization, we use a $\lambda/2$ and $\lambda/4$ waveplate. The $\lambda/4$ waveplate is mounted in a micrometer actuated rotation stage. The two waveplates allow us to precisely set the polarization to be only σ^+ or π at the position of the atoms. The polarizer is overlapped with the bottom MOT beam with a D-shaped mirror placed in the focus of the expansion telescopes, same as for the Raman lattice and repumper beams from the top.

this degree of freedom. Each beam has a waist of 1.1 mm and we have powers of 8.3 mW, 31.2 mW and 6.9 mW in the X' , Y' and Z axis respectively.

The four beams generate a 3D lattice, albeit one with asymmetric trap frequencies along different directions. The benefit of using 4 beams instead of 6 is a reduced sensitivity to phase fluctuations, which in this case only cause an overall translation [160]. Due to the strong Raman coupling during cooling, the difference in lattice trap frequencies is not resolved [161].

To align the lattice beams on the atoms we tune them on resonance and pulse them at the atomic cloud after the molasses [121]. This allows rough alignment by trying to minimize the pulse duration required to completely kill the atomic cloud. Finer alignment is possible by increasing the detuning from resonance. In this case the atoms in the center of the Raman lattice beam are killed first, leading to a hole in the atomic cloud. By symmetrizing this hole (or its projection along the imaging axis) we optimize the fine alignment for the X' and Z axis and the incoming Y' beam. The Y' -retro beam is simply coupled back into the Y' -axis fiber.

The Raman lattice is approximately -20 GHz detuned from $F = 3 - F' = 2$ resonance. This is in contrast to some other Caesium experiments [98, 137], where the lattice is detuned by -10 GHz and serves as depumper for atoms in $F = 4$. We need a separate depumper, which in our case is running on the $F = 4 - F' = 4$ transition. While the cooling does not work as well without the repumper, we have found that even μW 's of power are already sufficient.

In addition to the lattice and depumper beam we have a polarizer/repumper beam running on the $F = 3 - F' = 2$ transition. The polarizer beam has a beam waist of 1.1 mm and a power of $650 \mu\text{W}$. It is mostly σ^+ polarized, and repumps the atoms that underwent Raman transitions from $m_F < 2$. To

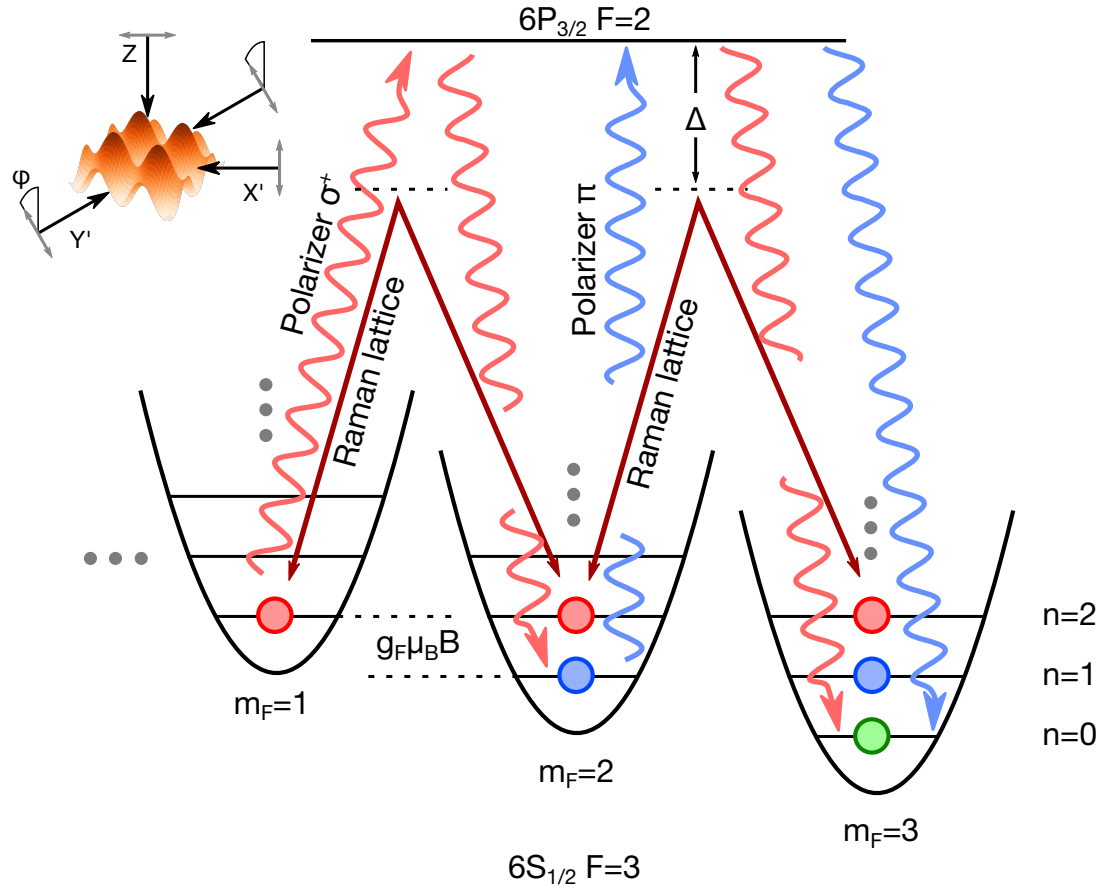


Figure 3.22 | Sketch of dRSC. Balls represent atoms in different internal (m_F) and vibrational (n) states. Different vibrational levels of different m_F states are brought into degeneracy by a magnetic field that shifts the states by $m_F g_F \mu_B B$. The Raman lattice (detuning Δ) couples the energetically degenerate states (atoms of the same color) via two photon Raman transitions. The σ^+ polarized component (red squiggly line) of the polarizer pumps the atoms into $6P_{3/2}, F = 2$, from where they decay. During the decay, the vibrational quantum number remains the same. If the m_F quantum number increases during the decay, the atom's energy is reduced by $m_F g_F \mu_B B = h\nu$, with ν the vibrational frequency of the lattice. The π polarized components (blue squiggly line) of the polarizer is required to pump atoms in $m_F = 2, n = 0$ and reach the absolute ground state (green ball). The inset in the top left shows the beam configuration of the Raman lattice. The polarization (grey) of all beams is linear. The polarizations of the beam along X' and Z are both in the X' - Z plane, preventing any interference between the two beams. The polarization of the Y' beams is angled such that it interferes with all other Raman lattice beams.

reach low temperatures it is critical that the polarizer does not have any σ^- component. To achieve this we have used a sequence suggested by Elmar Haller [162]. After the MOT (or cMOT or molasses) phase, we pump all atoms into $F=3$ using the depumper beam and add an offset magnetic field along the propagation direction of the polarizer. We subsequently turn on the polarizer beam at maximum power for a few ms. In case the polarizer has both σ^+ and σ^- components, the atoms will never be dark to the polarizer and the cloud will be blown away. However, for a purely σ^+ (or σ^-) polarized beam, the atoms will be pumped into the dark state $|F = 3, m_F = 3\rangle$ ($|F_3, m_F = -3\rangle$). So the polarization may be optimized by minimizing the effect of the polarizer beam on the atomic cloud. This method is extremely sensitive and allowed us to reduce the temperature from around $3 \mu\text{K}$ to around 400 nK . To measure these low temperatures, we use levitation and up to 150 ms time of flight, taking the correction due to the anticonfinement of the magnetic field gradient (Equation 3.3.2) into account.

After optimization, we slightly rotate the magnetic field axis by adding an offset field in the horizontal axis, which adds a small π polarization component to the repumper.

During optimization of the laser powers and detunings we have found that the final temperature after dRSC is most sensitive to the polarizer power and the offset field. We typically don't have to scan neither polarizer detuning nor depumper power. During optimization we minimize the cloud size after around 30 ms ToF as a proxy for the atomic temperature.

Once optimized, we have around 2×10^7 atoms at $<1 \mu\text{K}$ after 6 ms of cooling, at a density of around $3 \times 10^{10} \text{ cm}^{-3}$.

CHAPTER 4

Optical transport

Optical transport is a common technique for increasing the optical access for quantum gas experiments. This is especially interesting for quantum gas microscope experiments, as the objective severely restricts the optical access. Over the years, several different methods have been used to transport atoms from one place in the vacuum system to another (e.g. Refs. [129, 163–171]). These include moving the minimum of a magnetic trap [163], the focus of an optical trap [164, 168, 169, 171] or creating a running wave lattice [165, 167, 170].

We use a running wave lattice, formed from two slightly detuned lasers, to transport the atoms from the MOT into the glass cell. This allows faster transport compared to moving a magnetic or optical trap, and has no moving components, thereby avoiding vibrations as a possible heating or loss channel.

Because of the large distance between the MOT chamber and glass cell in our experiment, we use a Bessel beam, which does not expand during propagation. This beam provided the dipole trap to hold the atoms against gravity. To create the running wave lattice, we add a counter propagating Gaussian beam. We can control the detuning between Bessel and Gaussian beam using DDS boards.

This section describes the details of our optical transport and presents measurements on the transport efficiency and stability. The contents of this section have also been presented in Ref. [172].

4.1 Transport schemes

Cold, trapped atoms can be transported by moving the trap. Magnetically trapped atoms can be transported by either moving the coils generating the magnetic field gradient directly [129, 166], or by using a stack of displaced coil pairs and varying the current in each pair so as to move the minimum of the trap [163]. Caesium in its absolute ground state can not be magnetically trapped, so these schemes cannot be used in this experiment.

In our case, only optical transport is possible. The simplest schemes translate the lens focusing a dipole trap using a motorized translation stage [164] (Figure 4.1a). The atoms trapped in the dipole trap move with the focus of the trap provided that the axial trap frequency is sufficiently large compared to the acceleration of the stage. The axial trap frequency for Gaussian dipole traps is typically quite a lot weaker than the radial one ($\omega_{ax}/\omega_r = \sqrt{\lambda^2/2w_0^2} \approx 3.5 \times 10^{-2}$ for $w_0 = 20\lambda$). The critical acceleration, where the trap is not sufficiently steep to keep the atoms in the potential and they all spill out is accordingly lower, with the ratio $a_{ax}^{crit}/a_r^{crit} = 0.54w_0/z_R$. For a given trap depth V_0 , the critical accelerations are $a_{ax}^{crit} = 3\sqrt{3}V_0/8mz_R$ and $a_r^{crit} = \sqrt{4e^{-1/2}V_0}/mw_0$ where w_0 is the beam waist and z_R the Rayleigh range. As an example, Caesium in a 1064 nm dipole trap made by a 10 W round Gaussian with waist $w_0 = 20\ \mu\text{m}$ gives $a_{ax}^{crit} \approx 130\ \text{m/s}^2$ or about half the gravitational acceleration on the sun. To improve the axial trap frequency, experiments have used a crossed dipole trap [169].

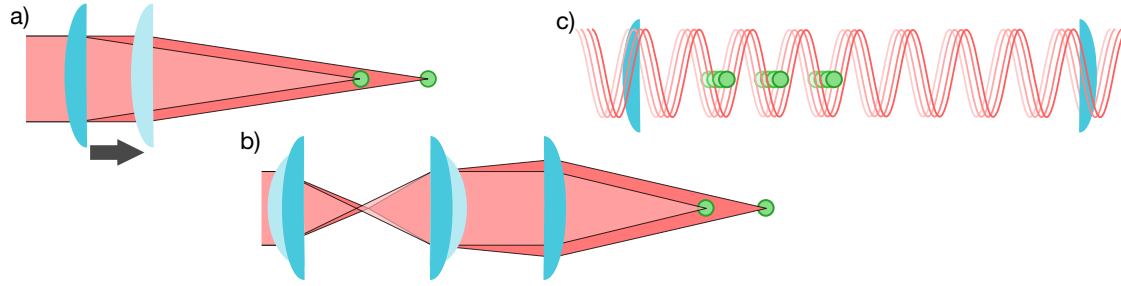


Figure 4.1 | Optical transport via a) lens translation, b) using focus tunable lenses or c) a running wave lattice

The small projection of the radial trap frequency along the direction of transport provides a slightly steeper trap and thereby allows for higher accelerations.

Apart from the limits placed on the transport due to the low trap frequency, vibrations of the translation stage lead to pointing fluctuations of the dipole trap beams which can heat the atoms in the dipole trap. To alleviate this, air bearing stages may be employed [169], or the translation of the lens is avoided altogether. The second option can be realized by using focus tunable lenses [168, 171] (Figure 4.1b). While using focus tunable lenses certainly avoids a linear translation stage and the associated pointing fluctuations during movement, the axial trap frequency is still the same as in regular dipole traps.

To address the issue of the low axial trap frequency we use an optical lattice [165, 167, 170] (Figure 4.1c). In an optical lattice, the axial trap frequency scales with $1/\lambda$, i.e. will typically be much larger than the radial trap frequency ($a_{\text{latt}}^{\text{crit}} = 4\pi V_0/m\lambda$). To transport atoms loaded into the lattice, a small frequency detuning Δf is introduced between the counter propagating beams. The resulting potential is proportional to $\cos(2kz - \Delta\omega t)$, where $k_1 + k_2 = 2k_1 + \mathcal{O}(\Delta f/f) \approx 2k$ is the lattice wavevector and $\Delta\omega = 2\pi\Delta f = \omega_1 - \omega_2$ is the frequency difference between the beams. This potential moves with a velocity of $v = \Delta\omega/2k = \lambda\Delta f/2$ in the direction of propagation of the beam with the higher frequency. In addition to allowing much larger accelerations, this transport scheme has no moving mechanical components. Apart from controlled transport of atoms from one place to the next, running wave lattices are also used for launching atoms in atomic fountain clocks [157, 173].

4.2 Transport setup

4.2.1 1064 nm Lasers

For all dipole traps, and for the transport lattice we use three 1064 nm fiber amplifiers¹. One 45 W laser² produces the reservoir dipole trap in the MOT chamber and the Bessel beam for the transport lattice, another 50 W laser³ is used for the X & Y dipole traps in the glass cell and the Gaussian beam of the transport lattice. A third 35 W laser⁴ is currently only used for the shallow angle vertical lattice in the glass cell (see section 5.3). The 50 W Gaussian laser and 35 W vertical lattice laser are both seeded by a 200 mW Mephisto⁵ (Figure 4.2). The Bessel laser is seeded using light from the Gaussian. This seeding setup will be described in detail later (subsection 4.2.3). To avoid interference between the different dipole traps and lattices entering the glass cell we use AOMs that shift the frequencies by ± 80 or 100 MHz (cf. inset of Figure 4.2). The seed for the 35 W vertical lattice laser is also shifted by 80

¹Azur Light System (ALS)

²ALS-IR-1064-50-A-SF, power stabilized, ALS

³ALS-IR-1064-50-A-SF, current stabilized, ALS

⁴ALS-IR-1064-30-A-SF, current stabilized, ALS

⁵Mephisto S 200 NEFC, Coherent

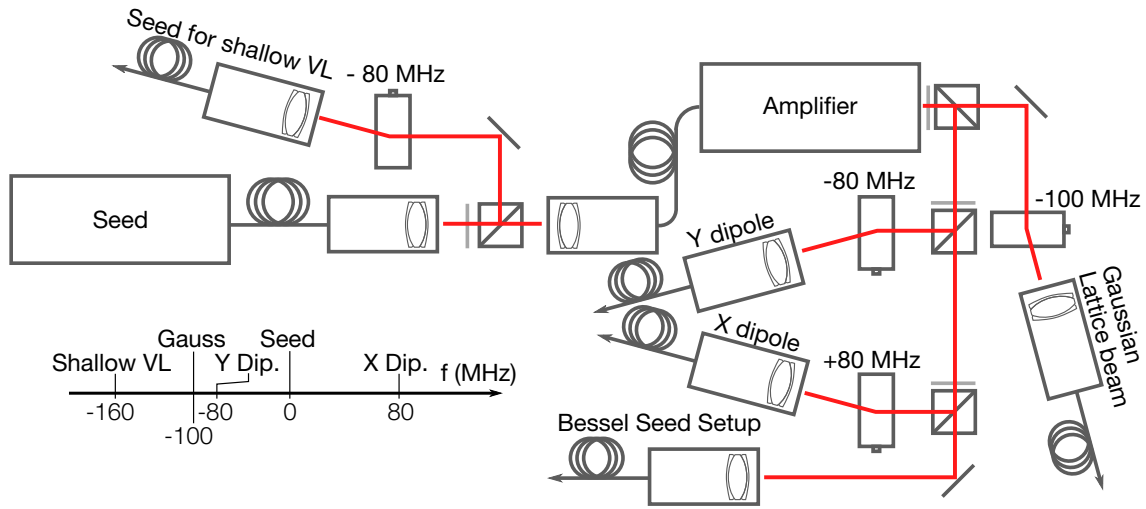


Figure 4.2 | Sketch of the seeding setup and the Gaussian laser setup before the fiber coupling to the experiment. The seed is used to seed two amplifiers, the Gaussian laser and the shallow angle vertical lattice (shallow VL, see section 5.3). To avoid interference between beams of the two amplifiers, one of the seeds is frequency shifted before fiber coupling. The amplifier is used for the Gaussian beam of the transport lattice and the X and Y dipole traps in the glass cell (see section 5.2). Finally, part of the Gaussian beam is also used to seed the amplifier used to generate the Bessel beam. The inset at the bottom left shows the relative frequencies of all the lasers as they enter the experimental chamber.

MHz before being amplified. In conjunction with another AOM at the output, this gives a total shift of 160 MHz from the Mephisto frequency. In addition to avoiding interferences, these AOMs also allow us to stabilize and control the intensity of the dipole trap and vertical lattice.

4.2.2 Reservoir

After pre-cooling the next step would be to load the transport lattice and transport the atoms into the glass cell. However, after dRSC the cloud is cold but relatively dilute. Because of the small diameter of the Bessel beam ($<400 \mu\text{m}$), the overlap between the transport lattice and the cloud is relatively small and therefore the loading efficiency is small. In addition, the atoms that are loaded into the lattice would be compressed. This causes an increase in temperature even for adiabatic transfer as the phase space density $\phi = n\lambda_{\text{dB}}^3$ is conserved. Here $\lambda_{\text{dB}} = \frac{h}{\sqrt{2\pi mk_B T}}$ is the thermal de Broglie wavelength and n the peak density of the cloud. To match the phase space density of the dilute Raman cloud, the denser cloud trapped in the transport lattice has to increase its temperature.

We address this issue by loading the transport lattice in a three step process (Figure 4.3, Ref. [174]). We first load a large, shallow crossed dipole trap, the reservoir. The laser for the reservoir is the same as the one for the Bessel beam and the crossed trap is formed by passing the same beam through the MOT chamber twice with perpendicular polarization (Figure 4.4). To control the power in the reservoir and Bessel traps, we opted to use motorized⁶ waveplates instead of AOMs to avoid pointing instabilities and thermalization effects as these would be detrimental to the optical transport. The drawback of the motorized waveplates is that they are slow compared to an AOM, with a rotation of 45° in around 500 ms.

The reservoir beams have a diameter of 1 mm and a power of 14 W and 10 W for the first and second arm respectively. The reduction in power for the second arm is due to reflections off the vacuum viewports and sub-optimal angle of incidence on some of the mirrors along the path. This gives trap

⁶DDR25-M, Thorlabs

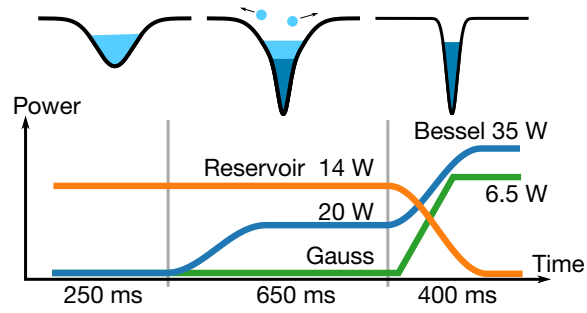


Figure 4.3 | Illustration of the loading of the transport lattice using the reservoir dipole trap. The atoms are first loaded into a shallow dipole trap. The Bessel beam is subsequently ramped up and the atoms are allowed to thermalize with those in the reservoir. Finally, the reservoir is removed and the lattice ramped up to its full depth.

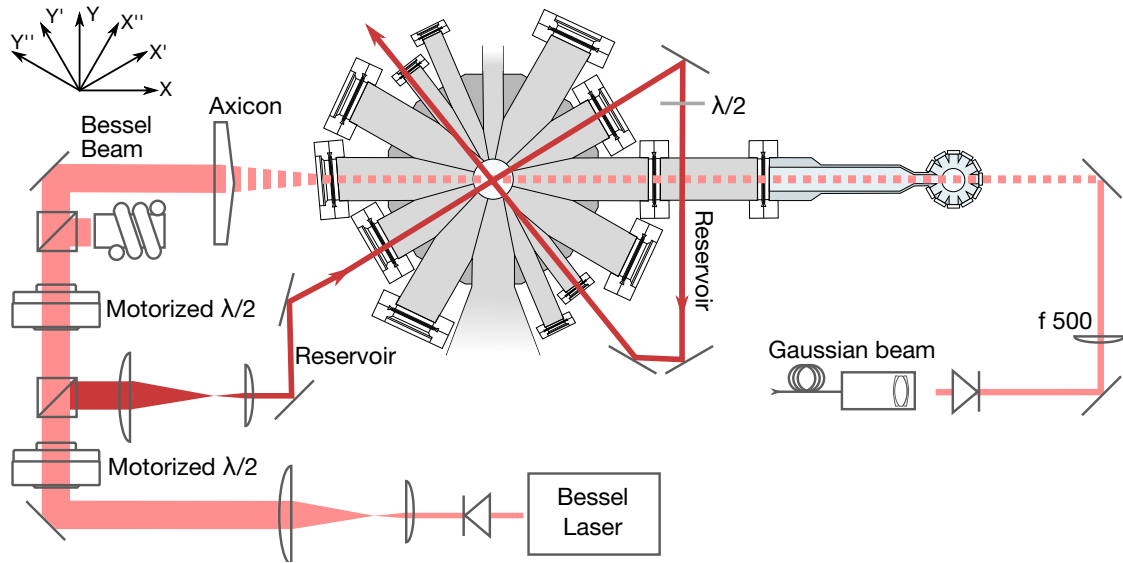


Figure 4.4 | Setup of only the reservoir dipole trap and transport lattice around the vacuum chamber. The light from the Bessel laser is used for both Bessel beam and reservoir. The relative power between them is controlled using polarizing beam splitters and $\lambda/2$ waveplates mounted in motorized rotation mounts. Counter propagating with the Bessel beam is the Gaussian.

depths of $8 \mu\text{K}$ and $6 \mu\text{K}$ and trap frequencies of $\omega_{Y'} = 2\pi \times 15 \text{ Hz}$, $\omega_{X'} = 2\pi \times 12 \text{ Hz}$ and $\omega_z = 2\pi \times 19 \text{ Hz}$. The resulting trap is large enough to capture all atoms after dRSC. It is however not strong enough to hold the atoms against gravity. We therefore apply a magnetic field gradient to levitate the atoms ($F_{\text{grad}} = \mu_B g_F m_F \partial_z B = mg \Rightarrow \partial_z B = 31.3 \text{ G/cm}$)⁷. This has the additional benefit of spin-purifying the sample, as only the atoms in $|3, 3\rangle$ are levitated against gravity. The captured atoms are heated up to match the phase space density, causing some loss from the reservoir of the hottest atoms. After 250 ms of thermalization we add the Bessel beam, which is overlapped with the reservoir. Some of the atoms in the reservoir get trapped in the deeper Bessel trap and heat up as they are compressed. However, they are still in thermal equilibrium with the atoms in the reservoir. Hot atoms in the Bessel trap scatter with colder atoms in the reservoir. The thus heated atoms in the reservoir subsequently escape from the shallow reservoir trap, leading to an evaporative cooling effect on the atoms remaining in

⁷Since Caesium in the state $|3, 3\rangle$ is a high fields seeker, the current through the upper anti-Helmholtz coil has to run in the same direction as the upper bias coil for levitation.

reservoir and Bessel trap. After another 650 ms the reservoir is removed and the Bessel power increased to its maximum. As the reservoir is removed, the Gaussian beam is ramped up to keep the atoms from spreading along the transport axis.

Other loading schemes Initially we did not try and load the transport lattice using a shallow reservoir trap. Instead, we started out with a crossed dipole trap formed by the Gaussian beam (or Bessel beam) of the transport lattice (entering from the glass cell, or MOT chamber side for the Bessel beam) and a second dipole trap entering the chamber at a 30° angle w.r.t. the transport axis. In addition, we chose the waist of this second dipole trap such that the trap would be steep enough to hold the atoms against gravity. However, using this dipole trap configuration we were faced with a relatively low confinement along the transport axis and a large temperature increase when loading the Raman cooled cloud into the dipole trap. This led to a relatively low atom number captured in the transport lattice, compared to the current scheme with a crossed dipole trap of much larger waist.

We have also tried to cool the atoms after they are loaded in the reservoir or transport lattice. To cool the atoms after loading them into the reservoir, we pulsed the degenerate Raman sideband cooling sequence. The idea was to let the atoms evolve in the dipole trap potential for a quarter period and switch the Raman lattice back on when the density in the dipole potential was maximal [175, 176] (See also Ref. [159], p.47). The density would increase, while the temperature would remain the same as after regular dRSC. This scheme did help a bit in increasing the atom number trapped in the original (small waist) crossed dipole trap. However, after switching to the reservoir trap we could not use the scheme anymore, as we required a magnetic field gradient to keep the atoms in the trap, which interfered with the Raman cooling. Turning the gradient on and off was not an option since we could not switch off and on the gradient fast enough.

We also tried cooling the atoms after they were loaded into the transport lattice. Here, we tried to implement the scheme from Ref. [177]. The polarizations between the two lattice arms are slightly tilted with respect to each other. We managed to increase the phase space density measured directly after transport using this scheme. However, the PSD would not increase as efficiently during the following evaporation stages. We attributed this to the fact that after the Raman cooling in the 1d lattice not all atoms were in the $|3, 3\rangle$ state, but some were in other hyperfine states ($|3, 2\rangle$, $|3, 1\rangle$) were observed in the glass cell using microwave spectroscopy), leading to more inelastic collisions.

4.2.3 Transport lattice

The transport lattice is formed from the interference of a Bessel and Gaussian laser. We need to be able to control the relative detuning of the lasers precisely in order to start and stop the atoms at different positions. As the transport velocity scales linearly with the detuning between the laser beams ($v = \lambda\Delta f/2$), a larger detuning bandwidth enables faster transport. Because in optical transport with a lattice the axial trap frequency is quite large, high accelerations on the order of km/s^2 are possible before atoms start to be lost. So in addition to having a large detuning bandwidth, we want to be able to quickly ramp the detuning.

Because we are using two externally seeded fiber amplifiers, we can split off light from one amplifier, shift it using double pass AOMs and use it to seed the other (Figure 4.5). This avoids relative drifts between the lasers, and they do not have to be locked to one another. Double pass AOM setups allow us to shift the frequency quickly and over a broad range, and no AOMs need to be placed in the amplifier output. We therefore don't have to worry about thermal lensing or pointing drifts induced by the AOM crystal.

In our experiment, we use light from the Gaussian to seed the Bessel. The seed passes through two double pass AOM setups, optimized for -225 MHz and 175 MHz respectively. Running at these

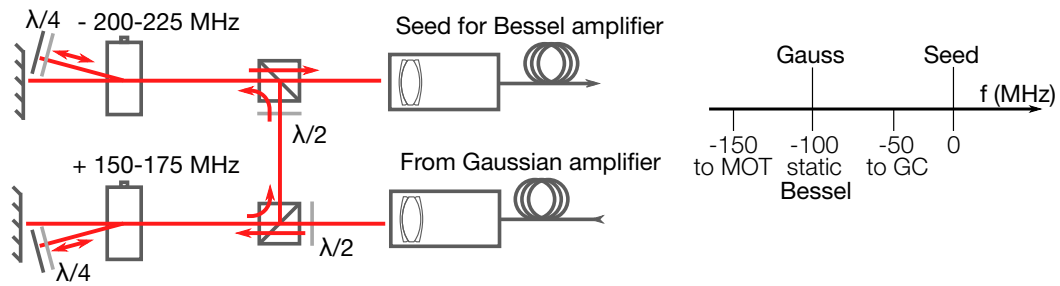


Figure 4.5 | DPAOM setup for seeding the Bessel amplifier from light taken from the Gaussian amplifier. The frequency is first shifted to higher, then to lower frequencies. Depending on the relative detuning, the atoms are either transported to the MOT or the glass cell (see right plot)

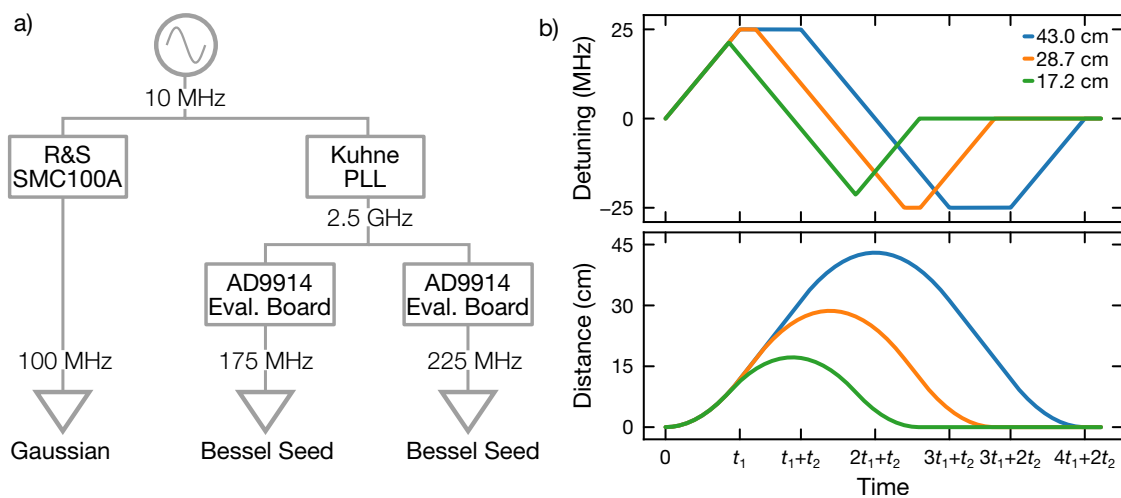


Figure 4.6 | a) Frequency generation setup for the Gaussian intensity stabilization and the two DPAOMs in the Bessel laser seeding setup. b) Exemplary frequency detuning ramps used to transport atoms to the glass cell and back to the MOT chamber (see also subsection 4.3.1). Using $\Delta f_{\max} = 25$ MHz and $a = 2.8$ MHz/ms. Different colors correspond to different transport distances. $t_1 = 8.9$ ms is the duration of the frequency ramp and $t_2 = 7.3$ ms the time between the start and stop frequency ramp and are indicated for the blue curve (see Equation 4.1). For the green curve, the frequency ramp duration t_1 is insufficient to reach Δf_{\max} .

frequencies, the output is shifted by -100 MHz to the same frequency as the Gaussian beam after it passes through its intensity stabilizing AOM. The subsequently amplified seed therefore produces a standing wave when interfering with the Gaussian beam. By ramping the frequency of the -225 MHz AOM to -200 MHz the standing wave turns into a running one travelling towards the glass cell. Ramping the frequency back to -225 MHz stops the atoms, and ramping the other AOM to 150 MHz drags the atoms back to the glass cell.

To control the frequency of the AOMs we use two AD9914 DDS evaluation boards (Figure 4.6a). We initially used signal generators to produce the frequencies for the DDS board. The ones we tested were however not well suited for the task⁸. They did not have the option to program and externally trigger a linear frequency ramp. Instead, when specifying a frequency step and step duration (dwell time) for a sweep, the signal generator would increment the frequency by the given amount and fix the frequency for the given step duration. However, when changing the frequency the output of the signal generator became unstable. This was the expected behaviour, the dwell time essentially only

⁸SMY01, Rhode&Schwarz

specified the duration for which the output frequency was certain to be within some band around the set frequency. We also tried to control the signal generators' output using the analog modulation input. This however implied that either the bandwidth of detuning was very small or the output frequency was extremely sensitive to noise on the analog signal. We found that for large detuning bandwidth, the analog modulation input stability was insufficient for transport to the glass cell.

Using a DDS chip for the frequency generation allowed for essentially arbitrarily fast, broadband frequency ramps. There is no time window where the output frequency is unstable between steps (Figure 4.7). The temporal and frequency step size during the ramp is limited by the system clock for the DDS. For the 2.5 GHz system clock we are using, these are $\Delta f_{\min} = 580$ mHz and $\Delta t_{\min} = 9.6$ ns. The DDS board has an internal VCO and PLL loop, which would allow one to generate the 2.5 GHz system clock with a slower signal (e.g. 10 MHz). However, another experiment in our group made the experience [178] that for a different DDS chip⁹ the internal PLL loop is not particularly good. We therefore supply our own 2.5 GHz clock¹⁰, locked to a 10 MHz signal from a Rb reference clock. This same clock is also used for the signal generator¹¹ supplying the 100 MHz for the Gaussian beam's intensity stabilization AOM.

Given the linear rate of change to the laser detuning $2\Delta f_{\text{rate}}$ and the maximum detuning $2\Delta f_{\text{max}}$, the velocity and acceleration are given as $v_{\text{max}} = \lambda\Delta f_{\text{max}}$ and $a = \lambda\Delta f_{\text{rate}}$. The factor 2 in the laser detuning rate and amplitude is due to the double pass AOM setup and cancels with a factor 2 in the formulas for v_{max} and a . The laser detuning is varied linearly. Define t_1 the time of the stop of the linear acceleration ramp and t_2 , the time between the end of the acceleration ramp and the start of the deceleration ramp as:

$$t_1 = \begin{cases} \frac{v_{\text{max}}}{a} & d > \frac{v_{\text{max}}^2}{a} \\ \sqrt{\frac{d}{a}} & d < \frac{v_{\text{max}}^2}{a} \end{cases} \quad t_2 = \begin{cases} \frac{d}{v_{\text{max}}} - t_1 & d > \frac{v_{\text{max}}^2}{a} \\ 0 & d < \frac{v_{\text{max}}^2}{a} \end{cases}. \quad (4.1)$$

Here d is the distance to be transported. The position and velocity during transport is then given as

$$x = \begin{cases} \frac{1}{2}at^2 & t < t_1 \\ x(t_1) + v_{\text{max}}(t - t_1) & t_1 \leq t \leq t_1 + t_2 \\ x(t_1 + t_2) + v_{\text{max}}(t - t_1 - t_2) - \frac{1}{2}a(t - t_1 - t_2)^2 & t_1 + t_2 < t \end{cases} \quad (4.2)$$

$$v = \begin{cases} at & t < t_1 \\ v_{\text{max}} & t_1 \leq t \leq t_1 + t_2 \\ v_{\text{max}} - a(t - t_1 - t_2) & t_1 + t_2 < t \end{cases} \quad (4.3)$$

Exemplary ramps to illustrate the above equations are shown in Figure 4.6b. Linear ramps of the velocity are easier to implement, but are not ideal when trying to avoid heating during transport. The heating after the transport has ended can be estimated from the amplitude of the Fourier transform of the velocity profile at the trap frequency of the lattice. For our linear frequency ramps, assuming a triangular velocity profile and oneway transport for simplicity, we have

$$v(t) = v_{\text{max}} \text{Tri}\left(\frac{t}{T}\right) \quad (4.4)$$

$$v(\omega) = \frac{v_{\text{max}}T}{\sqrt{2\pi}} \text{sinc}^2\left(\frac{\omega T}{2}\right), \quad (4.5)$$

⁹AD9910, Analog Devices

¹⁰KU LO 2500 PLL-849, Kuhne; Splitter ZB 8PD-362-S+, Mini Circuits

¹¹SMC 100A, Rhode & Schwarz

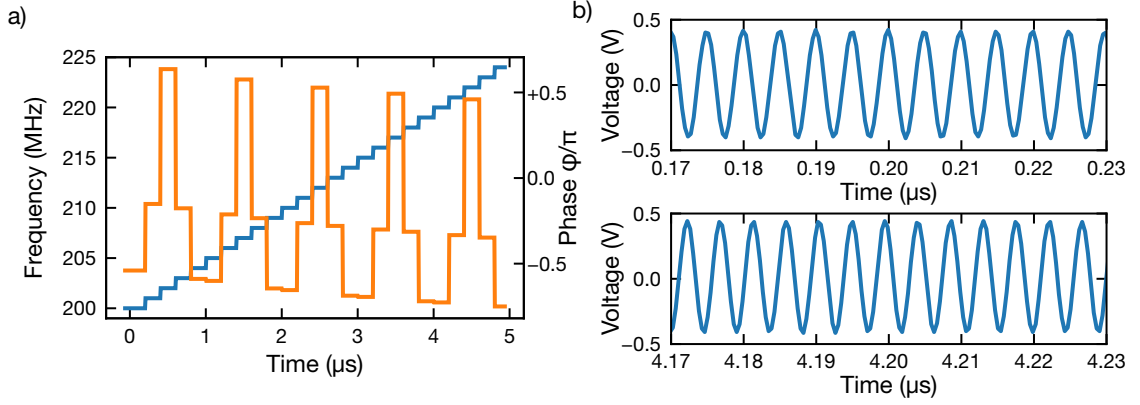


Figure 4.7 | Illustration of the frequency ramps generated by the DDS board. **a)** Change of the frequency (blue) and phase (orange) during a ramp of the DDS from 200 MHz to 225 MHz with frequency step size of 1 MHz and frequency step rate of $1/0.2 \mu\text{s}$. **b)** Measured DDS output signal at the transition between frequency steps (blue). The steps are at $0.2 \mu\text{s}$ in c) and $4.2 \mu\text{s}$ in d).

where v_{max} is the maximum velocity, T the transport duration and Tri the unit triangular function. For our typical transport durations of around 25 ms and lattice trap frequencies of around $\omega_{\text{latt}} = 2\pi \times 60 \text{ kHz}$, the expected oscillation amplitude is around $0.08 \ell_0 = 2.7 \text{ nm}$, with $\ell_0 = \sqrt{\hbar/m\omega_{\text{latt}}}$ the harmonic oscillator length. The heating due to the abrupt start of the transport can be reduced by more involved transport ramps [179–182]. In the simplest case, the acceleration profile is simply linear and the associated displacement of the atoms follows a cubic profile [167, 181].

We control the frequency ramps by setting the DRCTL pin of the DDS board to high (ramp to high frequency) or low (ramp to low frequency). The ramp to higher frequencies starts the moment the DRCTL pin is set high and stops after reaching Δf_{max} . The inverse ramp, to lower frequencies, is started immediately when the DRCTL pin is set low (i.e. the current ramp does not finish before inverting the ramp). Note that the DDS board discretizes the frequency ramp. During programming a frequency step size Δf_{step} and a frequency step rate $1/\tau$ is specified. However, the signal changes continuously, i.e. the phase of the signal after the step is chosen such that there is no abrupt change of the signal voltage when the frequency is changed (see Figure 4.7a). Figure 4.7b illustrates the effect of varying the phase as well as the frequency at two frequency steps. The plots show the measured frequency output around two representative frequency steps.

4.2.4 Bessel beam

Like a Gaussian beam, a Bessel beam is a solution to the Helmholtz equation $(\nabla^2 + \vec{k}^2)E(x, y, z) = 0$. The Bessel beam solution has the form

$$E(x, \rho) = \exp[i\beta x]J_0(\alpha\rho), \quad (4.6)$$

where $y^2 + z^2 = \rho^2$, x is the propagation direction, $\vec{k}^2 + \vec{k}^2 = \vec{k}^2$ and J_0 the zeroth order Bessel function of the first kind (Figure 4.8a). It is non-diffracting, i.e. the size of the beam profile does not depend on x . Expressing the Bessel function as an integral

$$J_0(\alpha\rho) = \int_0^{2\pi} \exp[i\alpha(y \cos \phi + z \sin \phi)]d\phi/2\pi, \quad (4.7)$$

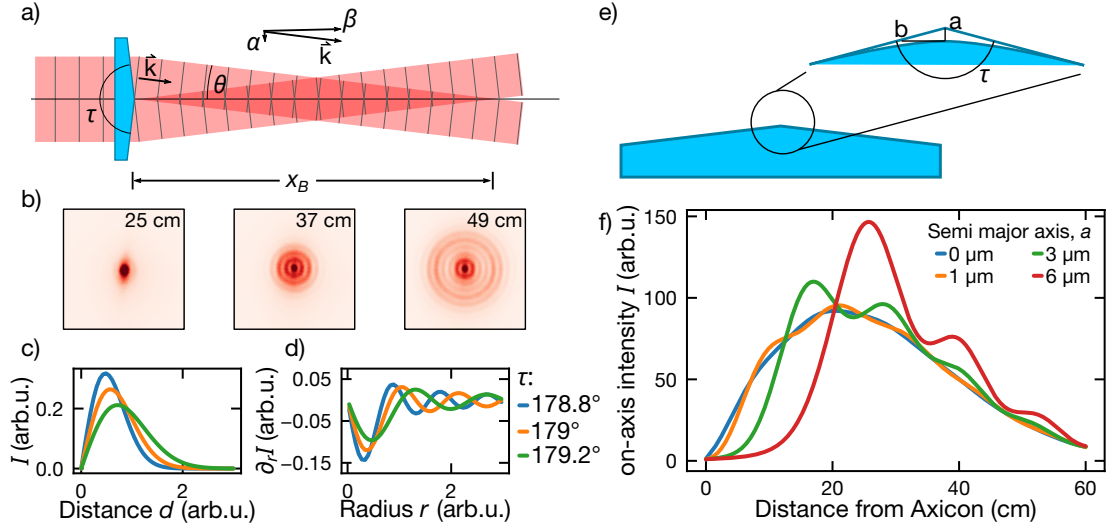


Figure 4.8 | **a)** Bessel beam formation with an axicon. The axicon has an opening angle τ . After passing through the axicon, the incident plane waves have a wavevector \vec{k} with radial component $\alpha = |\vec{k}| \sin \theta$ and axial component $\beta = |\vec{k}| \cos \theta$. The interference of the plane waves generates a Bessel beam over a distance x_B . **b)** Sample profiles of the Bessel beam. The distance between the profile and the axicon is indicated in the images. The incident Gaussian beam has a diameter of 5.3 mm. **c)** Intensity of the Bessel beam versus distance for three different axicon apex angles. In the experiment, the axicon angle 179° is used. **d)** Radial derivative of the intensity of the Bessel beam for three different axicon apex angles. The optical potential gradient due to the Bessel beam is proportional to the radial derivative. A large derivative implies that trapped atoms are held against gravity at lower intensity. **e)** Schematic of a round tip axicon. The round tip is approximated as a hyperboloid with semi major axis a and linear eccentricity $\sqrt{a^2 + b^2}$. **f)** Effect of the round tip on the axial intensity. The intensities were computed numerically for different axicon semi major axes a .

one sees that the Bessel beam may be interpreted as a superposition of plane waves with an angle $\sin \theta = \alpha/|\vec{k}|$ with the optical axis [183] (Figure 4.8a). These Bessel beams may therefore be generated from a plane wave using an axicon [184–186], a type of lens with a conical cross-section instead of the typical spherical one. Given the apex angle of the axicon τ , the angle of the interfering plane waves is found to be

$$\theta = \arcsin \left[n \sin \left(\frac{\pi - \tau}{2} \right) \right] - \frac{\pi - \tau}{2} \stackrel{\tau \approx \pi}{\approx} \frac{\pi - \tau}{2} (n - 1), \quad (4.8)$$

where n is the refractive index of the axicon. The axicon used in the experiment¹² is made from fused silica, has a diameter of 1" and an apex angle $\tau = 179^\circ$. Other ways of producing Bessel beams include placing a circular aperture one focal length before a singlet lens [187], using holographic optical elements [188, 189], Mach-Zehnder interferometers [190] or diffractive phase elements [191].

An axicon transforms an infinitely extended plane wave into the ideal Bessel beam exactly. A finitely extended plane wave reproduces the non-diffracting Bessel beam over a finite range $x_B = w_0 / \tan \theta$, determined by the opening angle of the axicon τ via Equation 4.8 and the radius of the incident plane wave w_0 (Figure 4.8a).

¹²XFL25-005-U-U, C-coating, Asphericon

Typically, one works with Gaussian beams instead of perfect plane waves. In this case [186], the peak intensity becomes dependent on z

$$I_{\text{BG}}(x, \rho) = I_0 J_0^2(\alpha \rho) \frac{2\pi \alpha x w_0}{x_B} \exp\left[\frac{-2x^2}{x_B^2}\right], \quad (4.9)$$

where $I_0 = 2P/\pi w_0^2$ is the peak intensity of the incident Gaussian (Figure 4.8c,d). The x dependence is due to the radial intensity dependence of the Gaussian leading to a decreasing intensity of the interfering plane waves on the optical axis. The peak intensity is at $x = x_B/2$ with $I_{\text{BG,max}} = I_0 \pi \alpha w_0$. Increasing the apex angle τ increases the Bessel range x_B at the cost of a lower on-axis intensity and a larger radius ($\alpha \propto \frac{\pi-\tau}{2}(n-1)$ for $\tau \approx \pi$).

In addition, real axicons have rounded tips due to fabrication (Figure 4.8e). These lead to a modulation of the central spot's intensity. This may be intuitively understood by separating the round tip axicon into a spherical lens in the center and a perfect axicon ring around it [186]. The lens part focuses the central spot of the incident Gaussian and produces a new Gaussian beam. This copropagates with the Bessel-like beam produced by the perfect axicon ring. The two beams interfere, resulting in a modulation of the intensity. Additionally, the round tip leads to a lower than expected intensity immediately behind the axicon. Ref. [186] gives the expected electric field directly behind the axicon for such a round tip axicon. In Figure 4.8f, this field was propagated numerically [192] for different semi major axes values a .

To estimate the trap depth along the transport axis, we have measured the beam profile of a Bessel beam resulting from Gaussian beams with different diameters passing through our axicon (Figure 4.8b). We don't observe a fully formed Bessel beam immediately behind the axicon. Instead the beam starts out Gaussian shaped and transforms into a zeroth order Bessel-like beam after a few cm of propagation. As the beam propagates, the intensity of the rings around the central spot tends to increase and the intensity of the central spot tends to decrease. However, the radius of the central spot remains fairly constant over a distance greater than 50 cm for sufficiently large incident beams. At some point, the central spot appears to vanish and the beam starts to resemble a doughnut mode. All this is in good agreement with the expectation from a round tip axicon.

To analyze the taken images more quantitatively and use them to estimate dipole and lattice depth, we have fitted each image. We crop the image around the central spot and fit either a 2D Gaussian or a 2D Bessel profile, depending on whether or not rings are visible on the image. In addition we estimate the laser power in the full beam by performing a pixel sum over the whole, uncropped image. This step is necessary because in order to measure the profiles further away from the axicon, the exposure time of the camera had to be changed. By extracting the total power, each fitted Gaussian or Bessel beam can be scaled to a common optical power level. From the thus extracted power we estimate the peak intensity in the central spot by computing the ratio of the peak pixel value to the power. We do not use the previously fitted amplitude because this typically underestimates the peak intensity of the Bessel beam (Figure 4.9a).

Figure 4.9 shows the beam diameter (c) and peak intensity (b) versus distance from the axicon for a Gaussian beam with a waist of $w_{\text{in}} = 5$ mm before the axicon. The beam diameter initially drops and eventually levels off with some small amplitude modulation. We extract a $1/e^2$ beam radius of 80–100 μm . The peak intensity initially increases before falling off again further away from the axicon. Also, the fall off is not continuous but exhibits a small modulation. This modulation can be approximately reproduced by using the round tip axicon model.

From the fits, we can estimate the trap depth (Figure 4.9d) and lattice depth (Figure 4.9e) along the transport. For the counter propagating Gaussian, we use the beam waist (179 μm) and its position, measured by reflecting the beam before it enters the glass cell. The potential depth along the direction of gravity (z), taking gravity into account, is dominated by the Bessel beam. It increases rapidly at the start of the transport to 150 μK and then drops off. At the center of the glass cell, the trap depth is around 18 μK . Meanwhile, the lattice depth ramps up similarly to the trap depth along z but peaks

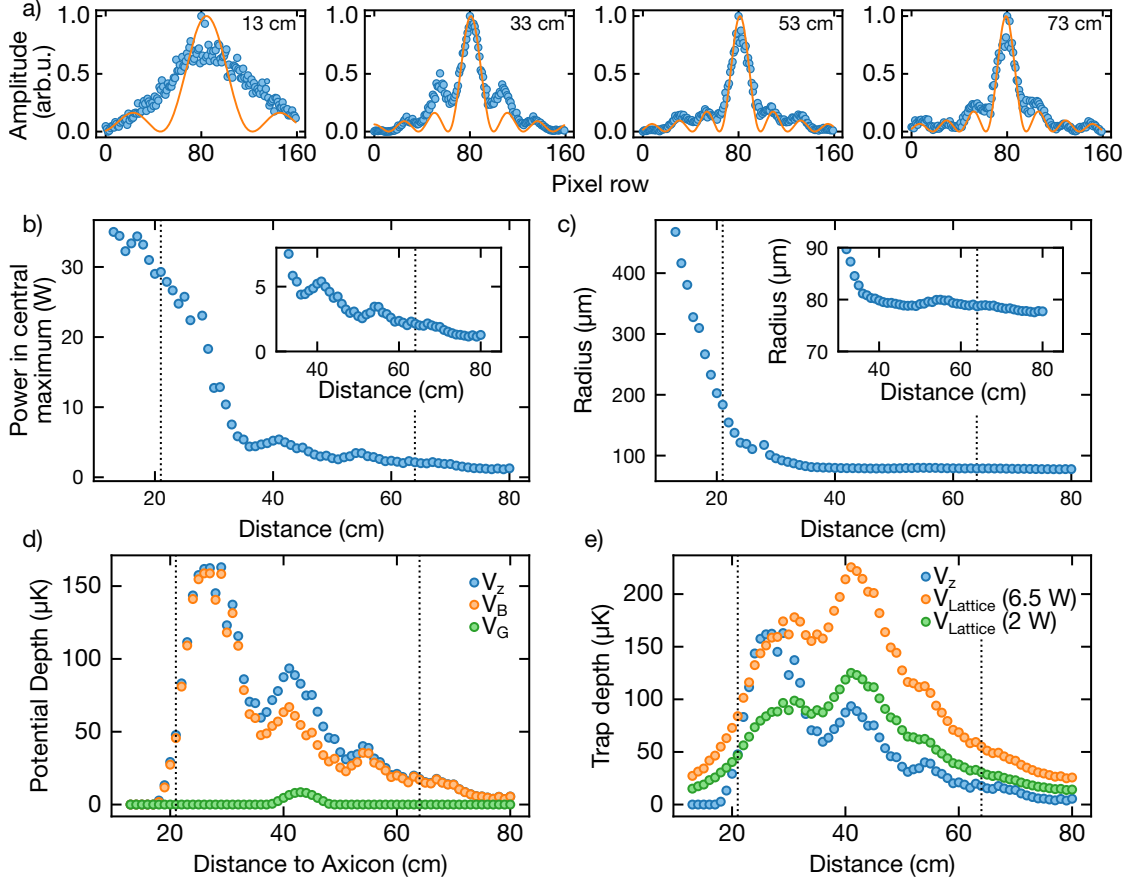


Figure 4.9 | **a**) Sample fits of a Bessel beam profile (orange) to the measured beam profiles (blue points). The distance from the axicon is indicated in the top right. The plots show crosscuts through the image and fit at the peak pixel value position. **b**) Power in the central spot of the Bessel beam as a function of the distance from the axicon. The total power before the axicon is 35 W. The inset shows the power between 30–80 cm. **c**) Fitted radius of the Bessel beam profile as a function of the distance from the axicon. Shown is the $1/e^2$ waist of the central spot. **d**) Potential depth in the z direction versus distance from the axicon, taking gravity into account. The potential solely due to the Bessel V_B is plotted in orange, the one solely due to the Gaussian V_G is shown in green and the combined trap of Bessel and Gaussian V_z is shown in blue. **e**) Lattice depth versus distance from the axicon for two different powers of the Gaussian beam ($P_G = 6.5$ W in orange and $P_G = 2$ W in green). For comparison the vertical potential depth V_z is also shown (blue).

later at around $240 \mu\text{K}$ (power of Gaussian beam $P_G = 6.5$ W). The lattice depth remains larger than the trap depth for the rest of the transport distance.

For our transport we were also worried about pointing drifts and fluctuations of the beam (see also Ref. [193]). We measured pointing drifts and fluctuations before installing the laser on the experiment table. In order to characterize the pointing fluctuations we can expect over the transport distance, we placed a four quadrant photodiode (4QP¹³) 65 cm behind the output of the 45 W ALS laser we planned to use for the Bessel beam. We performed two measurements, one with just waveplates and polarizing beamsplitters inserted into the beam path to reduce the power and another with the axicon placed 45 cm from the 4QP and an isolator and telescope inserted into the beam path. This second measurement roughly corresponds to the final setup we have around the experiment. In order to avoid the effect of the Bessel rings distorting the second measurement, we have placed an iris before the 4QP.

¹³QP45-Q, First Sensor

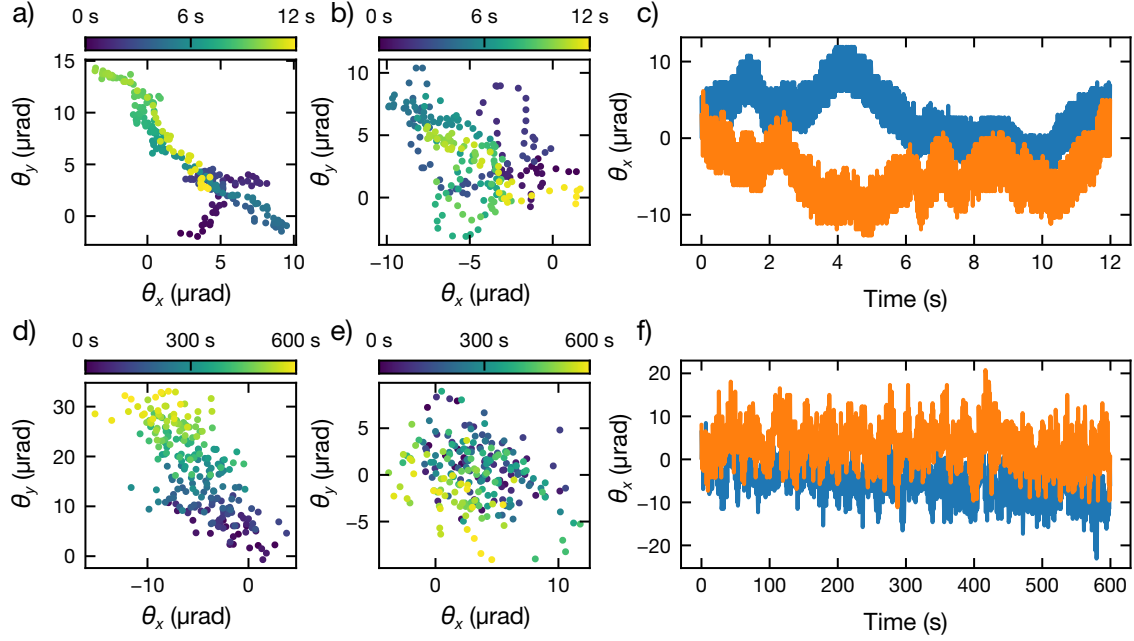


Figure 4.10 | Pointing drifts during warm-up (a,d) and after the laser was running for 30 minutes (b,e), plotted as deviation of the pointing angle. The distance between the 4QP and axicon was 45 cm. Color indicates time, the range of which is indicated in the colorbar above each plot. (c) and (f) show the time trace of the pointing fluctuations in the horizontal direction on short (c) and long (f) timescales. The warm-up phase is blue, the running laser measurement is shown in orange. A change of $10 \mu\text{rad}$ corresponds to a change of around $6.5 \mu\text{m}$ at the position of the atoms.

We found relatively small drifts and fluctuations of the pointing after some thermalization of the amplifier, on the order of $10 \mu\text{rad}$ (Figure 4.10). These are relatively slow, on the order of 1 s. We therefore were quite confident that we would not need to think of additional pointing stabilization schemes for the transport.

Using two Gaussians Considering the relatively small size of the central spot of the Bessel beam and the fact that far from the atoms only a small percentage of the total power is actually contained in the central spot, one may consider using two Gaussian beams for the transport. Though Gaussian beams will diffract, it might be possible to work with larger waists and two Gaussians to hold the atoms against gravity. For the distance in our experiment and the axicon we use, the Bessel-Gauss lattice combination gives favorable lattice and trap depths at the same total laser power available. For this comparison, I chose the Gaussian Rayleigh range z_R to be half the total transport distance and the waist position to be $3/4z_R$ from the start and end of the transport distance for the two beams. This configuration gives comparable trap depth in the center of the transport distance and the start and ends. In addition, the transport lattice configuration made from two Gaussians is potentially more sensitive to alignment between the Gaussian beams since the beam that holds the atoms against gravity changes during transport. We have noticed something similar during early stages of working with our transport configuration. At that time, we had the Gaussian beam focused in the MOT chamber to hold and capture the atoms and had moved the axicon closer to the glass cell. This way the Gaussian would hold the atoms initially, and the Bessel beam would supply the confinement against gravity towards the end of the transport. The idea was that the Gaussian, being larger in waist, would capture more atoms from the Raman cloud. As the Bessel beam is initially very Gaussian like and then starts to compresses to form the actual Bessel beam (cf. Figure 4.8b), the atoms would be compressed into the

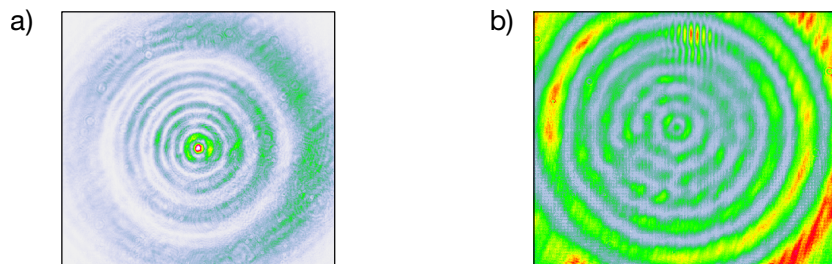


Figure 4.11 | a) Bessel profile with sub-optimal alignment, where the power in the outer rings is distributed asymmetrically. b) Better alignment makes the power distribution in the rings more symmetric. Note that the two images were taken at different positions and with different color scales, hence the different intensities in the rings.

central maximum of the Bessel beam during the transport, and thus more atoms would be transported into the glass cell. This setup did not work for us. Instead we found that a large number of atoms were lost a short distance from the MOT chamber. This might be because the atoms are not compressed into the central peak of the Bessel beam as we expected, the system is significantly more sensitive to the precise alignment between the Bessel and Gaussian beam or the compression increased the temperature of the atoms too much and they were lost from the trap.

4.2.5 Alignment of the transport lattice

For initial alignment through the chamber, we set up an imaging system along the transport axis. We first image the atoms in the MOT chamber along that axis and subsequently align the Bessel beam on the camera. This was only necessary once at the very beginning. Since then, fine alignment of the Bessel beam pointing is possible by maximizing the atom number trapped in the transport lattice after removing the reservoir. This is rarely necessary once optimized, only if significant work on the experiment table (installing new breadboards for instance) was performed.

For maximum transport efficiency we have found that the Bessel profile at the exit of the glass cell should be as symmetric as possible (Figure 4.11). To ensure that all required degrees of freedom are available, the axicon is mounted in a four axis mount (tip, tilt and displacement perpendicular to the optical axis). From our experience, it is not obvious from the Bessel beam profile at the glass cell axis which of the degrees of freedom need to be touched to improve the Bessel profile. To some degree, displacement and tilt along one axis are interchangeable. Typically however we tune the displacement. After tuning the axicon orientation and placement, the beam will have moved. We therefore follow an iterative procedure, where we maximize the atoms loaded into the transport lattice and then the Bessel beam profile. Note that this does not fix the position of the atomic cloud at the glass cell. This we typically do not try to do.

Aligning the Gaussian on the Bessel beam is relatively straight forward. The beams are simply overlapped at two points. The Bessel beam becomes ring shaped about 30 cm behind the glass cell. Here, the Gaussian can be aligned to the center of the Bessel beam. Note that we have found that the overlap needs to be quite good to be able to transport the atoms all the way to the glass cell. Once some atoms arrive in the glass cell, this atom number can be maximized by further tuning the alignment.

4.2.6 Magnetic fields during transport

We were initially worried about the magnetic field during transport. The cloud loaded from the reservoir into the optical lattice is purely $|3, 3\rangle$ polarized. This is, to my knowledge, the only internal state of Caesium people have been able to condense. As such, we do not want any depolarization of the cloud

during transport, as this would necessitate an additional spin purification in the glass cell and therefore fewer available atoms. We keep the magnetic offset field in the MOT chamber on during transport (23 G in the center of the MOT chamber) and ramp up the offset field in the glass cell before transport (28.2 G). There are no additional bias coils to keep a fixed quantization axis during transport. The transport passes underneath an IGP¹⁴ (Figure 3.10), which adds a small magnetic field (about 1 G). We do not observe any spin depolarization after transport as measured using microwave spectroscopy.

4.3 Optical transport

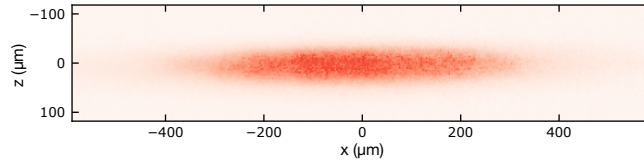


Figure 4.12 | Absorption image of the cloud after transport to the glass cell

Having loaded the atoms into the transport lattice, we can start the transport to the glass cell (Figure 4.12). We only vary the frequency of one DDS board. This is mostly for convenience, as we sometimes need the second DDS board to transport the atoms back to the MOT chamber. As the transport duration is already relatively short, we decided to keep the second DDS board programmed, and second DPAOM setup optimized for transport back to the MOT chamber. Typically, the DDS ramp settings are $f_{\text{low}} = 200$ MHz, $f_{\text{high}} = 225$ MHz for the first DDS board and $f_{\text{low}} = 150$ MHz and $f_{\text{high}} = 175$ MHz for the second DDS board. The frequency step size for both boards is 550 Hz and the frequency step rate is $0.2 \mu\text{s}$. The counter propagating Gaussian beam typically has a power of 6.5 W.

With these settings, we transport around 3×10^6 atoms to the glass cell out of 4×10^6 loaded into the transport lattice in 25.1 ms over the 43 cm transport distance. After transport the atoms have a temperature of $5 \mu\text{K}$ compared to $10 \mu\text{K}$ before transport.

4.3.1 Round trip measurements

Because we cannot reprogram the DDS boards within the sequence, we perform round trip transport by using one of the DPAOMs to transport the atoms towards the glass cell and the other to transport the atoms back towards the MOT chamber. Round trip measurements allow us to characterize the transport efficiency versus transported distance. As such, they are useful for checking for alignment errors between Gaussian and Bessel beam. In case the alignment between Gaussian and Bessel is not optimal, the atoms may not be transported all the way to the glass cell but only part of the way. Apart from this, we can also use round trip measurements to try and understand the limitations of the transport.

To this end, we repeatedly transport the atoms from the MOT chamber towards the glass cell and back. By varying the timing between setting the DRCTL pin to high or low we control the transport distance. Specifically, the transport to the glass cell starts with setting the pin on the 225 MHz AOM to low at $t_{\text{low}} =$

¹⁴Titan 10ST, Gamma Vacuum

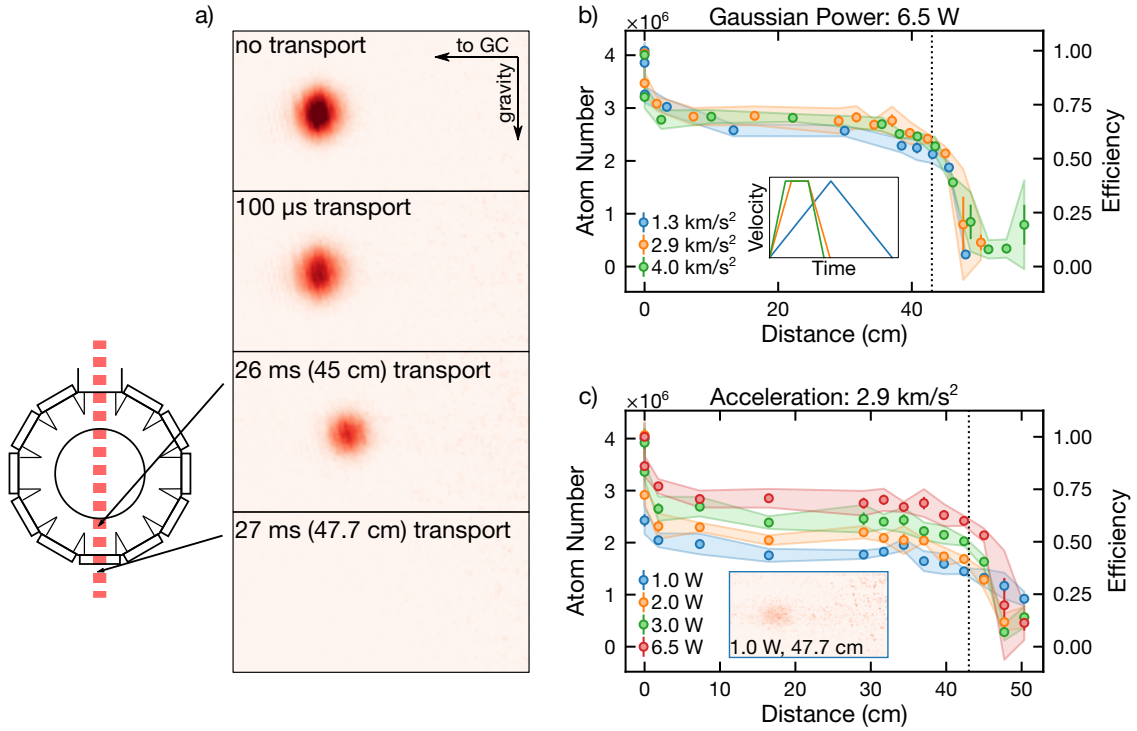


Figure 4.13 | a) Sample images taken in the MOT chamber of round trip transported atoms taken at $P_G = 6.5$ W and $a = 2.9$ km/s². The given duration and distance refers to the one-way transport duration and distance. The first two images (0 ms and 100 μ s illustrate the immediate loss of atoms at the start of the transport. The second pair of images illustrate the complete loss of round trip transported atoms once the atoms crash into the glass cell's exit viewport. The offset between the cloud center in the first image pair and second image pair is due to a slight difference in transport duration for the transport to and from the glass cell. This difference is used during the experiment to visualize to the experimenter whether the atoms are transported at all and is not present in case there is no or negligible transport. b) Round trip transport efficiency for three different accelerations and $P_G = 6.5$ W. Left vertical axis shows atom number measured in the MOT chamber after transporting, on the right vertical axis all data points were normalized to the mean atom number at 0 cm transport distance and $P_G = 6.5$ W, averaged over all accelerations. The dashed line indicates the center of the glass cell, 43 cm. Beyond 47 cm the transported atoms have crashed into the glass cell exit viewport and do not return to the MOT. The inset shows the one-way velocity ramps for the transport to the center of the glass cell for the different accelerations. c) Round trip transport efficiency for four different powers P_G . Axes and dashed line as in b). The inset shows the transported cloud at $P_G = 1$ W and after $d = 47.7$ cm transport distance, where no transported atoms return to the MOT chamber. Due to the low lattice depth, quite a few atoms remain in the MOT chamber and are not transported at all. The color scale in the inset is different from the one in a) with the maximum color (dark red) being lower by a factor of 3. In all plots circles denote the mean of 5 repetitions, error bars correspond to the standard error of the mean and the shaded area corresponds to one standard deviation. The error bars are often smaller than the marker size.

0 s. The distance traveled can be computed from t_{high} , the time where the pin is set high and the frequency ramp to 225 MHz starts. Using the notation introduced above (cf. Figure 4.6b and Equation 4.1)

$$t_1 = \begin{cases} \frac{\Delta f_{\text{max}}}{\Delta f_{\text{rate}}} \\ t_{\text{high}} \end{cases}, \quad t_2 = \begin{cases} t_{\text{high}} - t_1 \\ 0 \end{cases}, \quad d = \begin{cases} \lambda[\Delta f_{\text{rate}} t_1 + \Delta f_{\text{max}}(t_{\text{high}} - t_1)] \\ \lambda \Delta f_{\text{rate}} t_{\text{high}} \end{cases} \quad \begin{matrix} t_{\text{high}} > \frac{\Delta f_{\text{max}}}{\Delta f_{\text{rate}}} \\ t_{\text{high}} \leq \frac{\Delta f_{\text{max}}}{\Delta f_{\text{rate}}} \end{matrix}. \quad (4.10)$$

After the second ramp has finished, the atoms have stopped at some distance from the glass cell. To transport them back to the MOT chamber, the second DDS board's frequency (the 175 MHz one) is

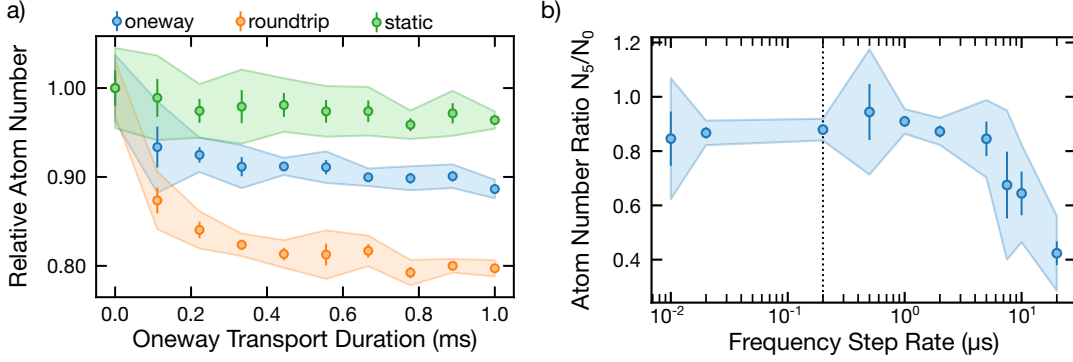


Figure 4.14 | a) Loss in atom number for short transport durations. The atoms are either transported towards the glass cell for a short duration (oneway, blue), transported back and forth for a short duration (round trip, orange) or not transported at all (static, green). In all cases the atoms are imaged in the MOT. For the one-way transport, the transport duration is insufficient to remove them from the imaging area. The circles denote the mean, errorbars are the standard error of the mean and the shaded area corresponds to one standard deviation. Starting the transport ramps leads to almost immediate and dramatic loss of atoms on the order of 20-25%. The round trip measurement is about a factor of two worse than the one-way measurement. The measurements series were normalized separately to the mean atom number without transport. For these measurement $a = 2.9 \text{ km/s}^2$ and $P_G = 6.5 \text{ W}$. **b)** Ratio of atom number after a $d = 5 \text{ cm}$ round trip and without transport versus the frequency step rate of the frequency ramp. The frequency step size was adjusted to keep the acceleration fixed at $a = 2.9 \text{ km/s}^2$. The dashed line indicates the regular frequency step rate. The transported atom number starts to drop for step rates greater than $5 \mu\text{s}$.

ramped using the same $\Delta t = t_{\text{high}} - t_{\text{low}}$, which transports the atoms back to the starting position in the MOT chamber.

We investigate the dependence of the round trip transport on the acceleration a and power of the Gaussian beam P_G (Figure 4.13). The general form of the atom number as a function of transport distance d shows a sharp drop at the start of the transport. This happens nearly instantaneously, for a transport duration of $100 \mu\text{s}$ the atom number is already reduced by 20–25%. This is followed by a plateau of almost constant transport efficiency, that slowly drops off towards the center of the glass cell. Finally, transporting the atoms into the exit viewport of the glass cell ($d \gtrsim 47 \text{ cm}$) leads to complete loss of the transported atoms and the only atoms that remain are those that were not transported at all. For round trips to the center of the glass cell ($d = 43 \text{ cm}$) and back (dashed line in Figure 4.13b–c) and $P_G = 6.5 \text{ W}$, $a = 2.9 \text{ km/s}^2$ we find around 2.3×10^6 atoms remaining out of 4×10^6 atoms, corresponding to 57.5%.

Varying the acceleration does not appear to have a significant effect on the transport efficiency (Figure 4.13b). For very low accelerations ($a = 1.3 \text{ km/s}^2$) the transport efficiency is slightly lower for longer transport distances. Varying the power P_G does have a significant effect on the transported atom number (Figure 4.13c). Not only is the atom number remaining after the initial jerk significantly reduced, but for the lowest Gaussian power ($P_G = 1 \text{ W}$) about 1×10^6 atoms remain in the MOT chamber and are never transported. The inset in Figure 4.13c shows an image of the atom number remaining in the MOT chamber at $P_G = 1 \text{ W}$.

To better understand the initial atom number loss at the start of the transport we perform a comparative measurement between round trip and one-way transport and a static lattice for different transport duration (Figure 4.14a). In case of the static lattice measurement, the atoms were simply held in the lattice for the specified duration before imaging. For the one-way transport measurement, the atoms were transported towards the glass cell but not back to the MOT chamber. Due to the short transport duration, the atoms do not leave the field of view of the MOT imaging system and can still be imaged in the MOT chamber. For the round trip measurements the atoms are transported the same distance

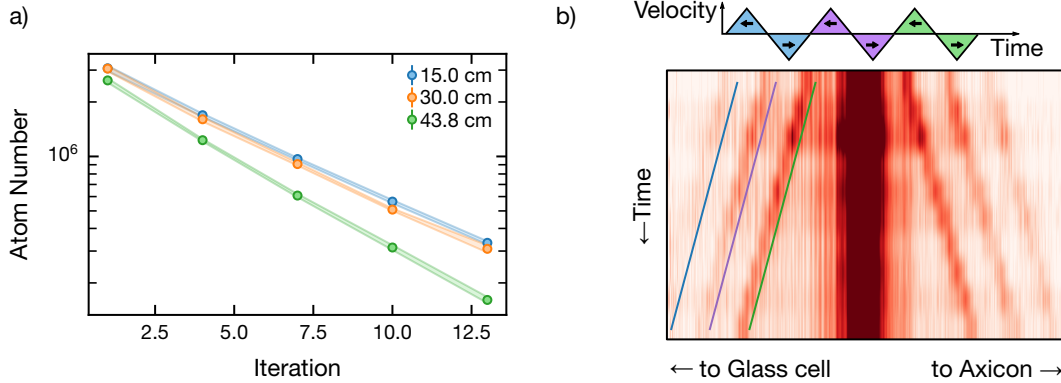


Figure 4.15 | a) Atom number versus number of round trips. The decay appears exponential with increasing number of round trips. $a = 2.9 \text{ km/s}^2$ and $P_G = 6.5 \text{ W}$. b) Very short round trip transport, repeated multiple times. The sketch above the image serves as illustration of the velocity ramps used. Every time the acceleration is inverted, some atoms are not stopped but keep traveling. The straight lines serve as guides to the eye. $a = 2.9 \text{ km/s}^2$ and $P_G = 6.5 \text{ W}$

as for the one-way transport measurement and then back to the center of the MOT chamber. From Figure 4.14a it is clear that the initial loss is not due to holding the atoms in the lattice but related to the start of the transport.

To check if the initial loss is related to the discretization of the frequency ramp we vary the frequency step rate $\delta\tau$ and adjust the frequency step size Δf_{step} to keep the acceleration $a = \lambda\Delta f_{\text{step}}/\delta\tau$ fixed at $a = 2.9 \text{ km/s}^2$. We compute the ratio of the atom number returning from a 5 cm long round trip with the atom number without transport. This ratio does not improve for discretizations finer than the typically chosen one ($\delta\tau = 0.2 \mu\text{s}$, $\Delta f_{\text{step}} = 550 \text{ Hz}$). For step rates above $5 \mu\text{s}$ ($1/\delta\tau = 2\pi \times 32 \text{ kHz}$) we observe a decrease of the atom number ratio with the step rate. For reference, the trap frequency of the lattice is expected to be $\omega \approx 2\pi \times 90 \text{ kHz}$ at the start of the transport (Figure 4.9e). The fact that the atom number ratio is unaffected up to frequency step rates of $\delta\tau = 5 \mu\text{s}$ suggests that the initial loss of atoms at the start of the transport is not due to the discretization of the frequency ramps.

Another option for the initial loss may be the sudden jump in the acceleration. Instead of a smooth increase of the acceleration as for example in Ref [167, 194], we turn on the acceleration instantaneously to a constant value. This type of ramp is easily programmable using the ramp register of the DDS board. More complicated ramps may be possible using the parallel data port. At our clock speeds, this would allow updates of the frequency at a rate of up to 103 MSPS. We have not tested the transport using the parallel data port for communication. Instead we have only used the digital ramp modulation mode of the DDS chip for the measurements presented here due to its ease of use.

Repeating the back and forth transport multiple times shows a roughly exponential decay in the atom number with iteration (Figure 4.15), suggesting that the loss may not be due to temperature, since the hottest atoms should escape during transport leaving a slightly colder sample. Instead, the loss of atoms may be predominantly due to the jerk at the change of acceleration as this jerk remains the same at each step. Furthermore, using multiple very short back and forth transport sequences, we observe that at every time the acceleration is inverted, some of the atoms keep traveling with the prior lattice velocity, i.e. these atoms are not stopped by the deceleration ramp.

4.3.2 One-way transport

In addition to the round trip measurements, we also measure the dependence of the atom number arriving in the glass cell, again as a function of the power P_G and the acceleration a (Figure 4.16). For one-way transport, the second DDS ramp is simply omitted. With $P_G = 6.5 \text{ W}$ and $a = 2.9 \text{ km/s}^2$ around

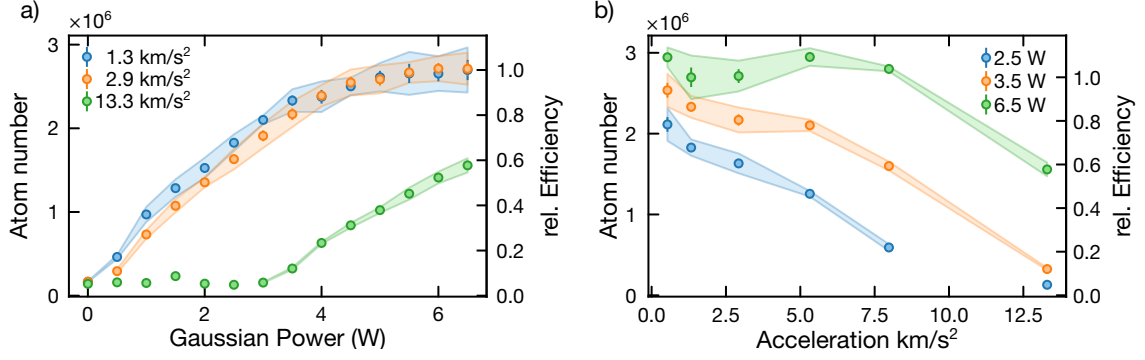


Figure 4.16 | Atom number arriving in the glass cell versus **a)** P_G and **b)** a . Relative efficiency is the atom number scaled to the number of atoms at $a = 2.9 \text{ km/s}^2$ and $P_G = 6.5 \text{ W}$. Markers indicate the mean of 5 measurements, errorbars the standard error of the mean (sem) and the shaded area indicates one standard deviation of the atom numbers, not the relative efficiency. Some of the markers do not show a shaded region because before computing the error, measurements with fitted atom numbers smaller 0 or greater 5×10^6 were discarded, and only a single point remained.

3×10^6 atoms arrive in the glass cell. The one-way transport with this acceleration and a maximum velocity of 26.6 m/s (laser detuning of 50 MHz) is 25.1 ms .

Varying the Gaussian power we find that the transported atom number scales roughly with $\sqrt{P_G}$, suggesting a linear dependence of the transport efficiency with the lattice depth. We find a decreasing efficiency as the acceleration is increased. This too suggests a linear dependence of the transport efficiency on the lattice depth when considering that the acceleration introduces a linear tilt on the lattice potential ($V(x) = V_L \sin(4\pi x/\lambda) - max$). At least for $max \ll V_L$ the effect of the acceleration is mostly a decrease of the lattice depth by $ma\lambda/2$. Additionally, we observe that for low accelerations and high lattice depth the transported atom number saturates. This suggests that neither parameter ultimately limits the transport efficiency. We tried to model the transport using a classical model described in the appendix, [section A](#).

CHAPTER 5

Evaporation to BEC

After transporting the atoms to the glass cell, the atoms are collected in a crossed dipole trap. We subsequently evaporate by tilting the dipole trap and reducing the optical power. This chapter gives details on the evaporation sequence. The evaporation technique was changed after an upgrade to the experimental setup in Spring of 2021. [Section 5.2](#) describes the old evaporation sequence that was developed initially. For future 2D physics experiments the atoms will be loaded into a single plane of a vertical lattice. In [section 5.3](#) I describe the optical setup for the shallow angle vertical lattice. A smaller spacing vertical lattice is currently being installed to increase the confinement along the vertical direction and provide more homogeneous trapping frequencies. This will be described in [\[139\]](#). The chapter closes in [section 5.4](#) by describing the changes to the evaporation sequence after the upgrade in Spring 2021 (see also [\[139\]](#)).

5.1 Production of a Caesium BEC

The first Caesium BEC was produced in 2003 in Innsbruck by Weber et. al [\[174\]](#). Reaching condensation of Caesium atoms had proved difficult before due to large inelastic two-body losses in the magnetically trappable states $|4, 4\rangle$ and $|3, -3\rangle$ [\[137\]](#). Condensation was only achieved when working in the absolute ground state $|3, 3\rangle$. Because the state is not magnetically trappable, optical evaporation has to be used.

While the absolute ground state is protected against inelastic two-body collisions, three-body collisions still play a role. It was found that the three-body loss rate in Caesium is large compared to other alkali atoms ($L_3 > 1 \times 10^{-28} \text{ cm}^6/\text{s}$ [\[99\]](#) compared to $2 \times 10^{-29} \text{ cm}^6/\text{s}$ in ^{87}Rb [\[195\]](#)). This makes evaporation of Caesium more difficult. However, there exists a minimum of the three-body loss rate, due to Efimov physics, which is exploited to improve the ratio of elastic to inelastic collisions [\[103\]](#).

The first successful production of a Caesium BEC first increased the phase space density by loading a smaller diameter dipole trap (dimple) from a larger reservoir dipole trap [\[100, 174\]](#). Thermalization between the atoms in the two traps enabled an increase in the density without increasing the temperature. Condensation was subsequently reached by reducing the laser power and controlling the scattering length to lie close to the minimum of the three-body loss rate at $a \approx 200a_0$ ($B \approx 21 \text{ G}$).

Later, a second evaporation scheme was developed [\[196\]](#), which skipped the dimple loading step. Instead of reducing the trap depth, the trap was tilted by increasing the levitating gradient. Tilting the trap does not alter the trap frequency as much as reducing the laser power. The higher trap frequency allows for faster thermalization during evaporation. The gradient tilt evaporation also proceeds close to the three-body loss rate minimum.

The gradient tilt evaporation proceeds quite fast (pure condensate after 2.5 s starting from the finished loading of the crossed dipole trap), though at comparatively low efficiency ($\eta = 1.9$). Alternatively, the authors of Ref. [\[196\]](#) also present a slower evaporation sequence (6.5 s instead of 2.5 s), which is

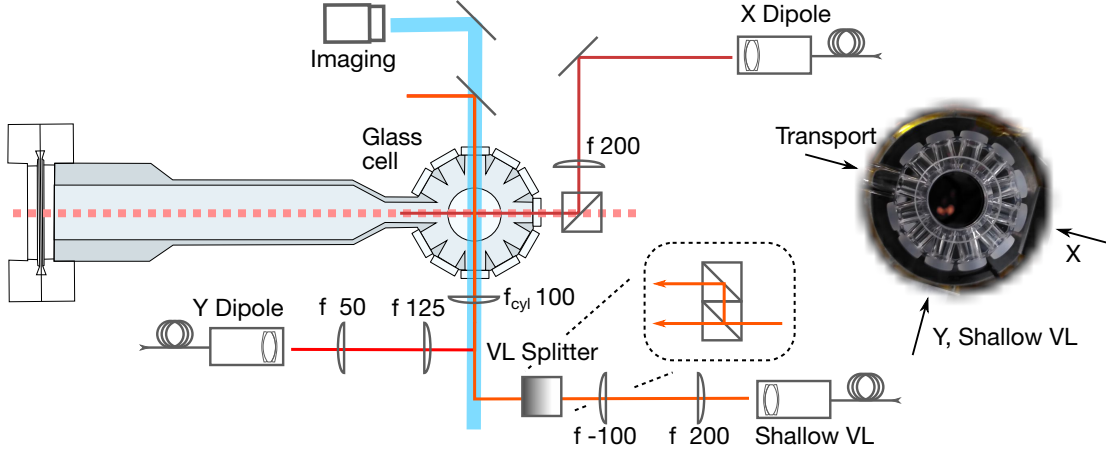


Figure 5.1 | Current setup of the dipole traps around the glass cell. The vertical lattice splitter (VL splitter, see [section 5.3](#)) is shown from above, and from the side in the inset. Y dipole and vertical lattice are overlapped by reflecting the Y dipole trap off a 7 mm \varnothing mirror, and passing the beams of the vertical lattice above and below the mirror.

more efficient ($\eta = 3.6$). The dimple evaporation is quite comparable in speed (6.5 s [151] or 6 s [98] after loading the dimple) and efficiency (≈ 3 [151]).

The initial evaporation sequence implemented in our setup is closer to the one presented in [197] and [198], where both the trap depth and the tilt are varied. This was necessary because we were unable to create sufficiently steep gradients to completely tilt the dipole traps. After an update of the setup in Spring 2021, the evaporation sequence was changed, and currently does not utilize a gradient, neither for levitation during loading from the transport lattice nor for tilting of the trap during evaporation (see [section 5.4](#)). In a sense the scheme is still a hybrid scheme, since the effect of gravity always tilts the trap, and the dimple evaporation scheme cancels the effect of gravity using a levitating gradient.

5.2 Gradient evaporation to BEC

5.2.1 Dipole trap

After transport we collect the atoms in a crossed dipole trap in the glass cell. The dipole trap is formed by an elliptical beam along the y axis ($w_x = 650 \mu\text{m}$, $w_y = 80 \mu\text{m}$ waist) and a circular beam along the x axis ($100 \mu\text{m}$ waist). Both beams use 1064 nm light ([Figure 5.1](#)). The light is taken from the same source as the Gaussian transport beam ([Figure 4.2](#)). To avoid interference between the x and y dipole traps, we have made sure that the beams are frequency shifted w.r.t. each other and have crossed polarization (y is polarized parallel to the bread board, x perpendicular). For both beams we measure the waist at the position of the atoms by reflecting the light out before the vacuum system and measuring the waist where the atoms are expected to be. The y dipole trap is elliptical to match the shape of the atomic cloud after transport (see [Figure 4.12](#)).

The y dipole trap is aligned with an absorption imaging system along the same axis. To overlap the imaging light with the y dipole trap we use a dichroic that reflects 1064 nm light and transmits 852 nm light. Behind the glass cell a dichroic splits the imaging light (852 nm) and the dipole light again. The small leak of the dipole trap light through the dichroic can be used to overlap the dipole trap with the atomic cloud observed in absorption imaging. In normal operation, an additional interference filter before the camera chip removes the 1064 nm leak, allowing only $850 \text{ nm} \pm 10 \text{ nm}$ light to pass¹. The

¹FBH850-10, Thorlabs

Dipole trap	Waists	Power (max)	Depth at 1 W	Trap Freq. at 1 W
x (old)	$100 \times 100 \mu\text{m}$	1 W	$16 \mu\text{K}$	$f_z, f_y = 100 \text{ Hz}$
y (old)	$650 \times 80 \mu\text{m}$	6 W	$3.1 \mu\text{K}$	$f_x = 7 \text{ Hz}, f_z = 56 \text{ Hz}$
x (current)	$100 \times 100 \mu\text{m}$	1 W	$15 \mu\text{K}$	$f_z, f_y = 97 \text{ Hz}$
y (current)	$370 \times 110 \mu\text{m}$	7 W	$3.6 \mu\text{K}$	$f_x = 13 \text{ Hz}, f_z = 42 \text{ Hz}$
Shallow VL	$74 \times 270 \mu\text{m}$	$2 \times 5.5 \text{ W}$	$15 \mu\text{K}$ (lattice)	$f_y = 8.3 \text{ Hz}, f_x = 36 \text{ Hz}, f_z = 2580 \text{ Hz}$

Table 5.1 | Summary of dipole traps around the glass cell. VL = vertical lattice. All dipole traps have a wavelength of 1064 nm. "old" refers to the original evaporation sequence. After an upgrade of the setup around the experimental table the trap waists changed. Notably, the horizontal waist of the y dipole trap was significantly reduced (see section 5.4)

imaging system uses a single achromat ($f = 100 \text{ mm}$, Magnification ≈ 2) to image the atomic cloud on the camera². In principle there should be no chromatic shifts between the dipole trap beam and the imaging light, so overlapping the dipole trap and atomic cloud on the camera should immediately give a signal of atoms trapped in the y dipole trap. We have found that this is not the case, the y dipole is typically slightly below the atomic cloud in the vacuum chamber when overlapped on the camera. Final alignment of the y dipole is done by letting the atoms expand in the Bessel beam by switching off the transport lattice. The expanded cloud is less sensitive to horizontal misalignment so a trapping signal from the y dipole trap can be found by only tuning the vertical alignment.

The x dipole trap is aligned along the transport axis. We do not have an imaging system along that axis, but the x dipole trap can be aligned with the Bessel beam. To overlap the x dipole trap with the transport axis we use a polarizing beam splitter cube just before the glass cell. The Gaussian transport lattice beam is transmitted through the cube, the x dipole trap is reflected. The x dipole trap has to be precisely overlapped with the Bessel beam before the glass cell and before the axicon to get a trapping signal from the atoms.

The transfer of the atoms from the transport lattice into the crossed dipole trap is done in two steps (see also Figure 5.3). In a first step, the Gaussian transport lattice beam is linearly ramped to 0 W in 350 ms while simultaneously ramping up the y dipole trap beam to 5.7 W. After the ramps have finished, we ramp up the x dipole trap to 1 W in 100 ms. Afterwards the atoms are trapped in a trap formed from the y dipole trap, the x dipole trap and the Bessel beam. We then reduce the offset field to 27 G in 200 ms. The end of the offset field ramp defines $t = 0$ in Figure 5.4. As a second step we now remove the Bessel beam by rotating the motorized waveplate. This process takes around 500 ms. We have found that reducing the power of the y dipole trap to 2 W during this time helps to increase the phase space density $\Phi = n_0 \lambda_{dB}^3$. Here $\lambda_{dB} = h/\sqrt{2\pi m k_B T}$ is the thermal de-Broglie wavelength with Planck's constant h , Boltzmann's constant k_B , the temperature T and the peak density n_0 .

After the Bessel has been fully removed, we start evaporation to reach condensation of the atomic cloud into a BEC. At this point we have 0.9×10^6 atoms at $T = 2 \mu\text{K}$. The geometric mean trap frequency is $\bar{\omega} = 2\pi \times 40 \text{ Hz}$. The peak density is $n_0 = N \bar{\omega}^3 (m \lambda_{dB} / h)^3 = 6 \times 10^{11} \text{ cm}^{-3}$ and the phase space density is $\Phi = 3 \times 10^{-3}$.

5.2.2 Gradient Evaporation

The evaporation sequence we followed initially was inspired by the gradient evaporation technique described in [196]. The trap depth is reduced by tilting the optical dipole trap. Tilting the trap is quite easy, as the effect of gravity already produces a tilt of the potential ($V = 1/2 m \omega^2 z^2 - mgz$). For the optical evaporation of Caesium this tilt is compensated by adding a levitation gradient ($\partial_z B = 31.3 \text{ G/cm}$). This means the trap may be tilted by either increasing the gradient (as in [196]) or slowly removing it (cf.

²Manta G-235B, Allied Vision, CMOS chip

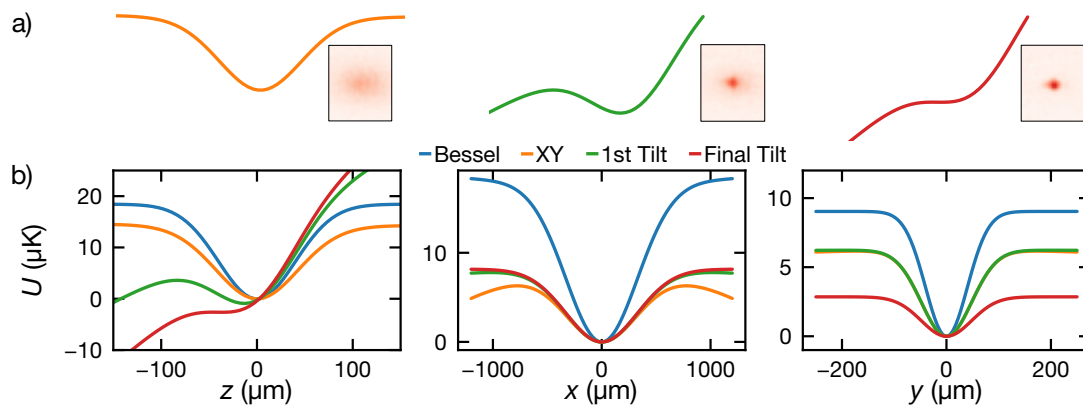


Figure 5.2 | a) Scheme for evaporation. The trap depth is reduced by decreasing the magnetic field gradient that levitates the atoms against gravity. The hottest atoms escape the trap decreasing the temperature of the remaining atoms. The insets show absorption images after 30 ms time of flight. b) Simulated dipole trap potential along x , y and z during the evaporation. Bessel (blue) refers to the configuration just after loading the crossed dipole trap (see Figure 5.3), where the Bessel is still on. XY (orange) refers to the dipole trap after the Bessel has been removed, 1st Tilt (green) is the dipole trap after the first reduction of the gradient, and Final Tilt (red) shows the dipole trap at the point where we observe a BEC.

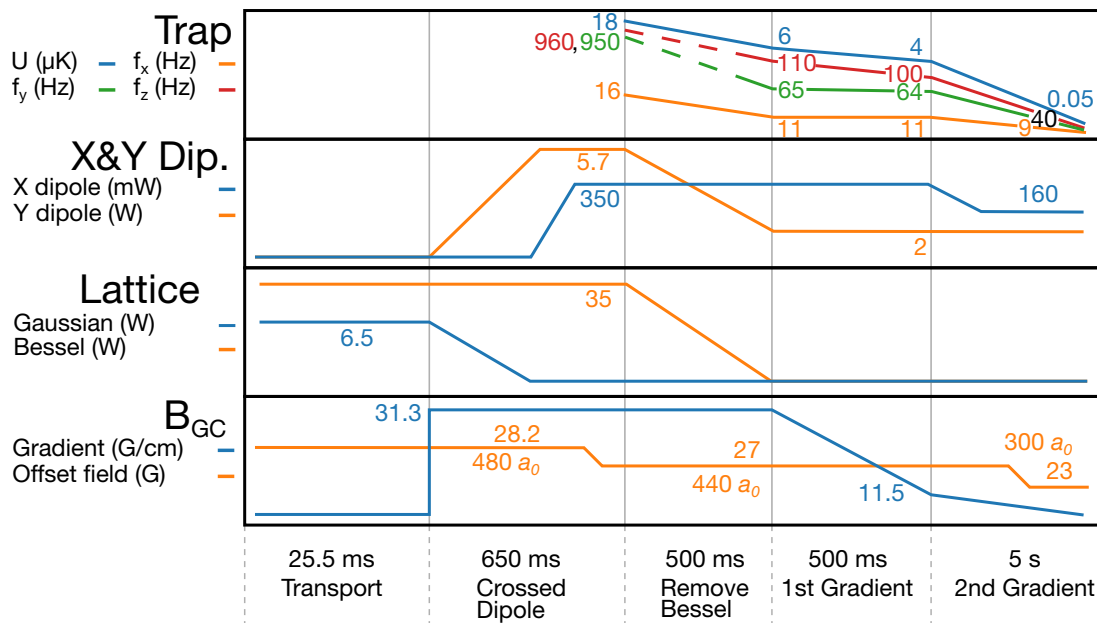


Figure 5.3 | Sequence starting from transport used for evaporation to BEC. The top row shows trap frequencies and minimal trap depths for the dipole traps in the glass cell. Because of the large waist of the y -dipole trap, the x -axis trap frequency remains the lowest trap frequency throughout the evaporation.

Sec. 3.1.6 in Ref. [199]). The benefit of this technique is that the reduction of the trap frequency with reducing trap depth (increasing tilt) is smaller than when simply reducing the optical power (cf. Fig.3 in Ref. [196]). Therefore, faster thermalization is possible and evaporation to degeneracy may be quicker.

In our case we reduce the levitation gradient (Figure 5.2). This is technically simpler as it requires less current than increasing the gradient for the same amount of tilt. Because the crossed dipole trap after having fully removed the levitating gradient (maximum tilt due to gravity) is still too deep to

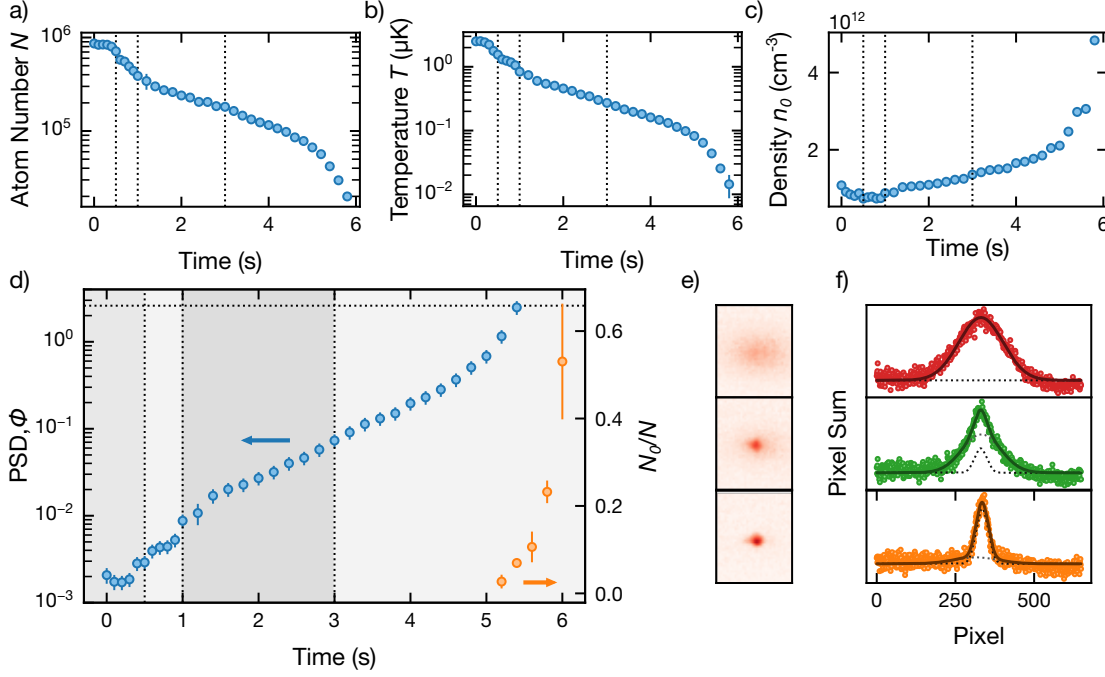


Figure 5.4 | **a)** Atom number N , **b)** temperature T , and **c)** density n_0 during evaporation in the glass cell. The Bessel beam is removed at $t = 0$, the dashed lines at 500 ms, 1 s and 3 s indicate the start of the first gradient ramp, the start of the second gradient ramp and the end of the x dipole trap power ramp respectively. **d)** Evolution of the PSD Φ (left y axis, blue points) and the condensed fraction N_0/N (right axis, orange points) during evaporation. The vertical dashed lines indicate the same times as in a)–c). The horizontal dashed line at $\Phi = 2.6$ is the phase space density at which condensation occurs. The shaded regions show purely optical evaporation (gray), pure gradient evaporation (light gray) and combined optical and gradient evaporation (dark gray). Error bars in a)–d) are one standard deviation of 3 repetitions. **e)** Sample images illustrating the change in the time of flight distribution during condensation. From top to bottom the trap depth is decreased slowly. The images are the mean of 10 repetitions. **f)** Horizontal pixel sums of the images in e). The fitted bimodal distribution is shown in darker shading. Dashed lines indicate the thermal and the condensed fits.

reach condensation, we also reduce the power of the x dipole trap while reducing the gradient. We have found that to reach condensation, the crossed dipole trap has to barely hold against gravity at zero magnetic field gradient.

We reduce the gradient in two linear ramps. First, it is reduced to 11.5 G/cm in 500 ms. This reduces the atom number to around 600 000 atoms, the temperature to 1 μK and increases the phase space density to around 1×10^{-2} . In the second ramp the gradient is reduced to 0 G/cm in 5 s. During the first 2 s of the second ramp we linearly reduce the power of the x dipole trap to 160 mW. We reduce the magnetic bias field to 23 G during the final evaporation stages where the density is highest to reduce three body losses. The lower magnetic field also reduces the scattering length, so the value of 23 G was optimized experimentally for the best ratio of elastic collisions to inelastic ones (three body losses). The evaporation efficiency $\eta = -\ln(\Phi_f/\Phi_i)/\ln(N_f/N_i)$ is $\eta = 1.3$ during the first ramp and $\eta = 2.5$ during the second **Figure 5.5**. Here $\Phi_{i,f}$ and $N_{i,f}$ are the initial (i) and final (f) phase space density and atom number. At the end of the second ramp we find a pure BEC with typically around 2.2×10^4 atoms (**Figure 5.4e–f**).

We measure the temperature and condensed fraction around the onset of condensation to find the critical temperature of the BEC. Temperature and condensed fraction are extracted from absorption images taken after $t_{\text{tof}} = 80$ ms time of flight. For these measurements, the magnetic gradient and offset

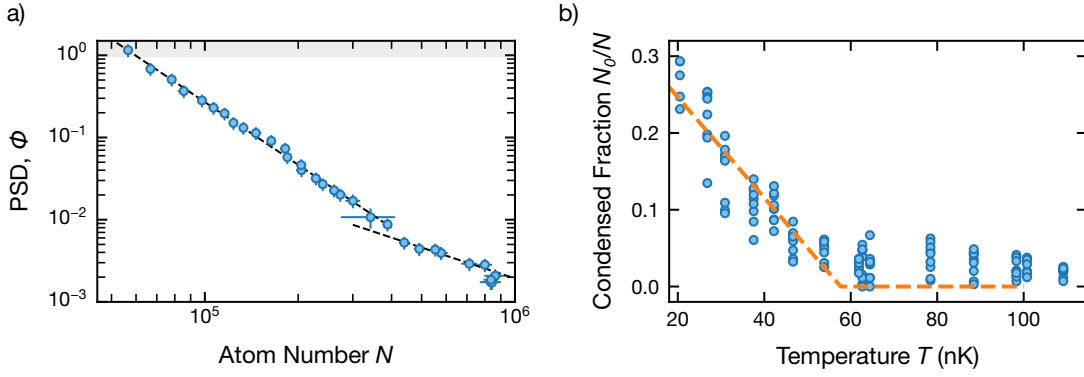


Figure 5.5 | **a)** Evaporation efficiency. The two dashed lines are linear fits to the measured data for the first and second gradient ramps (yielding $\eta = 1.3$ and $\eta = 2.5$). Error bars are one standard deviation. **b)** T_c determination from fitted temperature and condensed fraction. Blue points are measured values, orange curve is a fit to the data.

field are ramped to 30 G/cm and 18 G in the first 3 ms of expansion. 4 ms before taking the image, both are switched off. Expansion at positive scattering length ensures that the BEC does not collapse. The images are fitted with two Gaussian distributions of different sizes. The larger distribution corresponds to the thermal fraction, the smaller distribution to the condensed fraction. The temperature is estimated via $T = \frac{m\sigma^2}{k_B t_{\text{tof}}}$, where σ is the fitted width of the thermal fraction. The initial size is assumed to be negligible after 80 ms time of flight and does not need to be taken into account. The condensed fraction is given by $N_0/N = \frac{N_0}{N_0 + N_{\text{thermal}}}$, with N_0 and N_{thermal} the fitted amplitudes of the two Gaussians and is plotted in Figure 5.4d in orange.

The condensed fraction depends on the temperature as $N_0/N = 1 - (T/T_c)^3$ for $T/T_c < 1$. We fit this formula (Figure 5.5) to the measured ratios and find $T_c \approx 60$ nK. We use our value of T_c to calibrate the atom number in the BEC. The atom number at the critical temperature is $N = (k_B T_c / 0.94 \hbar \bar{\omega})^3$ without taking interactions and the harmonic confinement into account. We take these into account [200–202] and find $N = 130\,000$ atoms. The measured atom number is $N_{\text{exp}} = 54\,000$ atoms using the theoretically expected photon scattering cross section $\sigma_0 = 1.4 \times 10^{-9} \text{ cm}^2$. The ratio of the two atom numbers gives us the actual photon scattering cross section in our imaging system, which is a factor $N/N_{\text{exp}} = 2.3$ smaller. This calibration factor was taken into account for any atom numbers reported in the glass cell so far (also in the previous chapter, imaging axis indicated in Figure 5.1). However, this factor is dependent on the imaging parameters, so not directly transferable to other imaging axes around the vacuum system. For any other imaging axis the reported atom number is computed with an uncalibrated scattering cross section (isotropically polarized light, resonant with $F = 4 \rightarrow F' = 5$, $\sigma_0 = 1.4 \times 10^{-9} \text{ cm}^2$).

Fringes of the y dipole trap After condensing for the first time, we noticed that some times the BEC cloud at short time of flight fragmented. After installation of the high resolution objective for insitu absorption and fluorescence imaging of the BEC (see next chapter for more details on the objective), we found that the cloud reliably splits into stripes at low temperatures. These stripes/fringes were aligned with the y-dipole trap and reminiscent of a lattice. The spacing of the fringes was found to be around 4 – 5 μm . These stripes appear to be related to the y-dipole trap because they disappear once the y-dipole trap is turned off, however we were unable to remove them. We suspect that the cause may be some interference effect between the beam and a second, weak copy of the beam co-propagating at a small angle between the two (6 – 7°). However, changing the tilt of the y-dipole trap through the glass cell viewport, replacing all the optics in the path, simplifying path to only the coupler, a pickup for intensity stabilization and mirror to align the beam through the chamber, or sending the beam

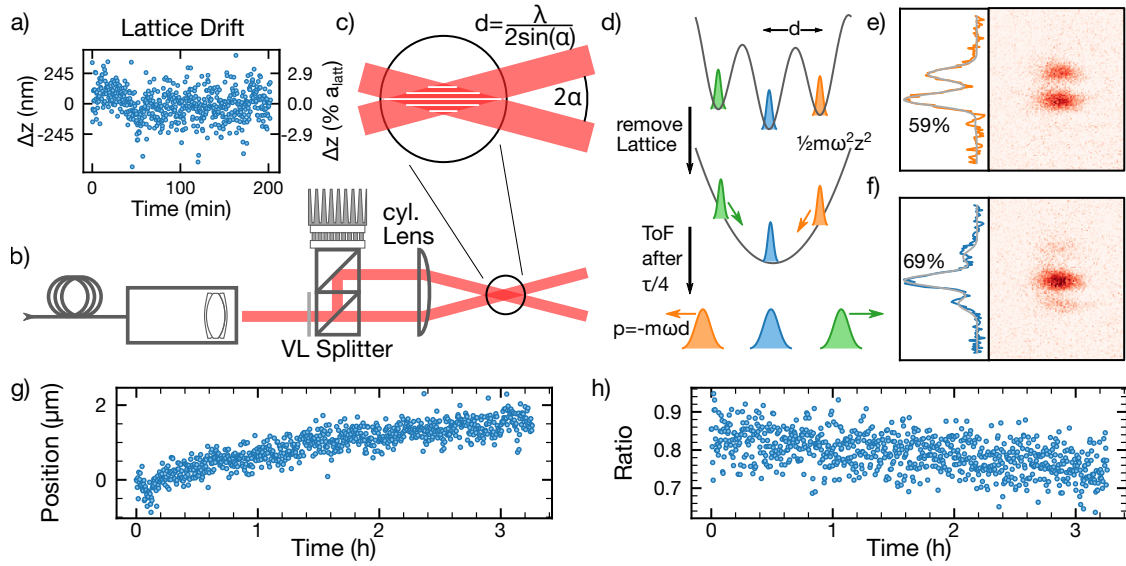


Figure 5.6 | **a)** Stability of the vertical lattice phase measured outside the experiment with temperature stabilization of the vertical lattice splitter. Measured over 3:20 h with a sampling of 2 s. The tick marks are at the mean and 2σ standard deviation of the lattice drifts. Left axis shows drift in nm, right axis in percent of lattice spacing. **b)** Sketch of the shallow angle vertical lattice setup. The beam is split into two parallel beams using a stack of polarizing beam splitters (PBS, VL Splitter). The two beams are focused on the atoms using a $f = 100$ mm cylindrical lens. The two arms interfere at the focus producing a vertical lattice. The VL Splitter can be temperature stabilized using a peltier element. The temperature is measured with a 10 k Ω thermistor (not shown). **c)** Sketch of the lattice produced by the interfering beams. The lattice is at $\lambda = 1064$ nm, so the atoms are trapped in the lattice maxima. **d)** Sketch of matter wave focusing. Atoms trapped on different lattice sites are released from the lattice and move in the potential of a harmonic trap with angular frequency ω . After one quarter period $\tau = 2\pi/\omega$ the atoms are released from the harmonic trap and expand during time of flight. **e),f)** Absorption images and pixel sums for two different alignments of the vertical lattice. In **e)**, the atoms are almost evenly distributed between two sites, in **f)** most of the atoms are in a single site. **g)** Position of the central lattice site and **h)** percentage of atom number in the central lattice site versus time. The position is scaled to the in-situ position of the atoms using the magnification of the matter wave focusing technique. These measurements were taken with a lattice constant of the vertical lattice of 8 μm and a harmonic trap frequency of the focusing potential of 90 Hz.

through the glass cell from the other side did not remove the fringes. Since these fringes will cause issues in future experiments, the plan is to try and work without the y-dipole trap once the atoms are loaded into the shallow angle vertical lattice (see section 5.3). Note that similar fringes were also observed in another Caesium experiment (Ref. [203], Sec. 2.4) and attributed to interference between a dipole trap beam with reflections off the glass cell.

5.3 Shallow angle vertical lattice

For future experiments and fluorescence imaging, the atoms will be loaded into a single plane of a vertical lattice. We produce a vertical lattice by interfering two beams at a shallow angle (half opening angle α), which produces a large lattice spacing, facilitating the loading of a single plane. The interference of the beams will produce a lattice at a spacing of $\lambda/2 \sin(\alpha)$. We use light from a third ALS fiber amplifier capable of producing 30 W of optical power. The lattice light is detuned from the x dipole trap by 80 MHz to avoid interference. To split the light we use two polarizing beamsplitter (PBS) cubes mounted on top of each other (Figure 5.6b, see Ref. [204], p. 73 and Ref. [205] for the original design). By tuning

the polarization before the first PBS the power balance between the two arms of the vertical lattice is controlled. Nylon tipped set screws control the relative pointing of the beams exiting the splitter. A 10 k thermistor connected to the base of the splitter mount and a Peltier element mounted on the top allow stabilization of the temperature³. The two PBS have a side length of 1/2", so the beams are separated by $D = 12.7$ mm. A cylindrical lens with focus length $f = 100$ mm focuses both beams onto the atoms. The beams interfere at an angle of $\alpha = \arctan(D/2f) = 3.6^\circ$ giving a lattice spacing of $d = 8.4 \mu\text{m}$. At the position of the atoms the shallow angle vertical lattice has an elliptical beam profile with waists $w_z = 74 \mu\text{m}$ and $w_x = 270 \mu\text{m}$.

We measured the stability of the vertical lattice planes outside of the experiment by placing a camera at the crossing of the beams⁴. With temperature stabilization of the splitter, we find a variation of the lattice phase of 123 nm (one standard deviation) over 3:20 h (Figure 5.6a). We found that the measured lattice stability also depended on actively stabilizing the temperature of the camera. As this is an artefact of the measurement method, the recorded stability should still be accurate.

The shallow angle vertical lattice enters the glass cell through the same viewport as the y dipole trap. Since the beams of the vertical lattice are displaced w.r.t. the regular beam height, we can overlap the two using a small mirror ($\varnothing = 7$ mm). The y dipole trap is reflected off this mirror whereas the vertical lattice beams pass above and below the mirror. Before aligning the y dipole trap on the atoms, it helps to make the two lattice beams as parallel as possible. For this we place common mirrors for both arms behind the splitter and use them to fold the beam path to a length of a few m. By placing a CCD at different distances from the splitter the parallelity of the beams can be checked and optimized using the set screws pressing against the PBS. After ensuring good parallelism, the vertical lattice may be roughly aligned in the same way as the the y dipole trap, by overlapping the beams with the atomic cloud using the imaging camera along the y axis. The lattice spacing of the vertical lattice is slightly larger than the pixel size, so it is possible to see the lattice on the camera. This allows initial optimization of the relative power and the polarization of the beams to maximize the lattice contrast.

Finer alignment of the vertical lattice is done by maximizing the number of atoms held only by the lattice at very low lattice powers. At this stage, we typically try and move only common mirrors behind the splitter and the cylindrical lens before the chamber to maximize the trapping signal. In the same way, the lattice power balance and polarization can be further optimized. To measure the trap frequency of the lattice we pulse off the y dipole trap. This is sufficient to cause the atoms to start oscillating in their lattice potential wells. At 1 W optical power before the splitter we measure trap frequencies of around 2.6 kHz, in agreement with the expectation from the beam waists and powers (Table 5.1).

The techniques described so far allow alignment of the lattice on the atomic cloud, but not determination of the atomic distribution over the planes of the vertical lattice. We can't observe this distribution directly in absorption imaging because the resolution of the imaging system is insufficient. To still measure the single plane occupation we use matter wave focusing [206–208]. This technique is sketched in Figure 5.6d. Initially the atoms are loaded into the vertical lattice with some distribution over the lattice sites. Due the crossed dipole trap, adjacent lattice sites have slight offsets in energy. Turning off the lattice, the individual wavepackets at each lattice site are free to evolve in the harmonic potential of the crossed dipole trap. Let ω_z be the harmonic trap frequency in the vertical direction, then after holding the atoms in the harmonic trap for a quarter period $t = \tau/4 = 2\pi/4\omega_z$ different initial positions of the atoms are mapped to different momenta [206]. The harmonic confinement is turned off at this time. The atoms are then falling due to gravity, but because of their different initial momenta p_i , atoms originating from different planes of the lattice separate by $\Delta x = t_{\text{TOF}}\Delta p$ with t_{TOF} the time of flight and $\Delta p = -m\omega_z d$ the momentum difference between atoms from different sites spaced by the lattice constant d (and neglecting interactions) [208]. After sufficiently long time of flight, Δx is

³TED200C, Thorlabs

⁴Raspberry Pi Noir Camera v2, Sony CMOS IMX219PQ-Sensor

large enough to be resolved in our imaging system. Figure 5.6e–f show absorption images taken after $t_{\text{TOF}} = 12$ ms and $\omega_z = 2\pi \times 78$ Hz (magnification $M \approx \omega_z t_{\text{TOF}}$). While for Figure 5.6e the atoms are almost equally distributed over two planes of the lattice, in Figure 5.6f about 70% of the atoms are in a single plane. We fit the cloud with three Gaussians of different amplitude and width. The distance between the Gaussians and the position of the central Gaussian are fit parameters, instead of fitting each Gaussian center individually. Note that this same technique is used in Ref. [208] to resolve the occupation of a 3D quantum gas in a 2D lattice.

We measured the stability of the vertical lattice loading using the matter wave focusing technique. The results are displayed in Figure 5.6g and h. We observe a slow drift of the lattice with time, on the order of around $2 \mu\text{m}$ over 3 hours. This results in a slight decrease of the percentage of atoms loaded into the central lattice site, from 80 - 90% to 70 - 80%. The shot-to-shot fluctuations of the lattice position have a standard deviation of around 220 nm or 2.6% of a lattice constant, about a factor of 2 larger than the measurement with the camera (Figure 5.6a).

The expansion of a BEC loaded into the vertical lattice is highly asymmetric. This is because the expansion of a BEC from a trap largely follows the momentum distribution of the ground state of the harmonic trap [209, 210]. As such, a large confinement translates to a faster expansion in time of flight. The trap frequency along the lattice is much larger than the harmonic horizontal trap frequency, leading to asymmetric expansion which is referred to as inversion of ellipticity. We have found that loading our BEC from the crossed dipole trap into the vertical lattice appears to lead to some non-adiabatic heating because for vertical lattice power of a few hundred mW the inversion of ellipticity disappears, suggesting that the atoms do not occupy the ground state of the potential anymore. This may be related to the large increase in density of the BEC as it is loaded into the lattice, and the associated increase in three body losses. To avoid this heating process we have, after an upgrade to the experimental setup around the glass cell, developed a different evaporation sequence, that loads the atoms into the vertical lattice before condensation.

5.4 Upgrade of the setup and new BEC sequence

In April 2021 we mounted the final set of coils around the glass cell and replaced the aluminium breadboards with fiber reinforced plastic ones [139].

With the new setup we initially were unable to reach degeneracy with the old sequence described above. In fact we found that having a magnetic field gradient for levitation decreased the atom number in later stages of the evaporation. We therefore developed a new evaporation sequence. Figure 5.7 presents the new sequence and Table 5.1 gives power and waist of the x and y dipole traps after the upgrade.

The new evaporation sequence is all optical, without tilting the dipole traps using magnetic field gradients. After the atoms have arrived in the glass cell, we simultaneously ramp up the y dipole trap to 7 W and ramp down the Gaussian beam in 350 ms. Afterwards we ramp up the x dipole trap to 1 W in 600 ms. We then remove the Bessel beam in 500 ms by rotating the waveplate. In the next step we jump the magnetic offset field to 26 G ($410 a_0$) and start ramping down the dipole trap depth for forced evaporation. We linearly ramp down the y dipole trap to 2.6 W and exponentially ramp down the x dipole trap to 100 mW in 3.5 s. Simultaneously, we reduce the scattering length in an exponential ramp to $318 a_0$ (23.5 G). The exponential ramps follow $f(t) = \Delta(e^{-t/\tau} - e^{-t_{\text{end}}/\tau})/(1 - e^{-t_{\text{end}}/\tau}) + f_{\text{end}}$, where Δ is the change in the x dipole trap power or the magnetic offset field, τ is the decay time, t_{end} the time where the ramp ends and f_{end} the final value of the dipole trap power or offset field.

2 s after the ramps finished, the vertical lattice power is ramped up to 20 mW with a sinusoidal ramp of 1 s duration. We ramp up the vertical lattice towards the end of the evaporation sequence to reduce the number of atoms loaded into different planes. During the evaporation, the cloud size

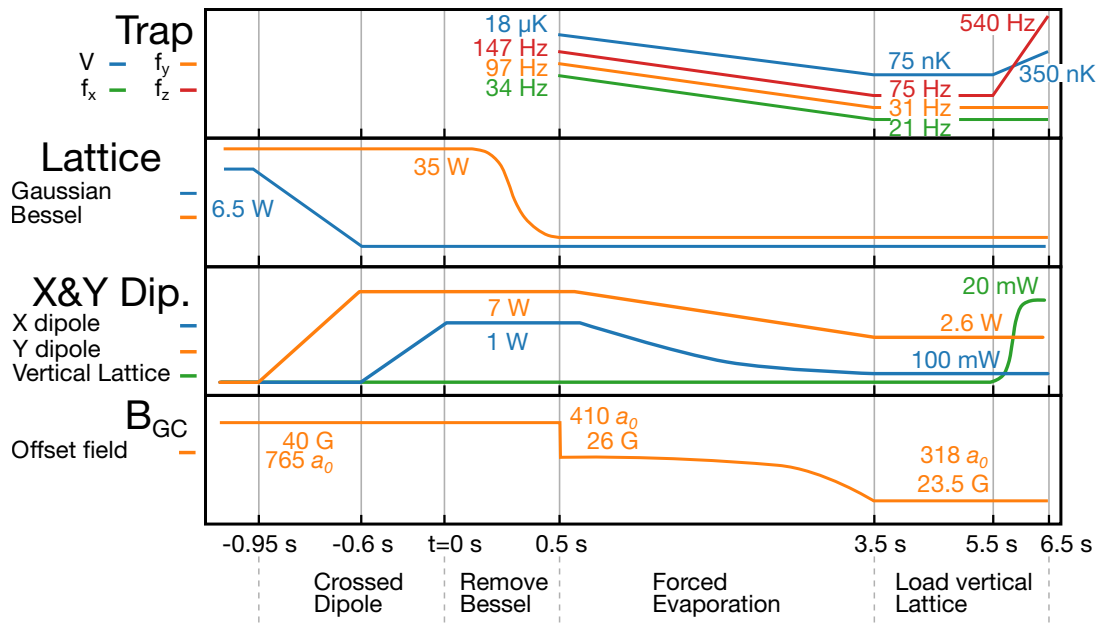


Figure 5.7 | New sequence used to produce a BEC in the combined trap of shallow angle vertical lattice and x and y dipole trap. The choice of $t = 0 \text{ s}$ is identical to the one in Figure 5.4a–d, namely the start of the removal of the Bessel. Trap depth and frequencies are estimated from the measured trap frequencies of the x and y dipole traps and the shallow angle vertical lattice at higher powers.

reduces which makes loading of a single plane easier. The full evaporation after the removal of the Bessel beam takes 6 s. Using this sequence we can produce a BEC of around 20 000 atoms. See [139] for a future description of the sequence.

At the end of the sequence we have a BEC, but we still have some population in other planes of the vertical lattice. We remove the population from other planes by tilting the trap to the side using a magnetic field gradient and an offset field along the horizontal direction. Because the atom number is lower in the other planes, all atoms are lost from those planes while some still remain in the central plane. This evaporation is analogous to the one used in the Rb microscope at the MPQ [211].

CHAPTER 6

Quantum Gas Microscope

After production of our BEC, with the atoms loaded into a single plane of the vertical lattice, we load the atoms into horizontal lattices. By tuning the lattice potential (using e.g. super lattices [212, 213]), the on-site interaction, projecting sharp edges on the lattice (using a DMD [20, 214]) or making the tunneling between sites complex (e.g. in an anti-magic lattice [62–64]), we want to study different many-body lattice Hamiltonians. To read out the quantum many-body state, a quantum gas microscope will be used.

This chapter describes our currently installed horizontal optical lattices as well as the single atom images we have recently been able to capture with our quantum gas microscope. I describe the cooling and imaging setup and the ongoing efforts to achieve single site reconstruction.

6.1 Fluorescence imaging

The working principle of a quantum gas microscope is relatively simple. Fluorescence from atoms trapped in a pinning lattice are captured using an objective and imaged on a CCD. Provided the resolution of the imaging system is comparable to the lattice spacing, the (parity projected) occupation of the pinning lattice can be reconstructed from these images. The imaging resolution is related to the numerical aperture (NA) of the objective and the imaging wavelength λ via $r_A = 0.61\lambda/\text{NA}$, where r_A corresponds to the Rayleigh resolution criterion. Typical lattice spacings on the order of the imaging wavelength imply that a high NA (≈ 0.8) is required. Two approaches to reach high numerical apertures have been implemented in other quantum gas microscopes. First, the atoms may be placed close to a hemispherical lens [11, 13, 14, 66], where the lens is either inside the vacuum or contacted to the glass cell. An out-of-vacuum objective of comparatively low NA (e.g. $\text{NA}=0.5$ [11]) completes the collection optics. Provided the atoms are sufficiently close to the hemisphere (on the order of the imaging wavelength), the NA is increased by a solid immersion effect [215] to $\text{NA}_{\text{SIL}} = n\text{NA}$, with n the refractive index of the hemisphere¹. The alternative is a fully custom objective of high NA and long working distance outside the vacuum chamber [12, 15, 16, 65, 216]. This is the approach we have taken. The objective used is described in more detail in section 6.4.

To produce the fluorescence for the imaging, the atoms need to be excited. The excitation and the subsequent emission of fluorescence leads to recoil heating of the atom. To prevent the atoms from escaping the lattice or tunneling to other lattice sites, deep lattices and cooling is required. The lattice depth typically is on the order of a few hundred μK , dependent on the equilibrium temperature of the cooling. The first quantum gas microscopes used bright optical molasses [11, 12] for cooling. Other microscopes use Raman sideband cooling [13, 65, 66] and EIT cooling [15, 16] (see also [217]) and for ytterbium it was possible to avoid cooling altogether by making the lattice exceptionally deep [14]

¹Alternatively, the refractive index of the hemisphere reduces the wavelength of the imaging light to λ/n

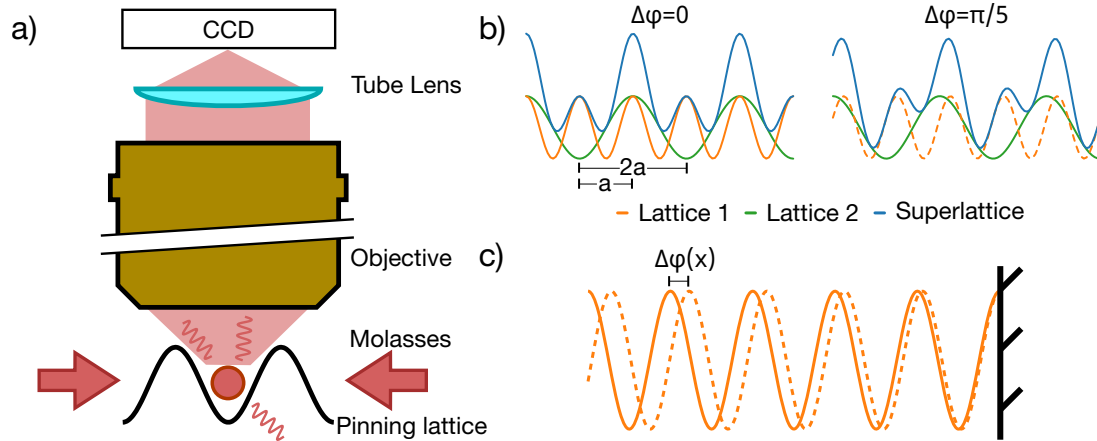


Figure 6.1 | a) For single site resolved imaging, fluorescence photons of atoms trapped in an optical lattice are captured using a high NA objective and imaged on a CCD. To create the fluorescence, the atoms have to be excited. As excitation and emission leads to recoil heating, the atoms need to be cooled during imaging using molasses (as in our case) or other optical cooling techniques. b) Superimposing two optical lattices at lattice spacing a (orange) and $2a$ (red) produces a super lattice potential (blue). Depending on the phase difference between the lattices, the shape of the super lattice potential changes (left and right plots). c) Slight variations in the wavelength of two lattices leads to an effective phase difference at the position of the atoms and allows tuning of the relative phase between the two optical lattices forming the super lattice.

(68 mK). Here we opted for molasses cooling due to its simplicity and the relatively low temperatures achievable in Caesium (see [section 6.3](#)).

Quantum gas microscopes have already been implemented for Rubidium [11, 12], Ytterbium [14, 216], fermionic Potassium [13, 15, 16] and fermionic [13, 15, 16, 65, 66] and bosonic [218] Lithium. Similarly, for Caesium, single site resolved imaging of atoms has been shown in Refs. [93, 123, 219, 220]. The cited Caesium experiments load their lattices directly from a MOT. In contrast, we will work with degenerate atomic samples, which will allow us to study the low-temperature or ground-state properties of many-body phases.

6.2 Lattices

Our glass cell is twelve-sided and as such offers 3 pairs of perpendicular axes for dipole traps and optical lattices. One pair is being used for the transport lattice and the optical dipole traps used during evaporation, as well as for the shallow angle vertical lattice. We plan to use the other two pairs for two different sets of 2d horizontal lattices. One pair is planned to be used for a 2d super lattice potential ([Figure 6.1b](#)) made from 767 nm and 1534 nm laser light, the other is intended for the anti-magic lattice along one axis and a super lattice along the other. Currently we are only working with a 767 nm lattice along the future double super lattice viewport pair (see [Figure 6.2a](#)). This is in some sense the simplest configuration to start with, as the 767 nm lattice can be used for loading the atoms into the lattice and for pinning them during fluorescence imaging. It suffers from the drawback of a shorter lattice spacing compared to the 1534 nm lattice, which makes reconstruction of the lattice occupation more difficult (see [section 6.6](#)). However, we do not have sufficient power at 1534 nm to pin the atoms to their lattice site during imaging. We would require both the 1534 nm and the 767 nm lattice to make use of the larger spacing of the 1534 nm lattice in imaging and reconstruction. In this case the atoms would be loaded in the 1534 nm lattice initially and for imaging the 767 nm lattices would be ramped up. The 767 nm

lattice would split the larger 2D 1534 nm unit cell into four sites. Phase control between the 767 nm lattice and the 1534 nm lattice would be required to deterministically load a specific site of the smaller spaced lattice. In this experiment, this phase control will be achieved by variation of the frequency difference between the 1534 nm and the 767 nm laser light. Small changes in the frequency lead to a phase shift of $\Delta\phi = 2\pi L\Delta f/c$, where L is the distance from the atoms to the retro mirror (Figure 6.1c). $L \approx 200$ mm in our setup, so $\Delta f = 1.5$ GHz for a 2π phase shift. The control of the frequency difference between the two lattices necessitates a frequency lock scheme. We have frequency doubled our 1534 nm light, but so far have not locked it to the Ti:Sa producing the 767 nm light. We have decided to proceed with the 767 nm lattice setup instead of waiting for the lock setup to be finished.

The light for the lattices is produced by two separate Ti:Sa ring lasers² each capable of up to 8 W output power at 780 nm. The Ti:Sa are set to run at 767 nm to allow for future installation of a super lattice, where the long wavelength lattice is produced by a 1534 nm fiber amplifier³. Apart from physics experiments, the 767 nm lattices are also used to pin the atoms during fluorescence imaging. From previous experience in the single-site Rb experiment of our group [211], we chose the waists for the 767 nm lattice such that at 3.5 W power on the atoms, the trap depth is around 200 μ K. This trap depth should be much larger than the temperature of the atoms to avoid thermal hopping. Thermal hopping may be modeled using Arrhenius' law $\Gamma_h = \Gamma_a \text{erfc}[\sqrt{V_{\text{latt}}/k_B T}]$ [211, 220], where Γ_a can be interpreted as the rate at which hopping is attempted. Ref. [220] reports $\Gamma_a = 265 \text{ s}^{-1}$ with Caesium in a lattice of 4.9 μ m spacing, ref. [211] reports $\Gamma_a \approx 20\sqrt{\pi} \text{ s}^{-1}$ with Rubidium in a lattice of 680 nm. Assuming that we can reach comparable temperatures to Ref. [220] ($T = 10 \mu$ K), we can expect $\Gamma_h (\approx 7 \times 10^{-8} \text{ s}^{-1})$ to be negligible for a lattice depth of 200 μ K.

We have chosen to use elliptical waist beams to minimize the horizontal trap frequency perpendicular to the lattice direction. As we plan to do experiments in 2D systems, the vertical trap frequency can in principle be almost arbitrary. In practice, very small waist lead to higher sensitivity to the alignment of the lattices. The compromise we have chosen are waists of $w_z = 45 \mu$ m and $w_h = 303 \mu$ m. The optics used consist of the $f = 20$ mm collimator lens⁴, a cylindrical $f = 400$ mm lens, a $f = 150$ mm singlet lens⁵ and a cat eye reflector⁶ on the other side of the glass cell (Figure 6.2a). The cylindrical lens forms a telescope with the singlet lens to reduce the horizontal beam diameter, the beam's vertical direction is simply focused on the atoms. This lattice is around 210 μ K ($2900 E_R$) deep at 3.5 W input power. At 25 mW, the lattice frequency is $\omega_{\text{latt}} = 2\pi \times 18$ kHz, the depth is $13 E_R$ and the tunneling rate is $J = 2\pi \times 25$ Hz. From these considerations, it becomes clear that stabilizing the lattice intensity during the experiment ($P_{\text{latt}} \approx 25$ mW) and the imaging ($P_{\text{latt}} \approx 3.5$ W) is tricky since either the photodiode recording the intensity is saturated or the signal is barely above the noise level of the photodiode. The power stabilization is less critical at pinning powers as the power fluctuations will typically be much slower than the trap frequencies. Therefore, we only actively stabilize the lattices at low powers during the experiments and simply set the RF power sent to the stabilizing AOM to maximum during pinning.

In the experiment, we do not reach 3.5 W but rather 3 W. This is due to low fiber coupling efficiency from the Ti:Sa output and an additional isolator placed at the fiber output on the experiment table. In addition, the waist at the position of the atoms appears to be slightly larger. From parametric heating measurement we deduce a lattice depth which is 60% of the expected depth (120 μ K).

We use a sinusoidal ramp of 200 ms duration to 80 mW to load the horizontal lattices. For fluorescence imaging, we then jump the lattice power to the maximum value.

²Matisse CS, Sirah

³Koheras, NKT; Rio, Orion; Nufern

⁴60FC-SMA-T-23-M20-10, Schäfter+Kirchhoff

⁵#47380, Edmund Optics

⁶lens: f150, #47380, Edmund Optics along Y", f100, #45806, Edmund Optics along X"

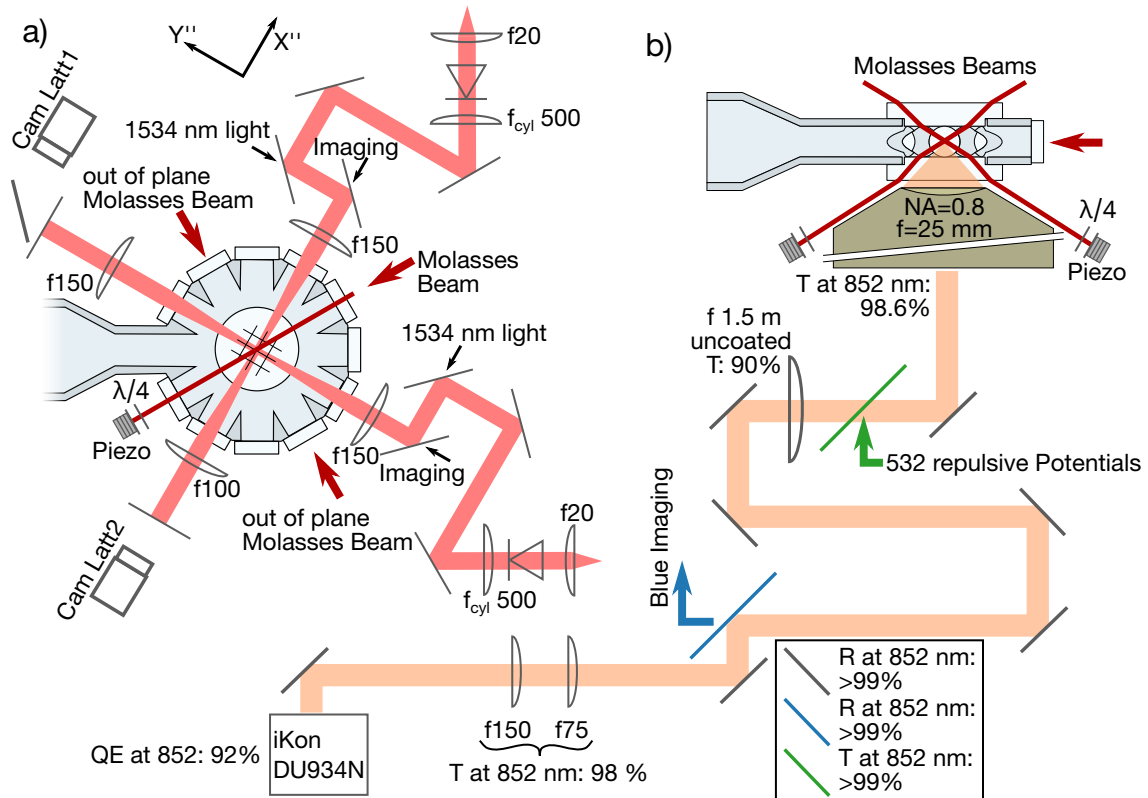


Figure 6.2 | a) Orientation of the lattice beams for the 767 nm lattice and the molasses beams used for cooling the atoms in the pinning lattice. In addition, the beam shaping lenses for the lattices and the dichroics to overlap imaging light and 1534 nm light with the lattice axes are shown. Each lattice axis has its own imaging camera used for rough alignment of the lattice beam on the atoms. The lenses in front of the lattice retro mirrors are different because of space constraints. b) Orientation of the out-of-plane molasses beams and beam path used for the imaging setup. The $f = 150$ mm and $f = 75$ mm lens are matched achromats. Distances not to scale. A dichroic mirror allows us to overlap blue detuned light with the imaging axis to project additional potentials through the objective. Another dichroic mirror behind the $f = 0.5$ m tube lens transmits 456 nm light and reflects 852 nm. The reflectivity and transmission of the imaging optics are listed for 852 nm. In total, we expect to catch around 15% of the emitted fluorescence photons, taking the solid angle of the objective into account (20% of emitted photons are captured by the objective).

6.3 Molasses

During fluorescence imaging we use an optical molasses on the D2 line to cool the atoms and generate the fluorescence photons. We opted to use molasses cooling instead of Raman sideband cooling as the experimental setup for molasses cooling is simpler, and in Caesium the temperatures that can be reached with free-space bright molasses on the D2 line are quite low (<10 μ K). We split off some of the light used in the MOT and fiber couple it. Using fiber splitters⁷, we split the light into three arms. We have one molasses axis in the horizontal plane. The other two are entering the glass cell at a 30° angle with the horizontal plane, passing between the coils and the objective (Figure 6.2a,b). All beams are circularly polarized before entering the chamber and retro reflected with a $\lambda/4$ waveplate mounted before the retro mirror. The retro mirrors are mounted on ring piezos⁸. These will be driven at low frequency to wash out the interference between the molasses beams, as is done in Ref. [211]. In Ref. [211] a

⁷PN850R3A1 (75:25 Split) and PN850R5A1 (50:50 Split), Thorlabs

⁸PI, Drivers: PDU150CL, PiezoDrive

modulation of the fluorescence intensity from the atoms in the lattice is observed, and attributed to the interference between the molasses beams. By modulating the retro mirrors this interference could be removed. Alternatively, the different molasses beams can be frequency offset from each other [11], though this is not an option in our setup because we are using fiber splitters.

Using fiber splitters also implies that we are unable to control the beam balance between the fiber outputs. We control the balance between the molasses axes by tuning the transmission through the cleaning cube at the fiber exit. Since very little power is required for the molasses, this is not a big constrain on the power needed on the optical table before the molasses fibers.

The vertical molasses beams are tightly constrained by the coil mount and the objective. Alignment of the beams through the coil mount to the other side is sufficient for an initial alignment, as the beams are relatively large (2 mm diameter). Alignment of the retro mirror is possible by coupling the retro light back into the fiber. For the initial alignment of the polarization for the vertical beams we minimize the reflection of the retro reflected beam off the cleaning cube. This ensures circular polarization, though the helicity is not determined. Aligning the horizontal beams is simpler in some sense, as it can be centered on the entry and exit viewport of the glass cell, and a tool to measure the polarization can be easily placed into the beam path.

6.4 Objective

To image the atoms, we use a high NA (NA = 0.8, solid angle $\Omega = 4\pi \times 0.2$) objective specially designed for our experiment⁹. The objective was designed to be diffraction limited at the imaging wavelengths 456 nm and 852 nm as well as 780 nm (imaging wavelength of ⁸⁷Rb) and 532 nm (for repulsive potentials projected through the objective). The objective has a focal length of 25 mm and a backward working distance from the top of the glass cell of 2.34 mm. The objective is mounted in a custom designed [139] 5 axis mount, which uses picomotors¹⁰ to control the tip, tilt, and x , y and z position of the objective. An additional set of closed loop piezos¹¹ allows fast, reproducible changes of the z position of the objective for refocusing. There are 9 lenses inside the objective, each with a broadband AR coating of $R < 0.15\%$ per surface. The expected transmission for 852 nm light is 98.6%, for 456 nm it is 97.6%.

Before installation of the objective, both the mount and the objective were tested (Figure 6.3a). To test the objective, we used a star target [glockner]. The star target is a glass plate with a thin reflective chrome coating on one side. Small holes with diameters of a few hundred nm have been pierced into the coating. By illuminating the star target from one side and imaging with the objective from the other, the point spread function (PSF) of the objective can be measured (provided $\varnothing_{\text{hole}} < \lambda_{\text{imag}}$) (Figure 6.3b). In addition to allowing tests of the objective, it also allows us to test alignment strategies. For initial alignment, we first align a reference beam perpendicular to the viewport by overlapping the incoming beam with its reflection. Part of the reference beam is reflected off each lens of the objective. We overlap those reflections with the incoming beam for rough alignment of the objective. Finer alignment is done with the camera and the emission from the star target holes by minimizing the size and distortion of the PSF. To measure the magnification we used a USAF target¹². Figure 6.3c and d show sample PSFs measured in the test setup with 852 nm and 456 nm light respectively. We find an average PSF of $r_A = 780$ nm at $\lambda = 852$ nm (Figure 6.3d) and $r_A = 430$ nm at $\lambda = 456$ nm by evaluating multiple PSFs from a single image. This size is slightly larger than what was expected theoretically.

⁹54-41-25@456-852nm, Special optics

¹⁰Picomotor 8301, Newport

¹¹P885.90 with strain gauge, PI

¹²Highres-1, Newport

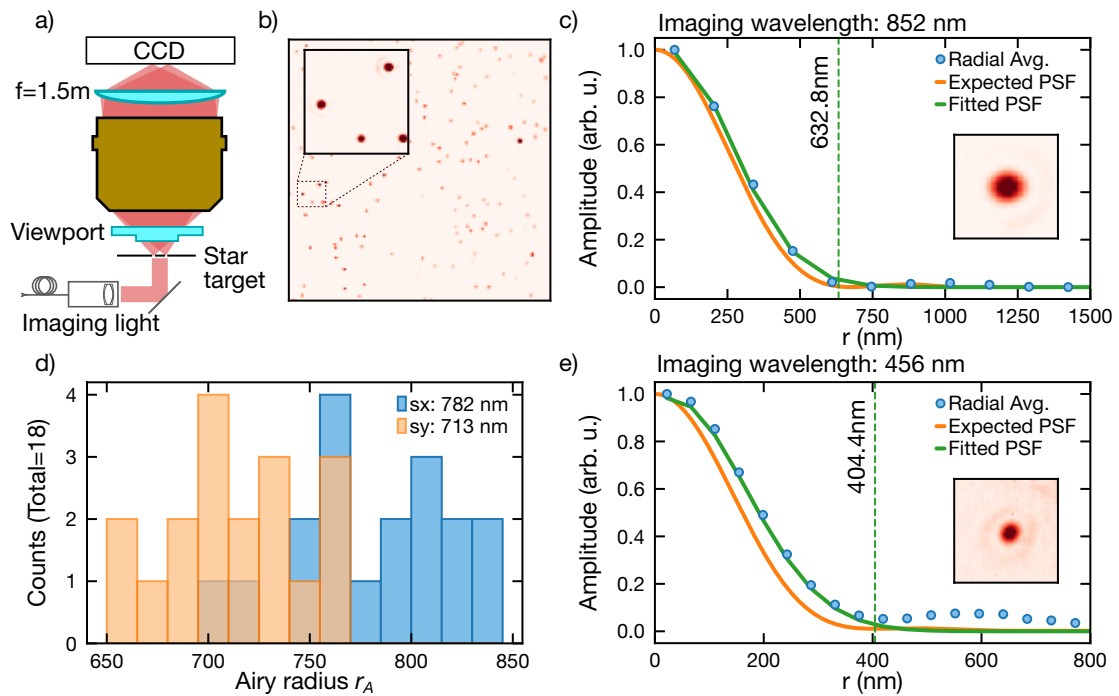


Figure 6.3 | **a)** Sketch of the test setup. The Star target is a chrome coated glass plate with tiny holes etched into it. The viewport is a replica of the glass cell viewports, but without the nano glass plate coating. **b)** Images taken of the star target with the camera. Each point is a hole in the PSF. The inset shows an enlarged view of an area around the middle left edge. **c)** Radially averaged PSF (blue points) of one of the stars, with 852 nm illumination. The orange curve is the expectation, taking the finite size of the star target holes into account (≈ 100 nm). The green curve is a Gaussian fit to the measured PSF. The dashed line indicates the resolution according to the Rayleigh criterion. This is a particularly small PSF, the average size is larger. The inset shows the image of the PSF. **d)** Fitted resolution to 18 PSFs from **b)**. The images are fit using a 2D Gaussian. The mean resolution in the x and y direction is 782 nm and 713 nm respectively. **e)** Radially averaged PSF of a single star similar to **b)** but using 456 nm light ($6S \rightarrow 7P$ transition of Caesium) for imaging.

Initial objective alignment on the atoms

- Before installing the objective, we made sure that the top and bottom viewports of the glass cell are perpendicular to the direction of gravity. This was done by placing a water basin underneath the glass cell and sending a laser beam from the top through the glass cell into the basin (Figure 6.4 ①). This laser is aligned perpendicular to the viewports of the glass cell and the optical table is subsequently tilted to make the laser beam perpendicular to the water surface. Note that we observe two reflections from the glass cell viewports, spaced by around 2 mm 99 cm from the glass cell. The two reflections are most likely from the top and bottom viewport, suggesting a tilt between the two of 2 mrad.
- The same laser beam is then aligned to hit the atoms while still being perpendicular to the glass cell viewports (Figure 6.4 ②). We use resonant light to kill the atomic cloud just after transport to the glass cell. This reference beam is then used to roughly align the objective, the tube lens and the mirrors in the imaging path. For this we use the same strategy as in the test setup.
- We move and tilt the objective such that the reflections of the reference beam from the lenses inside the objective are rotationally symmetric around the incoming reference beam. The reflections are viewed on a screen with a hole for the reference beam (Figure 6.4 ③).

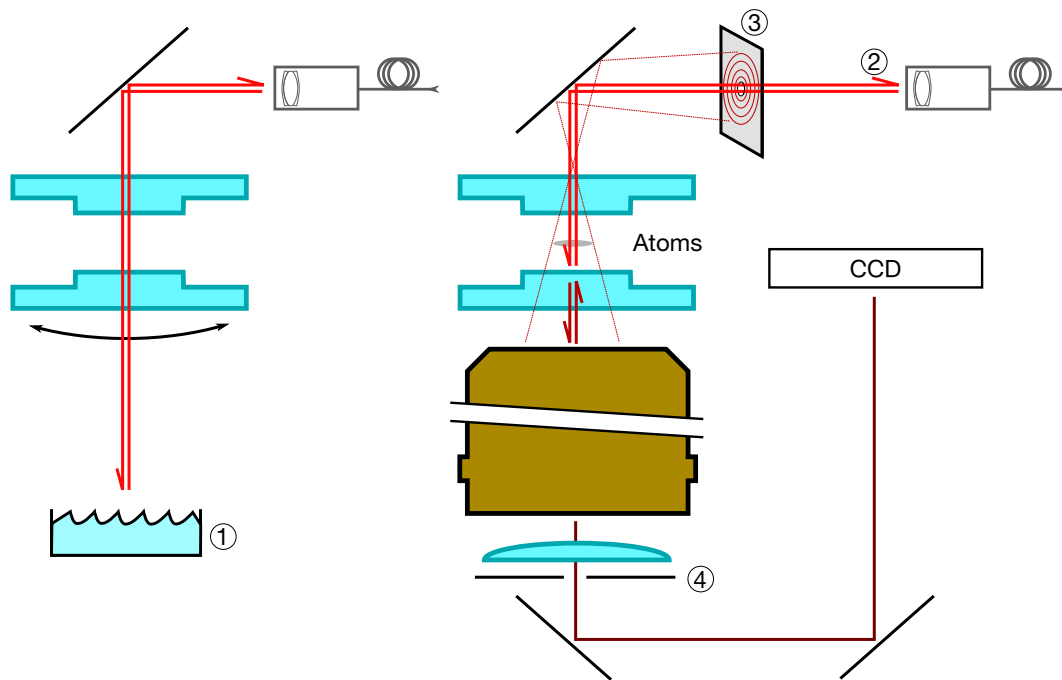


Figure 6.4 | ① Aligning the glass cell viewports perpendicular to the direction of gravity using a water basin. The glass cell is tilted by tilting the optical table. Right: Alignment of the objective. ② The reference beam is aligned perpendicular to the bottom viewport of the glass cell while also hitting the atoms. ③ The objective is moved such that the reflections from the objective are symmetric w.r.t. the incoming reference beam as viewed on a screen above the glass cell. ④ The imaging lens and the folding mirrors are centered on the reference beam using an iris right behind the imaging lens.

- The next step is to roughly align the imaging system. For this step, it helps to temporarily work at a lower magnification to have a larger field of view. We worked with a magnification of 20 (focal length of the tube lens $f = 500$ mm). We roughly align the tube lens and the imaging mirrors such that the reference beam hits the imaging CCD. Since the reference beam is overlapped with the atoms in the imaging plane, the atoms should then also be visible on the CCD. We take fluorescence images and move the mirrors before the camera to see the atoms on the CCD.
- With the imaging system roughly aligned, we place an iris between objective and tube lens (Figure 6.4 ④). We place the iris such that when closing it the reference beam is at the same position on the CCD camera as the atoms. In this way, we can use the reference beam in the next steps to center the image of the atoms on the tube lens and the imaging mirrors.
- After placing the iris, the tube lens can be exchanged for the one needed for the desired magnification (in our case $f = 1.5$ m yielding a magnification of 60). We center the tube and the mirrors behind the tube lens on the reference beam that is passing through the iris. We also optimize the tilt of the tube lens, by overlapping the back reflection off the lens with the incoming beam. This procedure results in a decent alignment of the imaging system. For further improvements, we image single atoms and move the objective to minimize the size of the point spread function.

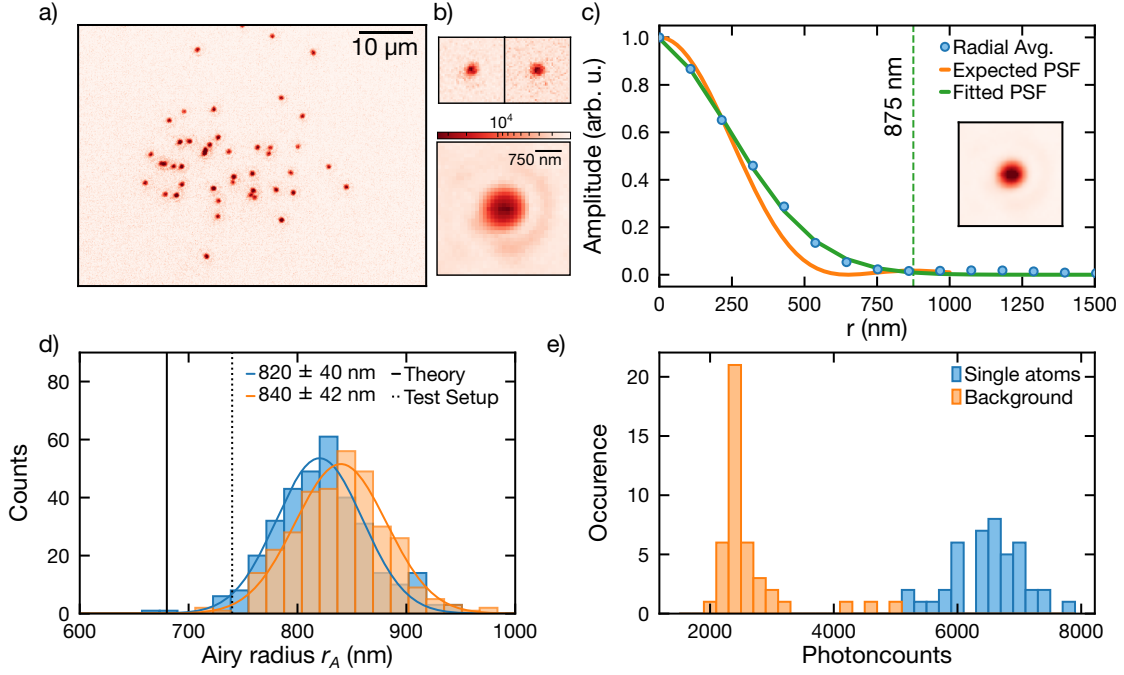


Figure 6.5 | **a)** Image of a dilute cloud with single atoms trapped in the pinning lattice. **b)** Sample crops around single atoms from **a** and the upsampled and averaged image of the point spread function. Logarithmic scale. **c)** Radial average and Gaussian fit to the averaged point spread function shown in **c**. The inset shows the averaged PSF with a linear color scale. **d)** Histogram of fitted PSF sizes along x and y . The error bars specify the standard deviation of a Gaussian fit to the distribution. The solid black line is the expectation from a diffraction limited imaging system, the dotted line is the result from the test setup. Imaging wavelength is 852 nm. **e)** Photon count histogram of regions with (blue) and without (orange) single atoms. For computing the histograms, an area of the image was cropped to a 9×9 region and the pixel counts summed up. This corresponds to an area of about $910 \text{ nm} \times 910 \text{ nm}$ in the atomic plane ($M \approx 128$). The exposure time was 1 s. For the background crops, we randomly picked locations in the image that were more than 8 pixel (810 nm) from any single atom.

6.5 Imaging

After loading the atoms into the horizontal and vertical lattices and ramping up the lattice powers for pinning ($P_{x,y} \approx 3 \text{ W}$, $P_z \approx 11 \text{ W}$), the molasses beams (cooling on $F = 4 \rightarrow F' = 5$) and a repumper (pumping atoms from $|F = 3\rangle$ to $|F' = 4\rangle$), aligned with the transport axis) are turned on. In addition, we change the magnetic field to fully compensate the previously measured background magnetic field. We initially tried to observe the fluorescence from the side, as here, due to the smaller magnification and the fact that the imaging system was already aligned, we were expecting to have an easier time to see some signal. Indeed we did observe a signal more or less out of the box. Surprisingly, we found that the atomic cloud in the fluorescence image was aberrated much more strongly compared to the absorption image on the same camera. Trying to correct for those aberrations by changing the position of the camera made the absorption image aberrations worse.

Having seen a signal on the camera from the side, we then aligned the imaging system through the objective, with an initial magnification of 60. Here too we quickly got a first fluorescence signal on the camera¹³. Because of the large pixel size of the camera ($13 \mu\text{m}$), the PSF only extended over a few pixels in diameter. We chose to increase the magnification to better resolve the PSF by installing two

¹³CCD camera, iKon DU934N-BR-DD, Andor

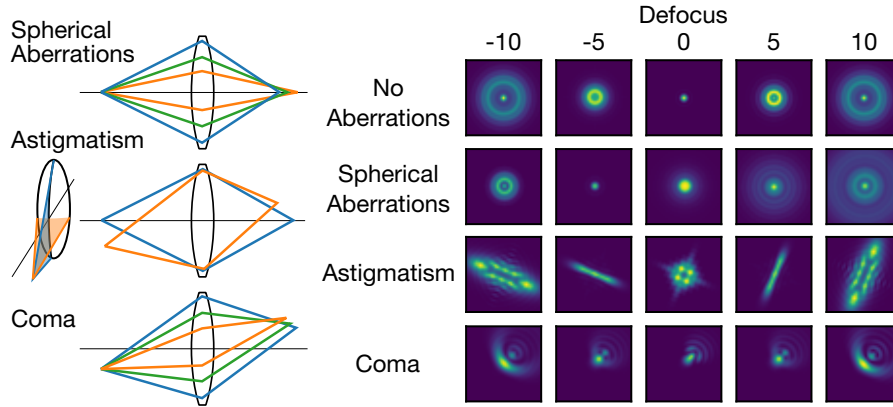


Figure 6.6 | Effect of different Seidel aberrations on the PSF. From left to right, the defocus is varied. Both astigmatism and coma lead to asymmetric PSFs, whereas the the PSF remains rotationally symmetric (for a given defocus) for spherical aberrations. The PSF was computed as $\text{PSF} = |FT\{P\}|^2$ via the pupil function $P = S_0\rho^4 + \alpha\rho^2 \cos(2\theta - 2\varphi) + \beta\rho^2 + \gamma\rho^3 \cos(\theta - \varphi)$, where $S_0, \alpha, \beta, \gamma$ specify the magnitude of spherical aberrations, astigmatism, defocus and coma respectively, and φ the tilt of the optical system. The left side sketches the origin of the different aberrations.

achromats¹⁴, magnifying the image by a factor of 2 (Figure 6.5a). With this new magnification, and by optimizing the position and tilt of the objective and ensuring that a beam entering the center of the $f = 1.5$ m imaging lens is centered on all subsequent mirrors, we managed to reach a Airy radius of $r_A = 830$ nm of the point spread function of a single atom (Figure 6.5d,e). Note that in order to avoid aberrations from stress on the mirrors, all mirrors have been glued into their mounts. The measured PSF is larger than what is expected from using the NA of the objective ($r_A = 0.61\lambda/\text{NA} \approx 650$ nm) or what was measured in a test setup ($r_A = 780$ nm for $\lambda = 852$ nm). The PSF was measured by taking multiple images similar to Figure 6.5a. Isolated atoms in each image were found¹⁵ (see Figure 6.5b) and fitted with a 2D Gaussian. The $1/e$ size of the Gaussian r_G was then converted into an Airy radius $r_A = 2.865r_G$. The factor 2.865 was found numerically by fitting a Gaussian to an Airy disk. To produce the averaged image of the PSF (Figure 6.5c), the isolated atom images were upsampled and overlapped using the fitted centers of the PSFs.

It is not clear at this point what is limiting the size of the PSF. The PSF size may increase due to aberrations, or an aperture in the imaging beam path reducing the effective NA. The dominant aberrations that distort the PSF are spherical aberrations, coma and astigmatism, shown in Figure 6.6 at different positions along the focus. They are part of the Seidel aberrations and arise due to corrections to the linear approximation of Snell's law used in paraxial optics ($\sin(x) = x - x^3/6 + \mathcal{O}(x^6)$) [221]. Coma and astigmatism are relevant for objects that do not lie on the optical axis of the imaging system and lead to asymmetric deformations of the PSF. Spherical aberrations are due to stronger refractions of beams off the optical axis. The images shown in Figure 6.6 were simulated using the effect of the aberrations on the wavefront in the entry pupil P (Ref. [221], p. 206, Table 7.2) and the relation between the entry pupil and the PSF: $\text{PSF} = |FT\{P\}|^2$ (Ref. [222], Fig. 2).

The measured PSF is fairly rotationally symmetric (Figure 6.5c), making coma or astigmatism unlikely. When scanning the focus, the size of the PSF increases asymmetrically, as would be expected for spherical aberrations. However, it seems unlikely that the 1.5 m singlet lens causes any spherical aberrations. The spot diameter due to third order spherical aberrations of a singlet lens may be estimated using $d_{\text{sph}} = 0.067f/(f/\#)^3$ ([223], p.13), where $f/\# = f/D$ is the f-number of the singlet lens. For the 2", $f = 1.5$ m lens, this yields $d_{\text{sph}} \approx 4$ μm , much smaller than the magnified ($\times 60$) PSF of an

¹⁴f75 and f150, MAP1075150, Thorlabs

¹⁵`skimage.feature.peak_local_max` of the `skimage` python package

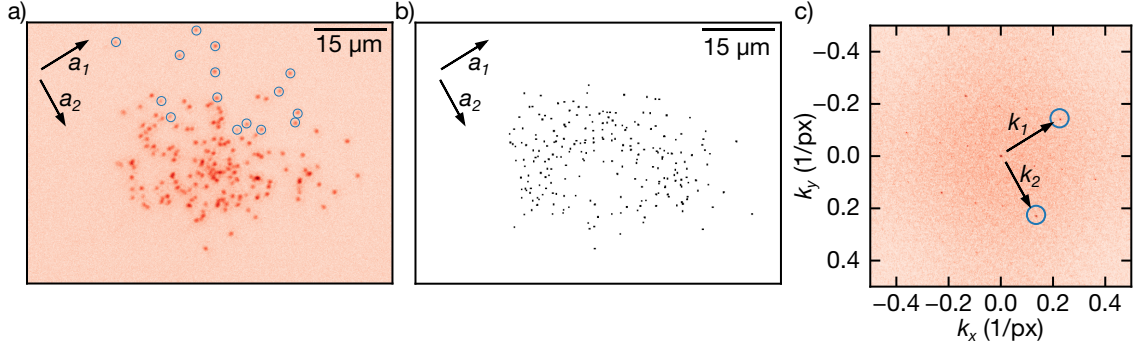


Figure 6.7 | **a)** Example of a fluorescence image used for extracting the lattice orientation. The blue circles mark atoms that the algorithm will use for the Fourier transform. **b)** Black dots mark the centers of single atoms extracted from 10 different images like the one in a. For each of the 10 images, isolated atoms are found (marked in blue in a) and a 2D Gaussian is fitted to the images. All fitted centers are combined into a single image as the one shown. **c)** 2D Fourier transform of the image in b. The Fourier transform exhibits peaks at the reciprocal lattice vectors and multiples thereof. The circles mark the positions of the reciprocal lattice vectors. From these, the lattice orientation and the magnification of the imaging system can be extracted. The lattice orientation is illustrated in the top right of panels a and b. The extracted magnification in c) is around 128, or 101.6 nm/px, close to the expected magnification of 120.

NA = 0.8 objective ($r_A \approx 60 \mu\text{m}$). Using Zemax, this assumption was also tested. To reach a diffraction limited resolution (Strehl ratio > 0.8), the lens should be centered on the imaging beam better than $\pm 7 \text{ mm}$ and the tilt w.r.t. the imaging axis should be better than $\pm 2^\circ$. Away from these, the imaging system is not diffraction limited anymore, however the PSF also gets distorted significantly more than what is apparent in the measured PSF.

Another idea we had, which may explain the larger than expected PSF size is the extent of the atoms along the imaging direction. Due to its high NA, the imaging system has a very short depth of focus ($z_{\text{dof}} = \lambda/\text{NA}^2 \approx 1.3 \mu\text{m}$ at $\lambda = 852 \text{ nm}$). If the confinement along the vertical direction is small, the atom may be spread over a comparable distance, resulting in blurring of the PSF. Using Zemax, we have simulated the expected change in the PSF radius from an atom that extends over $8 \mu\text{m}$ along the focal direction and assuming a flat top density profile. This should overestimate the distortion of the PSF due to the spread of the atomic wavepacket at $10 \mu\text{K}$. We find that the change in the PSF size is negligible. The effect of the increased spread is mostly a disappearance of the first Airy disk minimum, which is replaced by a shoulder with an amplitude of around 20% of the maximum of the PSF.

6.6 Reconstruction

Because the PSF is larger than the lattice spacing $a_{\text{latt}} = 767 \text{ nm}/2 = 383.5 \text{ nm}$, atoms in adjacent lattice sites will not be resolved. This is not atypical for quantum gas microscopes, though the discrepancy between PSF radius and lattice spacing is particularly large in our case ($r_A/a_{\text{latt}} \approx 2.1$, typical values are $r_A/a_{\text{latt}} = 1 - 1.3$). To still reconstruct the lattice occupation, we need to deconvolute the image.

The first step is to reconstruct the lattice orientation and phase. In our case, this works well by taking images at low filling (Figure 6.7a) and fitting the position of single atoms. From the fitted positions an artificial image is created where a pixel is set to 1 if an atom was centered at that position and 0 otherwise (Figure 6.7b). The Fourier transform of that image (Figure 6.7c) exhibits spikes at the reciprocal lattice spacing from which lattice orientation and spacing can be extracted via $\vec{a}_i \vec{b}_j = 2\pi \delta_{ij}$. In principle, the phase of the lattice can be extracted from the phase of the Fourier transform at the

reciprocal lattice vectors \vec{b}_j . Alternatively, it can be fixed by finding a single (or more) atom somewhere on the image and fixing the origin at the atom's position (or using the average offset of more than one atom). The advantage of the second approach is that it is easy to implement for individual images, whereas the Fourier transformation would either rely on negligible drifts of the lattice phase between shots so averages over multiple images can be used or the ability to extract lattice spacing, orientation and phase from a single shot, which can be tricky at the low resolutions we are working with, especially when going to larger fillings.

Once the lattice sites have been determined, other experiments have used deconvolution algorithms such as the Richardson-Lucy algorithm [126] or Wiener deconvolution [13, 66, 123]. The idea behind these algorithm is that the recorded image $I(n, m)$ is the convolution of the lattice occupation $O(n, m)$ with the PSF ($\text{PSF}(n, m)$). This is equivalent to the product of their Fourier transforms, so in the absence of noise the lattice occupation may be reconstructed via

$$O(n, m) = \text{FT}^{-1} \{ \text{FT}[I(n, m)] / \text{FT}[\text{PSF}(n, m)] \}. \quad (6.1)$$

Noise will interfere with this reconstruction by artificially amplifying regions where the Fourier transform of the PSF is small. Wiener deconvolution attempts to address this by using a more robust inverse filter instead of $1/\text{FT}[\text{PSF}(n, m)]$:

$$O(n, m) = \text{FT}^{-1} \{ G(f_n, f_m) \text{FT}[I(n, m)] \}, \quad (6.2)$$

with the Wiener filter

$$G(f_n, f_m) = \frac{1}{\overline{\text{PSF}}(f_n, f_m)} \left\{ \frac{|\overline{\text{PSF}}(f_n, f_m)|^2}{|\overline{\text{PSF}}(f_n, f_m)|^2 + |\text{SNR}(f_n, f_m)|^{-2}} \right\}, \quad (6.3)$$

where $\overline{\text{PSF}} = \text{FT}[\text{PSF}(n, m)]$ and SNR is the ratio of the Fourier transforms of the occupations and the noise. Both, occupation and noise are not known initially, however, Ref. [224] describes an algorithm to estimate this from the input image¹⁶. The Richardson-Lucy algorithm on the other hand starts from an initial guess on the occupation and iteratively improves upon this according to [126, 225, 226]

$$O_{r+1}(n, m) = O_r(n, m) \left(\frac{I(n, m)}{O_r(n, m) * \text{PSF}(n, m)} * \text{PSF}^\dagger(n, m) \right), \quad (6.4)$$

where $\text{PSF}^\dagger(n, m)$ is the PSF mirrored about the origin (i.e. $\text{PSF}(r) = \text{PSF}^\dagger(-r)$) and $*$ denotes convolution. Typically, O_0 , the initial guess for the occupation is simply the measured image I . However, from the form of Equation 6.4 it becomes clear that the reconstructed occupation O_r will only have finite amplitude where $O_0 \neq 0$. This can be used during reconstruction by only setting those pixels in $O_0 \neq 0$ that are closest to the center of a site.

The default initial guess for the Richardson Lucy algorithm does not work very well for our imaging system, as the PSF extends over multiple lattice sites and therefore multiple PSFs will typically overlap. The algorithm in this case tends to merge multiple single emitters into one. However, choosing the initial guess such that its zero everywhere but at the lattice site center gives reasonable results for the reconstruction (Figure 6.8). Because the single site amplitudes of the algorithm are not constrained to integer values, the sites need to be thresholded to assign the occupation to a given site. Ideally, this should be done by fitting the histogram of the reconstruction with two Poisson distributions. The overlap between the two distribution gives a limit on the possible fidelity of the reconstruction.

To test the performance of the reconstruction, we repeated the deconvolution on simulated images for different filling and resolutions (Figure 6.9). To simulate the image, we specify a filling and the

¹⁶This algorithm is implemented in `skimage.restoration.unsupervised_wiener` of the `skimage` python package

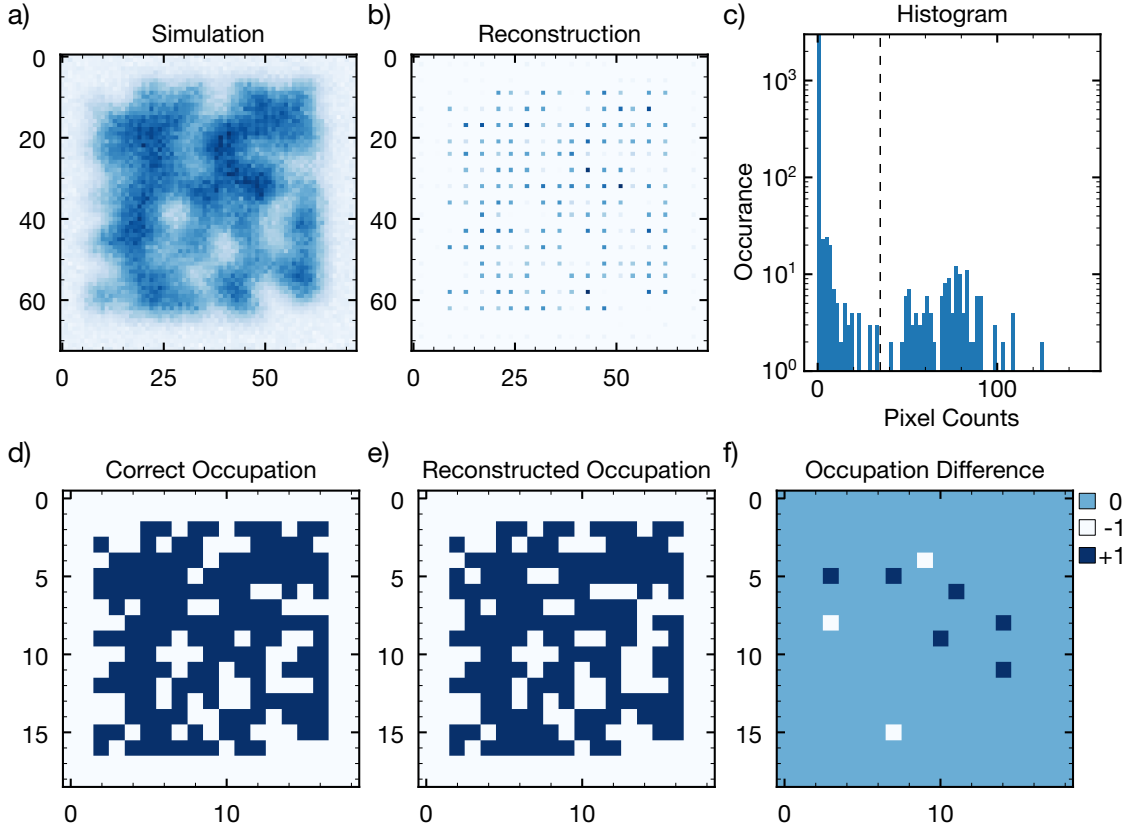


Figure 6.8 | **a)** Simulated image of 15×15 sites with 4×10^3 photons per atom, a PSF size of 860 nm and a filling fraction of 70%. **b)** Reconstructed amplitudes on each lattice site using the Richardson Lucy algorithm. The reconstructed image can be produced by convolution of the shown image with the PSF. As initial guess for the algorithm, only pixels closest to centers of lattice sites were set to non-zero values (see text). **c)** Histogram of the Richardson Lucy reconstruction shown in **b)**. There is a clear bimodality, associated with atoms present or not a given lattice site. The dashed line at 35 counts indicates the threshold chosen for the occupation reconstruction shown in **e)** **d)** Occupation used to produce the simulated image shown in **a)**. **e)** Occupation reconstructed from **b)** after thresholding, i.e. setting site amplitudes to 0 or 1 depending if the reconstructed amplitude at the given site is larger or smaller than the threshold. **f)** Difference between the correct and reconstructed occupation. 6 sites are wrongly empty in the reconstruction and 3 sites are wrongly filled. For 15×15 lattice sites this corresponds to a 96% of the lattice sites being reconstructed correctly.

number of lattice sites N_{sites} . We generate a random array of size $N_{\text{sites}} \times N_{\text{sites}}$, which represents the site occupation, and which has the chosen filling. Next we iterate over each site. If the site is filled, we pick N_{ph} samples from the PSF distribution of a single atom. N_{ph} is the number of photons per atom. We do not specify N_{ph} , but rather \bar{N}_{ph} , the mean photon number per atom, and pick N_{ph} from a Poisson distribution of mean \bar{N}_{ph} . Furthermore, we allow \bar{N}_{ph} to fluctuate for each site to model the intensity variation of the atom emission over the lattice. This variation can for instance be due to differences in molasses intensity. These samples are then binned into a second array, where each array entry represents a camera pixel. Finally, we add Gaussian distributed noise to each pixel to model read-out noise.

We find decent mean reconstruction fidelities $> 90\%$ for all fillings and tested resolutions (**Figure 6.9**). As expected, the reconstruction fidelity drops with the size of the PSF. The fidelity also drops with increasing filling and is minimal at 60–70% filling. Somewhat unexpected, the reconstruction fidelity increases

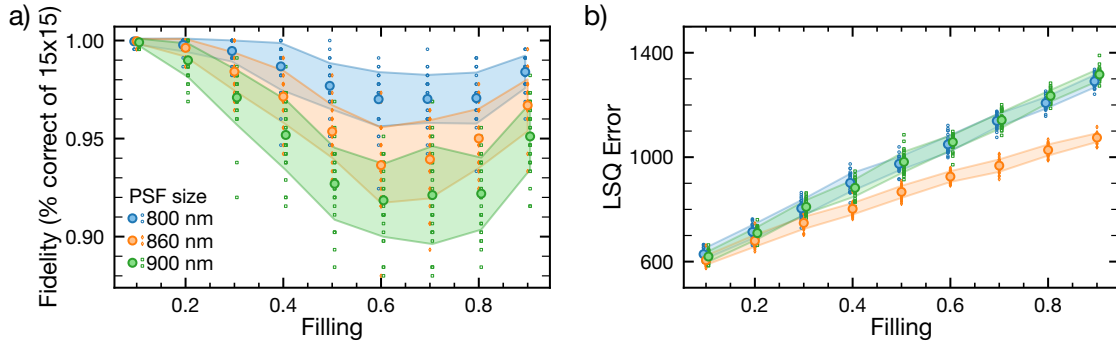


Figure 6.9 | **a)** Using simulated data at different filling and different resolution (PSF size indicates Airy radius), the reconstruction fidelity of a 15×15 site lattice using the Richardson-Lucy deconvolution is estimated. In all cases the photons per atom was 4×10^3 and the thresholding was fixed at a value of 35 counts. The open small symbols indicate individual reconstructions, the filled circles the mean and the shaded areas 1 standard deviation. The different PSF size data sets are offset from each other by 0.005 along the filling axis for visibility. **b)** The same data, but computing the squared error between the simulated image I and the reconstructed image R ($\sum \sqrt{(I - R)^2}$). For the squared error, no thresholding was performed. It is not clear where the large difference in squared error for 860 nm PSF size compared to 800 nm or 900 nm comes from. The increase in error with filling may be due to the increase in fluorescence and the associated noise (\sqrt{N} for N photons).

again for very high filling, but is not symmetric about 50% filling. If the reconstruction were symmetric, this would suggest that the reconstruction is equally good at reconstructing single atoms and holes.

As an alternative to the deconvolution based on the Richardson Lucy algorithm, the occupation may be fitted, or machine learning can be used [227]. To fit the occupation, we compute the image P_{ijk} generated by an atom on site k for each site. Given an occupation vector O_k (i.e. the flattened occupation matrix), the resulting image can be computed via matrix multiplication $G_{ij} = P_{ijk}O_k$. To fit a measured atom number distribution then involves optimization of the entries of the vector O_k . If O_k is not restricted to integer values, regular gradient descent techniques can be used. This yields similar results to the deconvolution based on the Richardson Lucy algorithm. We have also written an algorithm that tests a chosen set of changes to O_k (e.g. add an atom on site k or switch the occupation on site k with that on site $k + 1$). The algorithm computes the squared difference between the measured image I_{ij} and the reconstructed images $G_{ij}^{(n)}$, where n labels the possible changes applied to O_k . This algorithm is slow compared to deconvolution, but allows us to change the onsite occupation by finite values only (e.g. $O_k \in \{0, 1\}$). In this algorithm, the switching of site occupations is included to avoid getting stuck in local minima. For instance, the algorithm may have converged to a configuration where the site i is occupied instead of the sites $i - 1$ and $i + 1$. Adding atoms to site $i - 1$ or $i + 1$ or removing the atom from site i makes the least square error worse, but permutations of the local lattice occupation can improve on the fit.

The machine learning approach also allows us to fix the onsite occupation to either 1 or 0. In addition, once trained, the algorithm is also quite fast compared to the other methods. One problem in this approach is that a lot of training data is required. Assuming that one would train the algorithm on e.g. a 10×10 lattice, the training data set becomes rather big since each possible configuration (2^{100}) should be in the training data at least once. A more tractable approach is to train the algorithm to determine if the center site of a 5×5 lattice site array is occupied or not. Reconstruction can then proceed by feeding the neural network 5×5 lattice site crops around each lattice site. The choice of 5×5 lattice sites is determined by the extent of the single atom PSF, which in our case extends over this region. The training data is still relatively large, since one wants to train on all possible configurations in this array and also account for the noise due to read-out, dark current and the photon shot noise. Ideally, the training data would be generated by the experiment. There are two problems with this

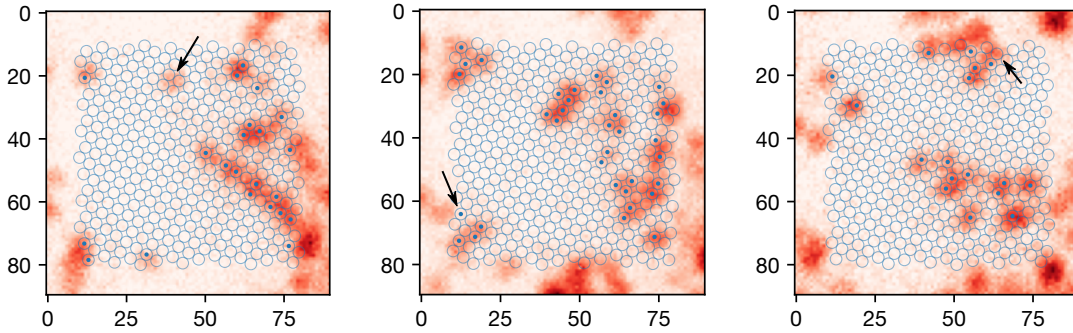


Figure 6.10 | Sample reconstructions of images of the atoms using the current code base for the Richardson-Lucy reconstruction. The blue circles indicate possible lattice sites, the blue dots indicate positions of reconstructed atoms. While the majority of the fitted atom locations seem plausible, some of the reconstructed sites are obviously wrong. A few are indicated with arrows in the figure. In the first, one atom was missed, likely because the offset of the lattice was not quite correct.

approach. One is that the experimental data is not labeled, the other is that so far we have not been able to control the filling in the lattices very well. In order to still push ahead, we have used simulated images for training. The simulations take the above noise sources into account and also allow a normal distributed variation of the fluorescence intensity of each atom. Some initial work on the machine learning based reconstruction has been done by one of the current PhD students in the lab, Alexander Impertro, and is currently being extended by a masters student [228].

At the time of writing of this thesis, the reconstruction of single atoms from fluorescence images is, unfortunately, still work in progress. While the different approaches outlined above have been tested on simulated images with reasonable success, their adoption to experimental images is still lacking. Figure 6.10 gives sample reconstructions of images taken at low filling using the Richardson-Lucy algorithm. While many atoms are properly found, some atoms are missed or some sites are filled even though the site seems empty when checked by eye.

6.7 Molasses optimization

Even without a fully working reconstruction, we can optimize the molasses cooling. We pin atoms in our lattice and turn on our molasses light. 60 ms after the start of the molasses we open the shutter in front of our CCD camera and take an image with 100 ms exposure time. We close the shutter, and wait for 680 ms before opening the shutter again for a second image, again with an exposure time of 100 ms. Between the two images the molasses is kept on.

We compare the first and second image to measure the hopping rate. Since we do not have a full reconstruction algorithm yet, we try to find single atoms in both images and compare their locations. Figure 6.11a illustrates the reconstruction. First, we find local maxima in a cropped region of both images. The peak finder finds not only atoms, but also many spurious background maxima. To remove those we sum in a 3×3 region around each found local maxima and fit a single Gaussian distribution to the resulting histogram. From the fit, we choose a threshold to filter out the found peaks. The threshold is chosen to be the fluorescence counts where the fitted distribution has dropped to 1% of its maximum.

The molasses optimization was still in progress during writing of this thesis, so only parts of the results are shown, and these are preliminary. In Figure 6.11b and c we scanned the molasses cooler detuning. We extract a signal to noise ratio as $1/(x_0 + \sigma)$ from the histograms where x_0 (σ) is the center ($1/e$ width) of the Gaussian distribution fitted to the data. This can be used because the fluorescence

counts are normalized to the interval $[0, 1]$. We find two maxima in the signal to noise ratio, one at around 40 MHz detuning, the other around 87 MHz detuning. Away from these the signal to noise ratio is worse, indicating that separating single atoms from the background becomes hard to impossible. Apart from the signal to noise ratio, we also extract the distance between peaks in the first and second image. Ideally, the distance will be zero for all points, and by considering the distribution of the distances between closest points in the first and second image we hope to extract information about the hopping rate. In [Figure 6.11c](#), an estimate of the number of atoms that hopped or were lost between the two images is plotted. For the estimate, the peaks left after thresholding are fitted with a 2D Gaussian. We use only those peaks where the 2D Gaussian has a $1/e$ size between 1 and 2 pixels. For those peaks, we compute for each peak in the first image the closest peak in the second image. If the distance between the peaks is larger than one lattice site (1.8 pixel), they are counted as having hopped. The number of lost atoms is given by the absolute value of the difference between the number of atoms in the two images. We find that, similar to the signal to noise ratio, the half distance is minimal around 50 MHz detuning and 87 MHz detuning. We also find that at the optimal signal to noise ratio (41 Hz), the half distance is slightly larger than at 87 MHz.

We also scanned the magnetic field during the molasses phase ([Figure 6.11d,e](#)). The molasses cooling efficiency is expected to be sensitive to the residual background field. By scanning the field, we can estimate how sensitive it is. We find that while the signal to noise ratio hardly changes, the number of hopped or lost atoms starts to increase beyond a field of 200 mG. Note that we have calibrated the magnetic background field independently using microwaves and find it compensated at 135 mG.

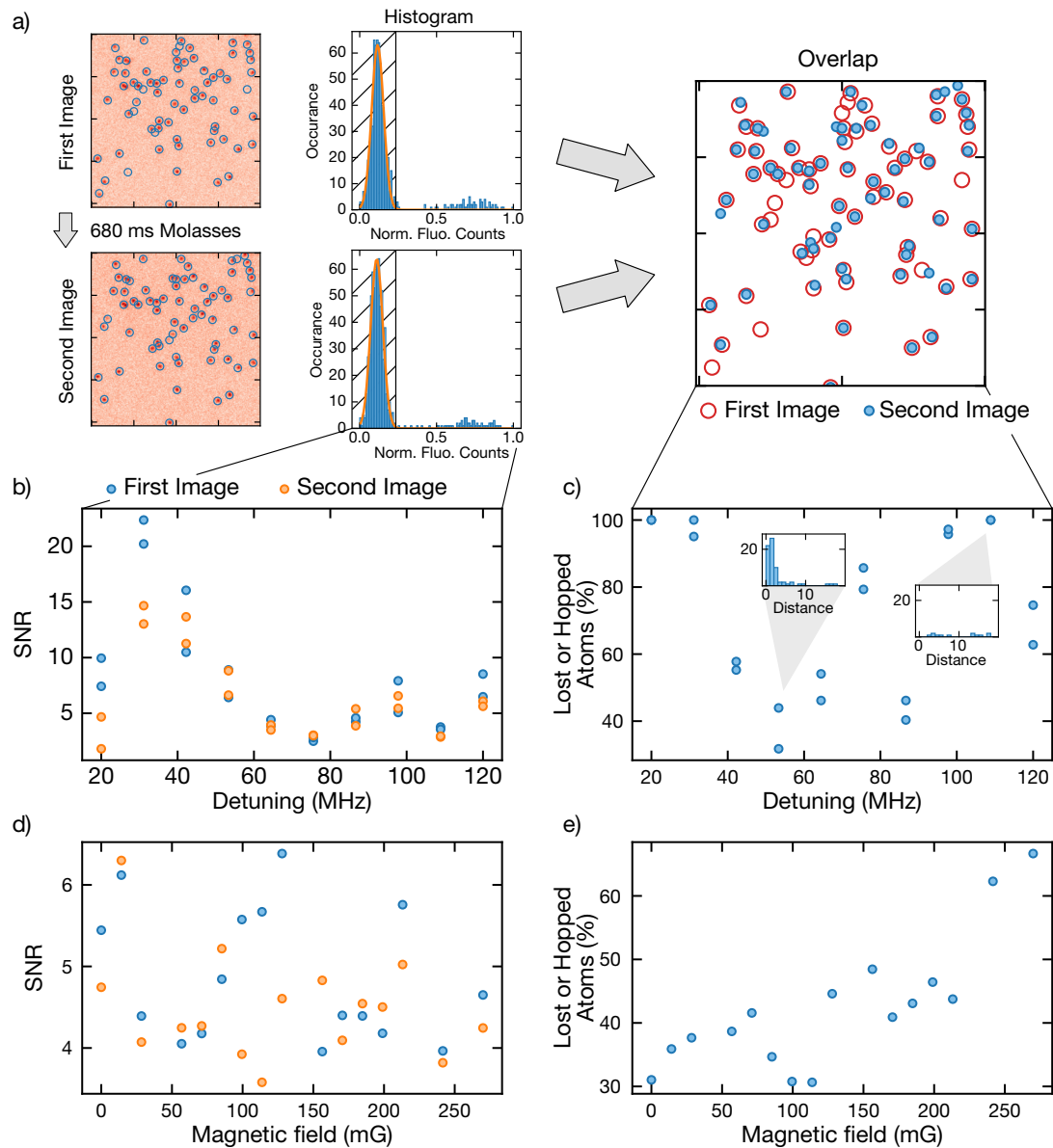


Figure 6.11 | a) Example images from a scan of the cooler detuning to illustrate the single atoms location reconstruction. The first row is the analysis of the first fluorescence image, the second row of the second fluorescence image taken 680 ms later. The blue circles in the fluorescence images indicate atom locations after thresholding. In the histogram plots, the orange curve is a Gaussian fit to low fluorescence count data. The black curve indicates the chosen threshold. Finally, the overlap on the right shows the identified peak locations in the first (red rings) and second (blue dots) image. The fluorescence data is from the detuning scan of the molasses cooler and corresponds to a detuning of 53 MHz. b) Signal-to-noise ratio (SNR) estimated from histograms as in a versus detuning (see text for definition). Blue and orange points show the signal to noise ratio in the first and second image respectively. The scan of the detuning was performed twice. c) Percentage of atoms that were lost or have hopped between the two images. If, for a given point in the first image, the closet point in the second image was further away than 1.7 pixel (1 lattice site), the atoms was counted as having hopped. The inset shows the distribution of distances between closest points. The number of lost or hopped atoms was normalized to the maximum number of atoms found in the first or second image. d) and e) show similar data as in b) and c) but versus magnetic offset field during imaging. The detuning for these images was 87 MHz. For b) and c) the magnetic offset field was 135 mG.

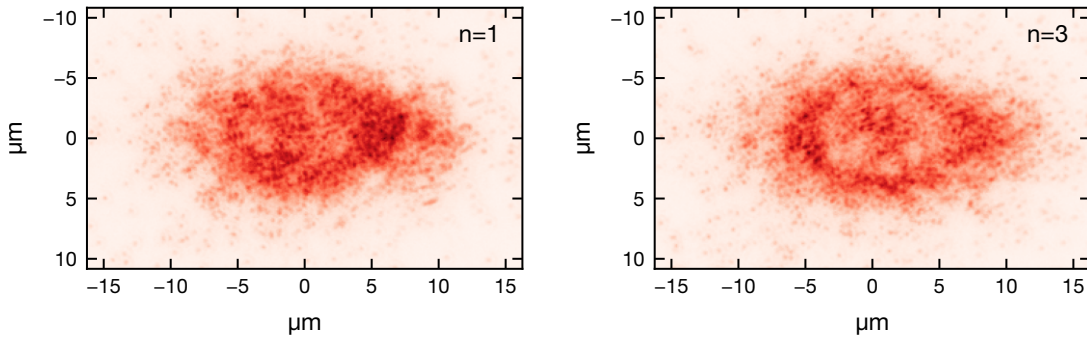


Figure 7.1 | First images of a Caesium Mott insulator taken with our fluorescence imaging system.

CHAPTER 7

Conclusion and Outlook

This thesis has described the general setup of the new Caesium quantum gas microscope, up to the point of loading atoms into a pinning lattice and imaging them with fluorescence photons. While the pre-cooling steps follow similar Caesium experiments (e.g. [98, 159]), the transport step between pre-cooling and condensation is novel [171] and makes direct adaption of the evaporation strategies of other Caesium experiments less straightforward. However, the transport allows us to move the atoms into a new section of the vacuum system, improving the optical access and thereby easing installation of lattices and objectives required for the quantum gas microscope. Even with the intermediate transport step, we reach condensation in a bit more than 10s. We have successfully loaded those atoms into a pinning lattice and managed to image single atoms using fluorescence photons captured by our high resolution microscope.

Though the construction of the experiment has progressed quite far, it is still not finished. As mentioned in the introduction, the goal of the experiment is the study of interacting topological many-body systems with single site resolution. As a first step in that direction, we plan to study the interacting Su-Schrieffer-Heeger (SSH) model in one and two dimensions. The canonical SSH model ([73], see Chapter 1 of [74] for an introduction), based on non-interacting fermions, exhibits edge modes that are protected by a chiral symmetry. For bosons, interactions are required to observe these modes [45, 48]. The higher-dimensional analog (2D SSH model) can exhibit symmetry protected corner modes in the presence of either flux [35] or interactions [229]. To realize these models in our system, a few key ingredients are still missing.

First, a superlattice is required to realize the staggered tunneling of the SSH model. For the superlattice, an optical lattice made from 1534 nm light will be locked to and overlapped with the existing 767 nm lattices. Secondly, we want sharp edges on the lattice potential to observe the corner modes. To do this, we plan to project repulsive potentials on the atoms using a digital micro mirror device

(DMD) and our high resolution objective. Third, the atoms need to be loaded into the lattices and a Mott insulator state needs to be prepared. So far, we have not worried much about the temperature of the atoms loaded into the lattices as we were mostly busy trying to align and characterize our imaging system. We got the first signal of a Mott insulator just before this thesis was finished. [Figure 7.1](#) shows an image of the parity projected Mott insulator, with the right image showing a reduced density at the $n = 2$ Mott lobe and $n = 1$ and $n = 3$ Mott lobes at the edge and center of the cloud respectively.

Another avenue of future work will be the installation of an anti-magic lattice. While the introduction mostly focuses on the use of the lattice for simulating artificial gauge fields, the small lattice spacing in the anti-magic lattice in principle also allows for non-negligible nearest neighbor interaction between atoms in different spin states. This would open the way for studying extended Bose-Hubbard models, which exhibit a rich phase diagram [\[230–232\]](#). Steps in this direction would be to load the atoms into an anti-magic lattice and trying to measure inter- and intra-species scattering lengths [\[69, 233\]](#).

Further in the future, the state-dependent lattice will be used to study interacting topological phases in the presence of a magnetic flux through the lattice. This may enable the realization and study of fractional Chern insulator states [\[81\]](#) on a new, highly tunable experimental platform.

Appendices

Appendix A Classical transport model

The apparent linear scaling of the relative transport efficiency with acceleration and Gaussian power is not understood. We tried modeling the system classically, by considering the dynamics of an atom in a tilted lattice potential $V(x) = -V_L \cos(4\pi x/\lambda) - max$ [165] (Figure A.1a–b). Here $V_L \propto \sqrt{P_G}$ is the lattice depth, λ the lattice laser wavelength, m the mass and a the acceleration. Substituting $x \rightarrow x' = 4\pi x/\lambda$ and $a \rightarrow a' = ma\lambda/4\pi V_L$ gives $V(x)/V_L = -a'x - \cos x$. $V(x)/V_L$ has extrema at $x_1 = \sin^{-1}(a) + 2\pi n$ and $x_2 = -\sin^{-1}(a) + 2\pi(n + 1/2)$, where the potential is $V(x_1)/V_L = -a' \sin^{-1}(a') - \sqrt{1 - a'^2}$ and $V(x_2)/V_L = a'(\sin^{-1}(a') + \pi) + \sqrt{1 - a'^2}$ respectively. From this model, we can extract for example a critical acceleration a_{crit} , beyond which the lattice does not have a local minimum anymore $\Delta V/V_L = a_{\text{crit}}(\pi + 2 \sin^{-1}(a_{\text{crit}})) + 2\sqrt{1 - a_{\text{crit}}^2} = 0$.

However, for sufficiently strong accelerations and instantaneous changes of the acceleration, the shift of the lattice minimum when changing the acceleration leads to a sudden increase of the atoms potential energy (Figure A.1a–b). This additional increase in potential energy would happen at every change of the acceleration and effectively reduce the critical acceleration. For a single acceleration, without deceleration, the critical acceleration is given by $a_{\text{crit}}(\sin^{-1}(a_{\text{crit}}) + \pi) + \sqrt{1 - a_{\text{crit}}^2} + 1 = 0$. Numerically, the critical acceleration in one way transport (two accelerations with opposite sign) is found to be $a'_{\text{crit}} = 0.42$ (Figure A.1c). Plugging in number from our experiment ($P_{\text{Bessel}} = 2.5$ W, $P_G = 6.5$ W, $\omega_{\text{Bessel}} = 80$ μm , $\omega_G = 200$ μm) this gives a critical acceleration in physical units $a_{\text{crit}} \approx 23$ km/s², i.e. much greater than what we test in experiment, suggesting that this is not the transport efficiency limiting process in the experiment.

The model so far does not take temperature into account. We tried to model the effect of temperature on the classical model above following [234, 235]. The density of states of thermal atoms in a potential is given by a Chi-squared distribution with 6 degrees of freedom (3 for kinetic and 3 for potential energy) provided the equipartition theorem applies. In this case the density of states is $f(E) = E^2 \exp[-E/k_B T]/2(k_B T)^2$ (Figure A.1d). Note that we estimate lattice trap frequencies of around 60–90 kHz, corresponding to harmonic oscillator energies of 3–4 μK . The temperature of the atoms in the lattice is measured to be 10 μK , so the equipartition theorem may still be applicable. We compute the transport efficiency by integrating the density of states up to the maximum effective potential depth, taking its reduction due to multiple accelerations into account. The resulting efficiency curves are illustrated in (Figure A.1e–f). Unfortunately, the resulting efficiency curves do not fit the measured data when using the lattice depth and the temperature as a free parameter.

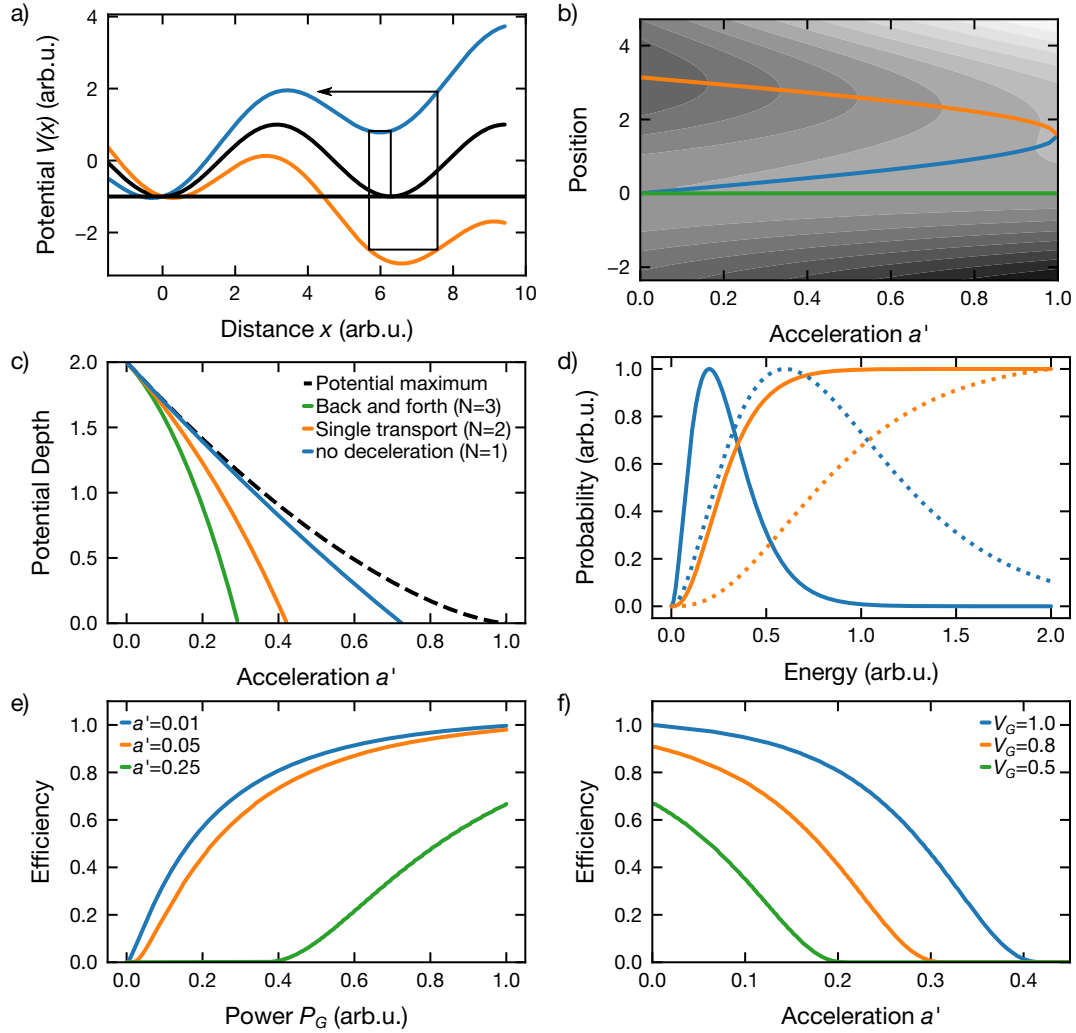


Figure A.1 | a) Effect of multiple accelerations on the back and forth transport. Shown are potential curves for static lattice (black), acceleration towards glass cell (increasing x , blue) and deceleration (orange). Arrow sketches how the non-adiabatic tilt of the lattice leads to an effective increase in the particles energy. b) Potential depth of the tilted lattice versus acceleration. Blue = local minimum, Orange = local maximum, Green = $x = 0$. c) Effective potential depth for different number of accelerations. The critical acceleration for a given number of accelerations and decelerations is where the potential depth crosses zero. d) Density of state (blue) for two different temperatures (solid line $T = 0.1$, dotted line $T = 0.3$) and cumulative distribution (orange) for classical particles trapped in a harmonic potential. e) Efficiency versus power of the laser generating the lattice at different accelerations. f) Efficiency versus acceleration for different powers. The temperature in e) and f) is $T = 0.3$.

References

- [1] M. Greiner, O. Mandel, T. Esslinger, T. W. Hänsch, and I. Bloch, *Quantum Phase Transition from a Superfluid to a Mott Insulator in a Gas of Ultracold Atoms*, *Nature* **415**, 39 (2002) (see pp. 1, 7, 8).
- [2] S. Nascimbène, N. Navon, K. J. Jiang, F. Chevy, and C. Salomon, *Exploring the Thermodynamics of a Universal Fermi Gas*, *Nature* **463**, 1057 (2010) (see p. 1).
- [3] I. Bloch, J. Dalibard, and S. Nascimbène, *Quantum Simulations with Ultracold Quantum Gases*, *Nat. Phys.* **8**, 267 (2012) (see pp. 1, 3).
- [4] K. Van Houcke, F. Werner, E. Kozik, N. Prokof'ev, B. Svistunov, M. J. H. Ku, A. T. Sommer, L. W. Cheuk, A. Schirotzek, and M. W. Zwierlein, *Feynman Diagrams versus Fermi-gas Feynman Emulator*, *Nat. Phys.* **8**, 366 (2012) (see p. 1).
- [5] I. M. Georgescu, S. Ashhab, and F. Nori, *Quantum Simulation*, *Reviews of Modern Physics* **86**, 153 (2014) (see pp. 1, 3).
- [6] M. Aidelsburger, M. Lohse, C. Schweizer, M. Atala, J. T. Barreiro, S. Nascimbène, N. R. Cooper, I. Bloch, and N. Goldman, *Measuring the Chern Number of Hofstadter Bands with Ultracold Bosonic Atoms*, *Nat. Phys.* **11**, 162 (2015) (see pp. 1, 5, 9, 10).
- [7] J.-y. Choi, S. Hild, J. Zeiher, P. Schauß, A. Rubio-Abadal, T. Yefsah, V. Khemani, D. A. Huse, I. Bloch, and C. Gross, *Exploring the Many-Body Localization Transition in Two Dimensions*, *Science* **352**, 1547 (2016) (see p. 1).
- [8] M. Schmitt, M. Wenzel, F. Böttcher, I. Ferrier-Barbut, and T. Pfau, *Self-Bound Droplets of a Dilute Magnetic Quantum Liquid*, *Nature* **539**, 259 (2016) (see p. 1).
- [9] C. R. Cabrera, L. Tanzi, J. Sanz, B. Naylor, P. Thomas, P. Cheiney, and L. Tarruell, *Quantum Liquid Droplets in a Mixture of Bose-Einstein Condensates*, *Science* **359**, 301 (2018) (see p. 1).
- [10] C. Mordini, D. Trypogeorgos, A. Farolfi, L. Wolswijk, S. Stringari, G. Lamporesi, and G. Ferrari, *Measurement of the Canonical Equation of State of a Weakly Interacting 3D Bose Gas*, *Phys. Rev. Lett.* **125**, 150404 (2020) (see p. 1).
- [11] W. S. Bakr, J. I. Gillen, A. Peng, S. Fölling, and M. Greiner, *A Quantum Gas Microscope for Detecting Single Atoms in a Hubbard-Regime Optical Lattice*, *Nature* **462**, 74 (2009) (see pp. 1, 2, 73, 74, 77).
- [12] J. F. Sherson, C. Weitenberg, M. Endres, M. Cheneau, I. Bloch, and S. Kuhr, *Single-Atom-Resolved Fluorescence Imaging of an Atomic Mott Insulator*, *Nature* **467**, 68 (2010) (see pp. 1–3, 8, 73, 74).
- [13] L. W. Cheuk, M. A. Nichols, M. Okan, T. Gersdorf, V. V. Ramasesh, W. S. Bakr, T. Lompe, and M. W. Zwierlein, *Quantum-Gas Microscope for Fermionic Atoms*, *Phys. Rev. Lett.* **114**, 193001 (2015) (see pp. 1, 2, 73, 74, 83).
- [14] M. Miranda, R. Inoue, Y. Okuyama, A. Nakamoto, and M. Kozuma, *Site-Resolved Imaging of Ytterbium Atoms in a Two-Dimensional Optical Lattice*, *Phys. Rev. A* **91**, 063414 (2015) (see pp. 1, 73, 74).
- [15] E. Haller, J. Hudson, A. Kelly, D. A. Cotta, B. Peaudecerf, G. D. Bruce, and S. Kuhr, *Single-Atom Imaging of Fermions in a Quantum-Gas Microscope*, *Nat. Phys.* **11**, 738 (2015) (see pp. 1, 2, 73, 74).
- [16] G. J. A. Edge, R. Anderson, D. Jervis, D. C. McKay, R. Day, S. Trotzky, and J. H. Thywissen, *Imaging and Addressing of Individual Fermionic Atoms in an Optical Lattice*, *Phys. Rev. A* **92**, 063406 (2015) (see pp. 1, 2, 73, 74).

-
- [17] C. Gross and W. S. Bakr, *Quantum Gas Microscopy for Single Atom and Spin Detection*, *Nat. Phys.*, **1** (2021) (see pp. 1, 3).
- [18] C. Chin, R. Grimm, P. Julienne, and E. Tiesinga, *Feshbach Resonances in Ultracold Gases*, *Reviews of Modern Physics* **82**, 1225 (2010) (see pp. 1, 2, 10, 11).
- [19] C. Weitenberg, M. Endres, J. F. Sherson, M. Cheneau, P. Schauß, T. Fukuhara, I. Bloch, and S. Kuhr, *Single-Spin Addressing in an Atomic Mott Insulator*, *Nature* **471**, 319 (2011) (see p. 1).
- [20] P. Zupancic, P. M. Preiss, R. Ma, A. Lukin, M. E. Tai, M. Rispoli, R. Islam, and M. Greiner, *Ultra-Precise Holographic Beam Shaping for Microscopic Quantum Control*, *Optics Express* **24**, 13881 (2016) (see pp. 1, 73).
- [21] C. Gross and I. Bloch, *Quantum Simulations with Ultracold Atoms in Optical Lattices*, *Science* **357**, 995 (2017) (see pp. 1, 3).
- [22] P. M. Preiss, R. Ma, M. E. Tai, J. Simon, and M. Greiner, *Quantum Gas Microscopy with Spin, Atom-Number, and Multilayer Readout*, *Phys. Rev. A* **91**, 041602 (2015) (see p. 1).
- [23] J. Koepsell, S. Hirthe, D. Bourgund, P. Sompet, J. Vijayan, G. Salomon, C. Gross, and I. Bloch, *Robust Bilayer Charge Pumping for Spin- and Density-Resolved Quantum Gas Microscopy*, *Phys. Rev. Lett.* **125**, 010403 (2020) (see p. 1).
- [24] T. Hartke, B. Oreg, N. Jia, and M. Zwierlein, *Doublon-Hole Correlations and Fluctuation Thermometry in a Fermi-Hubbard Gas*, *Phys. Rev. Lett.* **125**, 113601 (2020) (see p. 1).
- [25] D. Mitra, P. T. Brown, E. Guardado-Sanchez, S. S. Kondov, T. Devakul, D. A. Huse, P. Schauß, and W. S. Bakr, *Quantum Gas Microscopy of an Attractive Fermi-Hubbard System*, *Nat. Phys.* **14**, 173 (2018) (see p. 1).
- [26] M. Boll, T. A. Hilker, G. Salomon, A. Omran, J. Nespolo, L. Pollet, I. Bloch, and C. Gross, *Spin- and Density-Resolved Microscopy of Antiferromagnetic Correlations in Fermi-Hubbard Chains*, *Science* **353**, 1257 (2016) (see p. 1).
- [27] R. Islam, R. Ma, P. M. Preiss, M. Eric Tai, A. Lukin, M. Rispoli, and M. Greiner, *Measuring Entanglement Entropy in a Quantum Many-Body System*, *Nature* **528**, 77 (2015) (see p. 1).
- [28] Z. Wang, Y. Chong, J. D. Joannopoulos, and M. Soljačić, *Observation of Unidirectional Backscattering-Immune Topological Electromagnetic States*, *Nature* **461**, 772 (2009) (see p. 1).
- [29] M. C. Rechtsman, J. M. Zeuner, Y. Plotnik, Y. Lumer, D. Podolsky, F. Dreisow, S. Nolte, M. Segev, and A. Szameit, *Photonic Floquet Topological Insulators*, *Nature* **496**, 196 (2013) (see p. 1).
- [30] R. Süsstrunk and S. D. Huber, *Observation of Phononic Helical Edge States in a Mechanical Topological Insulator*, *Science* **349**, 47 (2015) (see p. 1).
- [31] A. B. Khanikaev, R. Fleury, S. H. Mousavi, and A. Alù, *Topologically Robust Sound Propagation in an Angular-Momentum-Biased Graphene-like Resonator Lattice*, *Nature Communications* **6**, 8260 (2015) (see p. 1).
- [32] L. M. Nash, D. Kleckner, A. Read, V. Vitelli, A. M. Turner, and W. T. M. Irvine, *Topological Mechanics of Gyroscopic Metamaterials*, *Proceedings of the National Academy of Sciences* **112**, 14495 (2015) (see p. 1).
- [33] S. Stützer, Y. Plotnik, Y. Lumer, P. Titum, N. H. Lindner, M. Segev, M. C. Rechtsman, and A. Szameit, *Photonic Topological Anderson Insulators*, *Nature* **560**, 461 (2018) (see p. 1).
- [34] M. Aidelsburger, S. Nascimbene, and N. Goldman, *Artificial Gauge Fields in Materials and Engineered Systems*, *Comptes Rendus Physique, Quantum Simulation / Simulation Quantique* **19**, 394 (2018) (see pp. 1, 3).
- [35] S. Mittal, V. V. Orre, G. Zhu, M. A. Gorlach, A. Poddubny, and M. Hafezi, *Photonic Quadrupole Topological Phases*, *Nature Photonics* **13**, 692 (2019) (see pp. 1, 89).
- [36] H. Miyake, G. A. Siviloglou, C. J. Kennedy, W. C. Burton, and W. Ketterle, *Realizing the Harper Hamiltonian with Laser-Assisted Tunneling in Optical Lattices*, *Phys. Rev. Lett.* **111**, 185302 (2013) (see pp. 1, 5).
- [37] M. Aidelsburger, M. Atala, M. Lohse, J. T. Barreiro, B. Paredes, and I. Bloch, *Realization of the Hofstadter Hamiltonian with Ultracold Atoms in Optical Lattices*, *Phys. Rev. Lett.* **111**, 185301 (2013) (see pp. 1, 5).

-
- [38] M. Atala, M. Aidelsburger, J. T. Barreiro, D. Abanin, T. Kitagawa, E. Demler, and I. Bloch, *Direct Measurement of the Zak Phase in Topological Bloch Bands*, *Nat. Phys.* **9**, 795 (2013) (see pp. 1, 3, 4).
- [39] G. Jotzu, M. Messer, R. Desbuquois, M. Lebrat, T. Uehlinger, D. Greif, and T. Esslinger, *Experimental Realization of the Topological Haldane Model with Ultracold Fermions*, *Nature* **515**, 237 (2014) (see p. 1).
- [40] M. Leder, C. Grossert, L. Sitta, M. Genske, A. Rosch, and M. Weitz, *Real-Space Imaging of a Topologically Protected Edge State with Ultracold Atoms in an Amplitude-Chirped Optical Lattice*, *Nature Communications* **7**, 13112 (2016) (see pp. 1, 4).
- [41] E. J. Meier, F. A. An, and B. Gadway, *Observation of the Topological Soliton State in the Su–Schrieffer–Heeger Model*, *Nature Communications* **7**, 13986 (2016) (see pp. 1, 4).
- [42] M. E. Tai, A. Lukin, M. Rispoli, R. Schittko, T. Menke, Dan Borgnia, P. M. Preiss, F. Grusdt, A. M. Kaufman, and M. Greiner, *Microscopy of the Interacting Harper–Hofstadter Model in the Two-Body Limit*, *Nature* **546**, 519 (2017) (see p. 1).
- [43] N. R. Cooper, J. Dalibard, and I. B. Spielman, *Topological Bands for Ultracold Atoms*, *Reviews of Modern Physics* **91**, 015005 (2019) (see pp. 1, 3, 4).
- [44] M. Tarnowski, F. N. Únal, N. Fläschner, B. S. Rem, A. Eckardt, K. Sengstock, and C. Weitenberg, *Measuring Topology from Dynamics by Obtaining the Chern Number from a Linking Number*, *Nature Communications* **10**, 1728 (2019) (see pp. 1, 5, 10).
- [45] S. de Léséleuc, V. Lienhard, P. Scholl, D. Barredo, S. Weber, N. Lang, H. P. Büchler, T. Lahaye, and A. Browaeys, *Observation of a Symmetry-Protected Topological Phase of Interacting Bosons with Rydberg Atoms*, *Science* **365**, 775 (2019) (see pp. 1, 4, 89).
- [46] K. Wintersperger, C. Braun, F. N. Únal, A. Eckardt, M. D. Liberto, N. Goldman, I. Bloch, and M. Aidelsburger, *Realization of an Anomalous Floquet Topological System with Ultracold Atoms*, *Nat. Phys.* **16**, 1058 (2020) (see pp. 1, 5).
- [47] L. Fidkowski and A. Kitaev, *Effects of Interactions on the Topological Classification of Free Fermion Systems*, *Phys. Rev. B* **81**, 134509 (2010) (see p. 1).
- [48] X. Chen, Z.-C. Gu, Z.-X. Liu, and X.-G. Wen, *Symmetry-Protected Topological Orders in Interacting Bosonic Systems*, *Science* **338**, 1604 (2012) (see pp. 1, 89).
- [49] S. Rachel, *Interacting Topological Insulators: A Review*, *Reports on Progress in Physics* **81**, 116501 (2018) (see p. 1).
- [50] W. P. Su and J. R. Schrieffer, *Fractionally Charged Excitations in Charge-Density-Wave Systems with Commensurability 3*, *Phys. Rev. Lett.* **46**, 738 (1981) (see p. 1).
- [51] R. B. Laughlin, *Anomalous Quantum Hall Effect: An Incompressible Quantum Fluid with Fractionally Charged Excitations*, *Phys. Rev. Lett.* **50**, 1395 (1983) (see p. 1).
- [52] F. D. M. Haldane, *Fractional Quantization of the Hall Effect: A Hierarchy of Incompressible Quantum Fluid States*, *Phys. Rev. Lett.* **51**, 605 (1983) (see p. 1).
- [53] B. I. Halperin, *Statistics of Quasiparticles and the Hierarchy of Fractional Quantized Hall States*, *Phys. Rev. Lett.* **52**, 1583 (1984) (see p. 1).
- [54] D. Arovas, J. R. Schrieffer, and F. Wilczek, *Fractional Statistics and the Quantum Hall Effect*, *Phys. Rev. Lett.* **53**, 722 (1984) (see p. 1).
- [55] B. Paredes and I. Bloch, *Minimum Instances of Topological Matter in an Optical Plaquette*, *Phys. Rev. A* **77**, 023603 (2008) (see p. 1).
- [56] P. G. Harper, *The General Motion of Conduction Electrons in a Uniform Magnetic Field, with Application to the Diamagnetism of Metals*, *Proceedings of the Physical Society. Section A* **68**, 879 (1955) (see pp. 1, 4).
- [57] D. R. Hofstadter, *Energy Levels and Wave Functions of Bloch Electrons in Rational and Irrational Magnetic Fields*, *Phys. Rev. B* **14**, 2239 (1976) (see pp. 1, 4).
- [58] F. D. M. Haldane, *Model for a Quantum Hall Effect without Landau Levels: Condensed-Matter Realization of the "Parity Anomaly"*, *Phys. Rev. Lett.* **61**, 2015 (1988) (see p. 1).

- [59] M. Aidelsburger, M. Atala, S. Nascimbène, S. Trotzky, Y.-A. Chen, and I. Bloch, *Experimental Realization of Strong Effective Magnetic Fields in an Optical Lattice*, *Phys. Rev. Lett.* **107**, 255301 (2011) (see pp. 1, 10).
- [60] T. Bilitewski and N. R. Cooper, *Scattering Theory for Floquet-Bloch States*, *Phys. Rev. A* **91**, 033601 (2015) (see p. 1).
- [61] A. Rubio-Abadal, M. Ippoliti, S. Hollerith, D. Wei, J. Rui, S. L. Sondhi, V. Khemani, C. Gross, and I. Bloch, *Floquet Prethermalization in a Bose-Hubbard System*, *Phys. Rev. X* **10**, 021044 (2020) (see p. 1).
- [62] D. Jaksch and P. Zoller, *Creation of Effective Magnetic Fields in Optical Lattices: The Hofstadter Butterfly for Cold Neutral Atoms*, *New Journal of Physics* **5**, 56 (2003) (see pp. 1, 3, 5, 8, 9, 73).
- [63] E. J. Mueller, *Artificial Electromagnetism for Neutral Atoms: Escher Staircase and Laughlin Liquids*, *Phys. Rev. A* **70**, 041603 (2004) (see pp. 1, 3, 9, 73).
- [64] F. Gerbier and J. Dalibard, *Gauge Fields for Ultracold Atoms in Optical Superlattices*, **12**, 033007 (2010) (see pp. 1, 3, 9, 73).
- [65] A. Omran, M. Boll, T. A. Hilker, K. Kleinlein, G. Salomon, I. Bloch, and C. Gross, *Microscopic Observation of Pauli Blocking in Degenerate Fermionic Lattice Gases*, *Phys. Rev. Lett.* **115**, 263001 (2015) (see pp. 2, 73, 74).
- [66] M. F. Parsons, F. Huber, A. Mazurenko, C. S. Chiu, W. Setiawan, K. Wooley-Brown, S. Blatt, and M. Greiner, *Site-Resolved Imaging of Fermionic ${}^6\text{Li}$ in an Optical Lattice*, *Phys. Rev. Lett.* **114**, 213002 (2015) (see pp. 2, 73, 74, 83).
- [67] H. Zhai, *Degenerate Quantum Gases with Spin–Orbit Coupling: A Review*, *Reports on Progress in Physics* **78**, 026001 (2015) (see p. 3).
- [68] J. Dalibard, *Introduction to the Physics of Artificial Gauge Fields*, Vol. 191: Quantum Matter at Ultralow Temperatures, Proceedings of the International School of Physics "Enrico Fermi" (IOS Press, 2016) (see p. 3).
- [69] C. Chin, V. Vuletić, A. J. Kerman, S. Chu, E. Tiesinga, P. J. Leo, and C. J. Williams, *Precision Feshbach Spectroscopy of Ultracold Cs_2* , *Phys. Rev. A* **70**, 032701 (2004) (see pp. 3, 10, 90).
- [70] M. V. Berry, *Quantal Phase Factors Accompanying Adiabatic Changes*, *Proceedings of the Royal Society of London. A. Mathematical and Physical Sciences* **392**, 45 (1984) (see p. 3).
- [71] D. Xiao, M.-C. Chang, and Q. Niu, *Berry Phase Effects on Electronic Properties*, *Reviews of Modern Physics* **82**, 1959 (2010) (see p. 3).
- [72] J. Zak, *Berry's Phase for Energy Bands in Solids*, *Phys. Rev. Lett.* **62**, 2747 (1989) (see p. 3).
- [73] W. P. Su, J. R. Schrieffer, and A. J. Heeger, *Solitons in Polyacetylene*, *Phys. Rev. Lett.* **42**, 1698 (1979) (see pp. 4, 89).
- [74] J. K. Asbóth, L. Oroszlány, and A. Pályi, *A Short Course on Topological Insulators: Band-structure Topology and Edge States in One and Two Dimensions*, Vol. 919, Lecture Notes in Physics (Springer), arXiv:1509.02295 (see pp. 4, 89).
- [75] M. Z. Hasan and C. L. Kane, *Colloquium: Topological Insulators*, *Reviews of Modern Physics* **82**, 3045 (2010) (see p. 4).
- [76] R. Jackiw and C. Rebbi, *Solitons with Fermion Number*, *Phys. Rev. D* **13**, 3398 (1976) (see p. 4).
- [77] D. J. Thouless, M. Kohmoto, M. P. Nightingale, and M. den Nijs, *Quantized Hall Conductance in a Two-Dimensional Periodic Potential*, *Phys. Rev. Lett.* **49**, 405 (1982) (see p. 4).
- [78] R. Peierls, *Zur Theorie des Diamagnetismus von Leitungselektronen*, *Zeitschrift für Physik* **80**, 763 (1933) (see p. 4).
- [79] J. M. Luttinger, *The Effect of a Magnetic Field on Electrons in a Periodic Potential*, *Physical Review* **84**, 814 (1951) (see p. 4).
- [80] M. Račiūnas, F. N. Ünal, E. Anisimovas, and A. Eckardt, *Creating, Probing, and Manipulating Fractionally Charged Excitations of Fractional Chern Insulators in Optical Lattices*, *Phys. Rev. A* **98**, 063621 (2018) (see p. 4).

-
- [81] C. Repellin, J. Léonard, and N. Goldman, *Fractional Chern Insulators of Few Bosons in a Box: Hall Plateaus from Center-of-Mass Drifts and Density Profiles*, *Phys. Rev. A* **102**, 063316 (2020) (see pp. 4, 90).
- [82] B. Wang, X.-Y. Dong, and A. Eckardt, *Measurable Signatures of Bosonic Fractional Chern Insulator States and Their Fractional Excitations in a Quantum-Gas Microscope*, arXiv:2111.01110 [cond-mat], arXiv:2111.01110 [cond-mat] (see p. 4).
- [83] A. Lazarides, A. Das, and R. Moessner, *Equilibrium States of Generic Quantum Systems Subject to Periodic Driving*, *Physical Review E* **90**, 012110 (2014) (see p. 5).
- [84] L. D'Alessio and M. Rigol, *Long-Time Behavior of Isolated Periodically Driven Interacting Lattice Systems*, *Phys. Rev. X* **4**, 041048 (2014) (see p. 5).
- [85] R. Grimm, M. Weidemüller, and Y. B. Ovchinnikov, *Optical Dipole Traps for Neutral Atoms*, *Advances In Atomic, Molecular, and Optical Physics* **42**, edited by B. Bederson and H. Walther, 95 (2000) (see pp. 5, 9).
- [86] M. Greiner, *Ultracold quantum gases in three-dimensional optical lattice potentials*, PhD thesis, Ludwig-Maximilians-Universität München (2003) (see pp. 7, 35).
- [87] I. Bloch, J. Dalibard, and W. Zwerger, *Many-Body Physics with Ultracold Gases*, *Reviews of Modern Physics* **80**, 885 (2008) (see p. 7).
- [88] D. Jaksch, C. Bruder, J. I. Cirac, C. W. Gardiner, and P. Zoller, *Cold Bosonic Atoms in Optical Lattices*, *Phys. Rev. Lett.* **81**, 3108 (1998) (see p. 7).
- [89] B. Capogrosso-Sansone, N. V. Prokof'ev, and B. V. Svistunov, *Phase Diagram and Thermodynamics of the Three-Dimensional Bose-Hubbard Model*, *Phys. Rev. B* **75**, 134302 (2007) (see p. 8).
- [90] N. Gemelke, X. Zhang, C.-L. Hung, and C. Chin, *In Situ Observation of Incompressible Mott-insulating Domains in Ultracold Atomic Gases*, *Nature* **460**, 995 (2009) (see p. 8).
- [91] M. Karski, L. Förster, J.-M. Choi, A. Steffen, W. Alt, D. Meschede, and A. Widera, *Quantum Walk in Position Space with Single Optically Trapped Atoms*, *Science* **325**, 174 (2009) (see p. 10).
- [92] C. Robens, J. Zopes, W. Alt, S. Brakhane, D. Meschede, and A. Alberti, *Low-Entropy States of Neutral Atoms in Polarization-Synthesized Optical Lattices*, *Phys. Rev. Lett.* **118**, 065302 (2017) (see p. 10).
- [93] S. Brakhane, *The Quantum Walk Microscope*, PhD thesis, University Bonn (2016) (see pp. 10, 74).
- [94] O. Mandel, M. Greiner, A. Widera, T. Rom, T. W. Hänsch, and I. Bloch, *Coherent Transport of Neutral Atoms in Spin-Dependent Optical Lattice Potentials*, *Phys. Rev. Lett.* **91**, 010407 (2003) (see p. 10).
- [95] F. Le Kien, V. I. Balykin, and K. Hakuta, *State-Insensitive Trapping and Guiding of Cesium Atoms Using a Two-Color Evanescent Field around a Subwavelength-Diameter Fiber*, *Journal of the Physical Society of Japan* **74**, 910 (2005) (see p. 10).
- [96] J. McKeever, J. R. Buck, A. D. Boozer, A. Kuzmich, H.-C. Nägerl, D. M. Stamper-Kurn, and H. J. Kimble, *State-Insensitive Cooling and Trapping of Single Atoms in an Optical Cavity*, *Phys. Rev. Lett.* **90**, 133602 (2003) (see p. 10).
- [97] J. Dalibard, *Collisional Dynamics of Ultra-Cold Atomic Gases*, *Bose-Einstein Condensation in Atomic Gases, Proceedings of the International School of Physics "Enrico Fermi"*, 321 (1999) (see p. 10).
- [98] M. Gustavsson, *A Quantum Gas with Tunable Interactions in an Optical Lattice*, PhD thesis, Leopold-Franzen-Universität Innsbruck (2008) (see pp. 10, 11, 25, 33, 39, 41, 64, 89).
- [99] P.-T. Kraemer, *Few-Body Interactions in an Ultracold Gas of Cesium Atoms*, PhD thesis, Leopold-Franzen-Universität Innsbruck (2006) (see pp. 11, 63).
- [100] T. Kraemer, J. Herbig, M. Mark, T. Weber, C. Chin, H.-C. Nägerl, and R. Grimm, *Optimized Production of a Cesium Bose-Einstein Condensate*, *Applied Physics B* **79**, 1013 (2004) (see pp. 11, 63).
- [101] M. Zaccanti, B. Deissler, C. D'Errico, M. Fattori, M. Jona-Lasinio, S. Müller, G. Roati, M. Inguscio, and G. Modugno, *Observation of an Efimov Spectrum in an Atomic System*, *Nat. Phys.* **5**, 586 (2009) (see p. 11).
- [102] L. J. Wacker, N. B. Jørgensen, D. Birkmose, N. Winter, M. Mikkelsen, J. Sherson, N. Zinner, and J. J. Arlt, *Universal Three-Body Physics in Ultracold KRb Mixtures*, *Phys. Rev. Lett.* **117**, 163201 (2016) (see p. 11).

- [103] T. Kraemer, M. Mark, P. Waldburger, J. G. Danzl, C. Chin, B. Engeser, A. D. Lange, K. Pilch, A. Jaakkola, H.-C. Nägerl, and R. Grimm, *Evidence for Efimov Quantum States in an Ultracold Gas of Caesium Atoms*, *Nature* **440**, 315 (2006) (see pp. 11, 63).
- [104] V. Efimov, *Energy Levels Arising from Resonant Two-Body Forces in a Three-Body System*, *Physics Letters B* **33**, 563 (1970) (see p. 11).
- [105] J. P. D’Incao, H. Suno, and B. D. Esry, *Limits on Universality in Ultracold Three-Boson Recombination*, *Phys. Rev. Lett.* **93**, 123201 (2004) (see p. 11).
- [106] M. Berninger, A. Zenesini, B. Huang, W. Harm, H.-C. Nägerl, F. Ferlaino, R. Grimm, P. S. Julienne, and J. M. Hutson, *Universality of the Three-Body Parameter for Efimov States in Ultracold Cesium*, *Phys. Rev. Lett.* **107**, 120401 (2011) (see p. 11).
- [107] R. J. Wild, P. Makotyn, J. M. Pino, E. A. Cornell, and D. S. Jin, *Measurements of Tan’s Contact in an Atomic Bose-Einstein Condensate*, *Phys. Rev. Lett.* **108**, 145305 (2012) (see p. 11).
- [108] S. Roy, *Test of the Universality of the Three-Body Efimov Parameter at Narrow Feshbach Resonances*, *Phys. Rev. Lett.* **111**, 10.1103/PhysRevLett.111.053202 (2013) (see p. 11).
- [109] J. Johansen, B. J. DeSalvo, K. Patel, and C. Chin, *Testing Universality of Efimov Physics across Broad and Narrow Feshbach Resonances*, *Nat. Phys.* **13**, 731 (2017) (see p. 11).
- [110] J. E. Sansonetti, *Wavelengths, Transition Probabilities, and Energy Levels for the Spectra of Cesium ($Cs_I - Cs_{IV}$)*, *Journal of Physical and Chemical Reference Data* **38**, 761 (2009) (see p. 13).
- [111] D. A. Steck, *Cesium D Line Data* (see pp. 13, 33, 35, 39).
- [112] R. K. Raj, D. Bloch, J. J. Snyder, G. Camy, and M. Ducloy, *High-Frequency Optically Heterodyned Saturation Spectroscopy Via Resonant Degenerate Four-Wave Mixing*, *Phys. Rev. Lett.* **44**, 1251 (1980) (see p. 14).
- [113] H. N. Rutt, *A Heterodyne Frequency Offset Locking Technique for Pulsed or CW Lasers*, *Journal of Physics E: Scientific Instruments* **17**, 704 (1984) (see p. 14).
- [114] D. J. McCarron, S. A. King, and S. L. Cornish, *Modulation Transfer Spectroscopy in Atomic Rubidium*, *Measurement Science and Technology* **19**, 105601 (2008) (see pp. 14, 21).
- [115] A. Reetz, *Laser Cooling, Transport and Imaging of Caesium Atoms*, MA thesis, Ludwig-Maximilians-Universität München (2018) (see p. 14).
- [116] J. H. Shirley, *Modulation Transfer Processes in Optical Heterodyne Saturation Spectroscopy*, *Opt. Lett.*, **OL 7**, 537 (1982) (see p. 14).
- [117] E. A. Donley, T. P. Heavner, F. Levi, M. O. Tataw, and S. R. Jefferts, *Double-Pass Acousto-Optic Modulator System*, *Review of Scientific Instruments* **76**, 063112 (2005) (see p. 16).
- [118] I. Petitbon, P. Gallion, G. Debarge, and C. Chabran, *Locking Bandwidth and Relaxation Oscillations of an Injection-Locked Semiconductor Laser*, *IEEE Journal of Quantum Electronics* **24**, 148 (1988) (see p. 19).
- [119] S. Wiczorek, B. Krauskopf, T. B. Simpson, and D. Lenstra, *The Dynamical Complexity of Optically Injected Semiconductor Lasers*, *Physics Reports* **416**, 1 (2005) (see p. 19).
- [120] P. Unterwaditzer, *Aufbau Eines Vollst Ändigen Diodenlasersystems Zur Laserkühlung Und Detektion von Gespeicherten Cs-Atomen*, Diplomarbeit, Leopold-Franzen-Universität Innsbruck (2006) (see p. 19).
- [121] J. F. Wienand, *Multi-Level Fluorescence Imaging and Degenerate Raman Sideband Cooling for a Caesium Quantum Gas Microscope*, MA thesis, Ludwig-Maximilians-Universität München (2019) (see pp. 19–21, 41).
- [122] N. Bobroff, *Position Measurement with a Resolution and Noise-Limited Instrument*, *Review of Scientific Instruments* **57**, 1152 (1986) (see p. 20).
- [123] A. Alberti, C. Robens, W. Alt, S. Brakhane, M. Karski, R. Reimann, A. Widera, and D. Meschede, *Super-Resolution Microscopy of Single Atoms in Optical Lattices*, *New Journal of Physics* **18**, 053010 (2016) (see pp. 20, 74, 83).

- [124] O. S. Heavens, *Radiative Transition Probabilities of the Lower Excited States of the Alkali Metals*, *JOSA* **51**, 1058 (1961) (see p. 20).
- [125] M. S. Safronova, U. I. Safronova, and C. W. Clark, *Magic Wavelengths, Matrix Elements, Polarizabilities, and Lifetimes of Cs*, *Phys. Rev. A* **94**, 012505 (2016) (see p. 20).
- [126] T. Hilker, *Spin-resolved microscopy of strongly correlated fermionic many-body states*, PhD thesis, Ludwig-Maximilians-Universität München (2017) (see pp. 20, 83).
- [127] G. C. Bjorklund, M. D. Levenson, W. Lenth, and C. Ortiz, *Frequency Modulation (FM) Spectroscopy*, *Applied Physics B* **32**, 145 (1983) (see p. 20).
- [128] S. Hubele, *Tbd*, MA thesis, Ludwig-Maximilians-Universität München (2022) (see p. 21).
- [129] H. J. Lewandowski, D. M. Harber, D. L. Whitaker, and E. A. Cornell, *Simplified System for Creating a Bose-Einstein Condensate*, *Journal of Low Temperature Physics* **132**, 309 (2003) (see pp. 22, 45).
- [130] R. Senaratne, S. V. Rajagopal, Z. A. Geiger, K. M. Fujiwara, V. Lebedev, and D. M. Weld, *Effusive Atomic Oven Nozzle Design Using an Aligned Microcapillary Array*, *Review of Scientific Instruments* **86**, 023105 (2015) (see p. 23).
- [131] F. Scazza, *Probing $SU(N)$ -symmetric orbital interactions with ytterbium Fermi gases in optical lattices*, PhD thesis, Ludwig-Maximilians-Universität München (2015) (see p. 23).
- [132] E. Friedman, *Erich's Packing Center*, <https://erich-friedman.github.io/packing/index.html>, 2021 (see p. 23).
- [133] N. Ramsey, *Molecular Beams*, Oxford Classic Texts in the Physical Sciences (Oxford University Press, Oxford, New York, Jan. 1986) (see p. 23).
- [134] D. Sabulsky, *A Cesium-133 Effusive Oven for Ultracold Atomic Experiments*, Bachelor Thesis, University of Chicago (2014) (see p. 23).
- [135] C. J. Dedman, J. Nes, T. M. Hanna, R. G. Dall, K. G. H. Baldwin, and A. G. Truscott, *Optimum Design and Construction of a Zeeman Slower for Use with a Magneto-Optic Trap*, *Review of Scientific Instruments* **75**, 5136 (2004) (see pp. 24, 25).
- [136] J. Krieger, *Zeeman-Slower Und Experimentsteuerung Für Das NaLi-Experiment*, Diplomarbeit, Uni Heidelberg (2008) (see p. 24).
- [137] T. Weber, *Bose-Einstein Condensation of Optically Trapped Cesium*, PhD thesis, Leopold-Franzen-Universität Innsbruck (2003) (see pp. 25, 39, 41, 63).
- [138] J. C. Simpson, J. E. Lane, C. D. Immer, R. C. Youngquist, and T. Steinrock, *Simple Analytic Expressions for the Magnetic Field of a Circular Current Loop*, Jan. 2001 (see p. 26).
- [139] H. von Raven, *Tbd*, PhD thesis, Ludwig-Maximilians-Universität München (2022) (see pp. 27, 30–32, 36, 63, 71, 72, 77).
- [140] R. J. Reid, *Cleaning for Vacuum Service*, *CERN*, 10.5170/CERN-1999-005.139 (1999) (see p. 27).
- [141] R. Grinham and A. Chew, *A Review of Outgassing and Methods for Its Reduction*, *Applied Science and Convergence Technology* **26**, 95 (2017) (see p. 27).
- [142] E. Vacuum, *Working with Vacuum - An Introduction*, MPQ, 2018 (see p. 28).
- [143] C. Bernhard, *Structural and Functional Adaptation in a Visual System*, *Endeavour* **26**, 79 (1967) (see p. 29).
- [144] P. B. Clapham and M. C. Hutley, *Reduction of Lens Reflexion by the "Moth Eye" Principle*, *Nature* **244**, 281 (1973) (see p. 29).
- [145] TelAztec, *Micro-Textured Surface Treatments For Enhanced Performance Optics and Windows*, <https://telaztec.com/technology.html>, 2008 (see p. 29).
- [146] W. H. Lowdermilk and D. Milam, *Graded-index Antireflection Surfaces for High-power Laser Applications*, *Applied Physics Letters* **36**, 891 (1980) (see p. 29).
- [147] B. D. MacLeod and D. S. Hobbs, *Long Life, High Performance Anti-Reflection Treatment for HgCdTe Infrared Focal Plane Arrays*, in *Infrared Technology and Applications XXXIV*, Vol. 6940 (Apr. 2008), 318 (see p. 29).

- [148] E. Brion, L. H. Pedersen, and K. Mølmer, *Adiabatic Elimination in a Lambda System*, *Journal of Physics A: Mathematical and Theoretical* **40**, 1033 (2007) (see p. 31).
- [149] W. Ketterle, D. S. Durfee, and D. M. Stamper-Kurn, *Making, Probing and Understanding Bose-Einstein Condensates*, *Bose-Einstein Condensation in Atomic Gases, Proceedings of the International School of Physics "Enrico Fermi"* **140**, 67 (1999), arXiv:cond-mat/9904034 (see pp. 33, 34).
- [150] T. Pyragius, *Developing and Building an Absorption Imaging System for Ultracold Atoms*, arXiv, arXiv:1209.3408 (see p. 33).
- [151] J. Herbig, *Quantum-Degenerate Cesium: Atoms and Molecules*, PhD thesis, Leopold-Franzen-Universität Innsbruck (2005) (see pp. 34, 64).
- [152] B. Gadway, D. Pertot, R. Reimann, M. G. Cohen, and D. Schneble, *Analysis of Kapitza-Dirac Diffraction Patterns beyond the Raman-Nath Regime*, *Optics Express* **17**, 19173 (2009) (see pp. 34, 35).
- [153] M. E. Gehm, K. M. O'Hara, T. A. Savard, and J. E. Thomas, *Dynamics of Noise-Induced Heating in Atom Traps*, *Phys. Rev. A* **58**, 3914 (1998) (see p. 35).
- [154] M. Greiner, I. Bloch, O. Mandel, T. W. Hänsch, and T. Esslinger, *Exploring Phase Coherence in a 2D Lattice of Bose-Einstein Condensates*, *Phys. Rev. Lett.* **87**, 160405 (2001) (see p. 35).
- [155] M. Greiner, I. Bloch, O. Mandel, T. Hänsch, and T. Esslinger, *Bose-Einstein Condensates in 1D- and 2D Optical Lattices*, *Applied Physics B* **73**, 769 (2001) (see p. 35).
- [156] M. T. DePue, S. Lukman Winoto, D. J. Han, and D. S. Weiss, *Transient Compression of a MOT and High Intensity Fluorescent Imaging of Optically Thick Clouds of Atoms*, *Optics Communications* **180**, 73 (2000) (see p. 38).
- [157] E. Donley, T. Heavner, J. O'Brien, S. Jefferts, and F. Levi, *Laser Cooling and Launching Performance in a (1,1,1)-Geometry Atomic Fountain*, in *Proceedings of the 2005 IEEE International Frequency Control Symposium and Exposition, 2005*. (2005), 292 (see pp. 39, 46).
- [158] A. Flir, *Implementierung Und Untersuchung von Raman-Seitenbandkühlung Zur Erzeugung Eines Ultrakalten Cäsiumgase*, Diplomarbeit, Leopold-Franzen-Universität Innsbruck (2006) (see p. 39).
- [159] C.-L. Hung, *In Situ Probing of Two-Dimensional Quantum Gases*, PhD thesis, University of Chicago (2011) (see pp. 39, 49, 89).
- [160] A. Kastberg, W. D. Phillips, S. L. Rolston, R. J. C. Spreeuw, and P. S. Jessen, *Adiabatic Cooling of Cesium to 700 nK in an Optical Lattice*, *Phys. Rev. Lett.* **74**, 1542 (1995) (see p. 41).
- [161] A. J. Kerman, *Raman Sideband Cooling and Cold Atomic Collisions in Optical Lattices*, PhD thesis, Stanford University (2002) (see p. 41).
- [162] E. Haller, *Private Communication*, Apr. 2020 (see p. 43).
- [163] M. Greiner, I. Bloch, T. W. Hänsch, and T. Esslinger, *Magnetic Transport of Trapped Cold Atoms over a Large Distance*, *Phys. Rev. A* **63**, 031401 (2001) (see p. 45).
- [164] T. L. Gustavson, A. P. Chikkatur, A. E. Leanhardt, A. Görlitz, S. Gupta, D. E. Pritchard, and W. Ketterle, *Transport of Bose-Einstein Condensates with Optical Tweezers*, *Phys. Rev. Lett.* **88**, 020401 (2001) (see p. 45).
- [165] D. Schrader, S. Kuhr, W. Alt, M. Müller, V. Gomer, and D. Meschede, *An Optical Conveyor Belt for Single Neutral Atoms*, *Applied physics. B, Lasers and optics* **73**, 819 (2001) (see pp. 45, 46, 91).
- [166] J. Goldwin, S. Inouye, M. L. Olsen, B. Newman, B. D. DePaola, and D. S. Jin, *Measurement of the Interaction Strength in a Bose-Fermi Mixture with ^{87}Rb and ^{40}K* , *Phys. Rev. A* **70**, 021601 (2004) (see p. 45).
- [167] S. Schmid, G. Thalhammer, K. Winkler, F. Lang, and J. H. Denschlag, *Long Distance Transport of Ultracold Atoms Using a 1D Optical Lattice*, *New Journal of Physics* **8**, 159 (2006) (see pp. 45, 46, 52, 61).
- [168] J. Léonard, M. Lee, A. Morales, T. M. Karg, T. Esslinger, and T. Donner, *Optical Transport and Manipulation of an Ultracold Atomic Cloud Using Focus-Tunable Lenses*, *New Journal of Physics* **16**, 093028 (2014) (see pp. 45, 46).

- [169] C. Gross, H. C. J. Gan, and K. Dieckmann, *All-Optical Production and Transport of a Large ^6Li Quantum Gas in a Crossed Optical Dipole Trap*, *Phys. Rev. A* **93**, 053424 (2016) (see pp. 45, 46).
- [170] M. Langbecker, R. Wirtz, F. Knoch, M. Noaman, T. Speck, and P. Windpassinger, *Highly Controlled Optical Transport of Cold Atoms into a Hollow-Core Fiber*, *New Journal of Physics* **20**, 083038 (2018) (see pp. 45, 46).
- [171] G. Unnikrishnan, C. Beulenkamp, D. Zhang, K. P. ZamarSKI, M. Landini, and H.-C. Nägerl, *Long Distance Optical Transport of Ultracold Atoms: A Compact Setup Using a Moiré Lens*, *Review of Scientific Instruments* **92**, 063205 (2021) (see pp. 45, 46, 89).
- [172] T. Klostermann, C. R. Cabrera, H. von Raven, J. F. Wienand, C. Schweizer, I. Bloch, and M. Aidelsburger, *Fast Long-Distance Transport of Cold Cesium Atoms*, arXiv:2109.03804 [cond-mat, physics:quant-ph], arXiv:2109.03804 [cond-mat, physics:quant-ph] (see p. 45).
- [173] S. Bize et al., *Cold Atom Clocks and Applications*, *Journal of Physics B: Atomic, Molecular and Optical Physics* **38**, S449 (2005) (see p. 46).
- [174] T. Weber, J. Herbig, M. Mark, H.-C. Nägerl, and R. Grimm, *Bose-Einstein Condensation of Cesium*, *Science* (2003) (see pp. 47, 63).
- [175] M. T. DePue, C. McCormick, S. L. Winoto, S. Oliver, and D. S. Weiss, *Unity Occupation of Sites in a 3D Optical Lattice*, *Phys. Rev. Lett.* **82**, 2262 (1999) (see p. 49).
- [176] J. Hu, A. Urvoy, Z. Vendeiro, V. Crépel, W. Chen, and V. Vuletić, *Creation of a Bose-condensed Gas of 87Rb by Laser Cooling*, *Science (New York, N.Y.)* **358**, 1078 (2017) (see p. 49).
- [177] V. Vuletić, C. Chin, A. J. Kerman, and S. Chu, *Degenerate Raman Sideband Cooling of Trapped Cesium Atoms at Very High Atomic Densities*, *Phys. Rev. Lett.* **81**, 5768 (1998) (see p. 49).
- [178] N. Lorenz, *Private Communication*, Jan. 2020 (see p. 51).
- [179] P. Carruthers and M. M. Nieto, *Coherent States and the Forced Quantum Oscillator*, *American Journal of Physics* **33**, 537 (1965) (see p. 52).
- [180] R. Reichle, D. Leibfried, R. Blakestad, J. Britton, J. Jost, E. Knill, C. Langer, R. Ozeri, S. Seidelin, and D. Wineland, *Transport Dynamics of Single Ions in Segmented Microstructured Paul Trap Arrays*, *Fortschritte der Physik* **54**, 666 (2006) (see p. 52).
- [181] E. Torrontegui, S. Ibáñez, X. Chen, A. Ruschhaupt, D. Guéry-Odelin, and J. G. Muga, *Fast Atomic Transport without Vibrational Heating*, *Phys. Rev. A* **83**, 013415 (2011) (see p. 52).
- [182] M. R. Lam, *Demonstration of Quantum Brachistochrones between Distant States of an Atom*, *Phys. Rev. X* **11**, 10.1103/PhysRevX.11.011035 (2021) (see p. 52).
- [183] J. Durnin, *Exact Solutions for Nondiffracting Beams. I. The Scalar Theory*, *JOSA A* **4**, 651 (1987) (see p. 53).
- [184] J. H. McLeod, *The Axicon: A New Type of Optical Element*, *JOSA* **44**, 592 (1954) (see p. 53).
- [185] G. Scott and N. McArdle, *Efficient Generation of Nearly Diffraction-Free Beams Using an Axicon*, *Optical Engineering* **31**, 2640 (1992) (see p. 53).
- [186] O. Brzobohatý, T. Čížmár, and P. Zemánek, *High Quality Quasi-Bessel Beam Generated by Round-Tip Axicon*, *Optics Express* **16**, 12688 (2008) (see pp. 53, 54).
- [187] J. Durnin, J. J. Miceli, and J. H. Eberly, *Diffraction-Free Beams*, *Phys. Rev. Lett.* **58**, 1499 (1987) (see p. 53).
- [188] J. Turunen, A. Vasara, and A. T. Friberg, *Holographic Generation of Diffraction-Free Beams*, *Applied Optics* **27**, 3959 (1988) (see p. 53).
- [189] A. Vasara, J. Turunen, and A. T. Friberg, *Realization of General Nondiffracting Beams with Computer-Generated Holograms*, *JOSA A* **6**, 1748 (1989) (see p. 53).
- [190] C. López-Mariscal, J. C. Gutiérrez-Vega, and S. Chávez-Cerda, *Production of High-Order Bessel Beams with a Mach-Zehnder Interferometer*, *Applied Optics* **43**, 5060 (2004) (see p. 53).
- [191] W.-X. Cong, N.-X. Chen, and B.-Y. Gu, *Generation of Nondiffracting Beams by Diffractive Phase Elements*, *JOSA A* **15**, 2362 (1998) (see p. 53).

- [192] E. Rogers, *PyHank*, 2021 (see p. 54).
- [193] J. Chen, *Fast Long-distance Transport of Caesium Atoms and Bichromatic Superlattice*, MA thesis, Ludwig-Maximilians-Universität München (2020) (see p. 55).
- [194] T. Middelmann, S. Falke, C. Lisdat, and U. Sterr, *Long-Range Transport of Ultracold Atoms in a Far-Detuned One-Dimensional Optical Lattice*, *New Journal of Physics* **14**, 073020 (2012) (see p. 61).
- [195] J. Söding, D. Guéry-Odelin, P. Desbiolles, F. Chevy, H. Inamori, and J. Dalibard, *Three-Body Decay of a Rubidium Bose–Einstein Condensate*, *Applied Physics B* **69**, 257 (1999) (see p. 63).
- [196] C.-L. Hung, X. Zhang, N. Gemelke, and C. Chin, *Accelerating Evaporative Cooling of Atoms into Bose-Einstein Condensation in Optical Traps*, *Phys. Rev. A* **78**, 011604 (2008) (see pp. 63, 65, 66).
- [197] T. Mežnaršič, T. Arh, J. Brence, J. Pišljarič, K. Gosar, Ž. Gosar, R. Žitko, E. Zupanič, and P. Jeglič, *Cesium Bright Matter-Wave Solitons and Soliton Trains*, *Phys. Rev. A* **99**, 033625 (2019) (see p. 64).
- [198] Y. Wang et al., *Hybrid Evaporative Cooling of ^{133}Cs Atoms to Bose-Einstein Condensation*, *Optics Express* **29**, 13960 (2021) (see p. 64).
- [199] X. Zhang, *Observation of Quantum Criticality with Ultracold Atoms in Optical Lattices*, PhD thesis, University of Chicago (2012) (see p. 66).
- [200] S. Giorgini, L. P. Pitaevskii, and S. Stringari, *Condensate Fraction and Critical Temperature of a Trapped Interacting Bose Gas*, *Phys. Rev. A* **54**, R4633 (1996) (see p. 68).
- [201] G. Baym, J.-P. Blaizot, M. Holzmann, F. Laloë, and D. Vautherin, *The Transition Temperature of the Dilute Interacting Bose Gas*, *Phys. Rev. Lett.* **83**, 1703 (1999) (see p. 68).
- [202] P. Arnold and G. Moore, *BEC Transition Temperature of a Dilute Homogeneous Imperfect Bose Gas*, *Phys. Rev. Lett.* **87**, 120401 (2001) (see p. 68).
- [203] L. Feng, *Coherent Nonequilibrium Many-Body Dynamics in Driven Bose Condensates*, PhD thesis, University of Chicago (2019) (see p. 69).
- [204] C. R. Cabrera Córdova, *Quantum Liquid Droplets in a Mixture of Bose-Einstein Condensates*, PhD thesis, Universitat Politècnica de Catalunya (2018) (see p. 69).
- [205] P. Thomas, *Optical Dipole Potentials for Multi-Component Bose-Einstein Condensates*, MA thesis, Universität Hamburg (2017) (see p. 69).
- [206] P. A. Murthy, D. Kedar, T. Lompe, M. Neidig, M. G. Ries, A. N. Wenz, G. Zürn, and S. Jochim, *Matter-Wave Fourier Optics with a Strongly Interacting Two-Dimensional Fermi Gas*, *Phys. Rev. A* **90**, 043611 (2014) (see p. 70).
- [207] K. Hueck, N. Luick, L. Sobirey, J. Siegl, T. Lompe, and H. Moritz, *Two-Dimensional Homogeneous Fermi Gases*, *Phys. Rev. Lett.* **120**, 060402 (2018) (see p. 70).
- [208] L. Asteria, H. P. Zahn, M. N. Kosch, K. Sengstock, and C. Weitenberg, *Quantum Gas Magnifier for Sub-Lattice-Resolved Imaging of Three-Dimensional Quantum Systems*, Arxiv **2104.10089v2** (2021) (see pp. 70, 71).
- [209] M. H. Anderson, J. R. Ensher, M. R. Matthews, C. E. Wieman, and E. A. Cornell, *Observation of Bose-Einstein Condensation in a Dilute Atomic Vapor*, *Science* **269**, 198 (1995) (see p. 71).
- [210] K. B. Davis, M.-O. Mewes, M. R. Andrews, N. J. van Druten, D. S. Durfee, D. M. Kurn, and W. Ketterle, *Bose-Einstein Condensation in a Gas of Sodium Atoms*, *Phys. Rev. Lett.* **75**, 3969 (1995) (see p. 71).
- [211] C. Weitenberg, *Single-Atom Resolved Imaging and Manipulation in an Atomic Mott Insulator*, PhD thesis, Ludwig-Maximilians-Universität München (2011) (see pp. 72, 75, 76).
- [212] J. Sebby-Strabley, M. Anderlini, P. S. Jessen, and J. V. Porto, *Lattice of Double Wells for Manipulating Pairs of Cold Atoms*, *Phys. Rev. A* **73**, 033605 (2006) (see p. 73).
- [213] S. Fölling, S. Trotzky, P. Cheinet, M. Feld, R. Saers, A. Widera, T. Müller, and I. Bloch, *Direct Observation of Second-Order Atom Tunnelling*, *Nature* **448**, 1029 (2007) (see p. 73).

- [214] G. Gauthier, T. A. Bell, A. B. Stilgoe, M. Baker, H. Rubinsztein-Dunlop, and T. W. Neely, *Chapter One - Dynamic High-Resolution Optical Trapping of Ultracold Atoms*, *Advances In Atomic, Molecular, and Optical Physics* **70**, edited by L. F. Dimauuro, H. Perrin, and S. F. Yelin, 1 (2021) (see p. 73).
- [215] S. M. Mansfield and G. S. Kino, *Solid Immersion Microscope*, *Applied Physics Letters* **57**, 2615 (1990) (see p. 73).
- [216] R. Yamamoto, J. Kobayashi, T. Kuno, K. Kato, and Y. Takahashi, *An Ytterbium Quantum Gas Microscope with Narrow-Line Laser Cooling*, *New Journal of Physics* **18**, 023016 (2016) (see pp. 73, 74).
- [217] G. Morigi, J. Eschner, and C. H. Keitel, *Ground State Laser Cooling Using Electromagnetically Induced Transparency*, *Phys. Rev. Lett.* **85**, 4458 (2000) (see p. 73).
- [218] K. Kwon, K. Kim, J. Hur, S. Huh, and J.-y. Choi, *Site-Resolved Imaging of Bosonic Mott Insulator of ^7Li Atoms*, arXiv:2111.15188 [cond-mat, physics:quant-ph], arXiv:2111.15188 [cond-mat, physics:quant-ph] (see p. 74).
- [219] Y. Miroshnychenko, D. Schrader, S. Kuhr, W. Alt, I. Dotsenko, M. Khudaverdyan, A. Rauschenbeutel, and D. Meschede, *Continued Imaging of the Transport of a Single Neutral Atom*, *Optics Express* **11**, 3498 (2003) (see p. 74).
- [220] K. D. Nelson, X. Li, and D. S. Weiss, *Imaging Single Atoms in a Three-Dimensional Array*, *Nat. Phys.* **3**, 556 (2007) (see pp. 74, 75).
- [221] P. Mouroulis and J. Macdonald, *Geometrical Optics and Optical Design*, Vol. 7, Oxford Series in Optical and Imaging Sciences (Oxford University Press, 1997) (see p. 81).
- [222] J. E. Harvey and C. Ftaclas, *Diffraction Effects of Telescope Secondary Mirror Spiders on Various Image-Quality Criteria*, *Applied Optics* **34**, 6337 (1995) (see p. 81).
- [223] CVI Melles Griot, *Technical Guide, Ch. 2, Gaussian Beam Optics*, tech. rep. (CVI Melles Griot) (see p. 81).
- [224] F. Orieux, J.-F. Giovannelli, and T. Rodet, *Bayesian Estimation of Regularization and Point Spread Function Parameters for Wiener–Hunt Deconvolution*, *JOSA A* **27**, 1593 (2010) (see p. 83).
- [225] W. H. Richardson, *Bayesian-Based Iterative Method of Image Restoration**, *JOSA* **62**, 55 (1972) (see p. 83).
- [226] L. B. Lucy, *An Iterative Technique for the Rectification of Observed Distributions*, *The Astronomical Journal* **79**, 745 (1974) (see p. 83).
- [227] L. R. B. Picard, M. J. Mark, F. Ferlino, and R. van Bijnen, *Deep Learning-Assisted Classification of Site-Resolved Quantum Gas Microscope Images*, *Measurement Science and Technology* **31**, 025201 (2019) (see p. 85).
- [228] S. Häfele, *Tbd*, MA thesis, Ludwig-Maximilians-Universität München (2022) (see p. 86).
- [229] J. Bibo, I. Lovas, Y. You, F. Grusdt, and F. Pollmann, *Fractional Corner Charges in a Two-Dimensional Superlattice Bose-Hubbard Model*, *Phys. Rev. B* **102**, 041126 (2020) (see p. 89).
- [230] E. Altman, W. Hofstetter, E. Demler, and M. D. Lukin, *Phase Diagram of Two-Component Bosons on an Optical Lattice*, *New Journal of Physics* **5**, 113 (2003) (see p. 90).
- [231] D. Rossini and R. Fazio, *Phase Diagram of the Extended Bose–Hubbard Model*, *New Journal of Physics* **14**, 065012 (2012) (see p. 90).
- [232] I. Dimitrova, N. Jepsen, A. Buyskikh, A. Venegas-Gomez, J. Amato-Grill, A. Daley, and W. Ketterle, *Enhanced Superexchange in a Tilted Mott Insulator*, *Phys. Rev. Lett.* **124**, 043204 (2020) (see p. 90).
- [233] F. Meinert, M. Knap, E. Kirilov, K. Jag-Lauber, M. B. Zvonarev, E. Demler, and H.-C. Nägerl, *Bloch Oscillations in the Absence of a Lattice*, *Science* **356**, 945 (2017) (see p. 90).
- [234] W. Alt, D. Schrader, S. Kuhr, M. Müller, V. Gomer, and D. Meschede, *Single Atoms in a Standing-Wave Dipole Trap*, *Phys. Rev. A* **67**, 033403 (2003) (see p. 91).
- [235] C. Tuchendler, A. M. Lance, A. Browaeys, Y. R. P. Sortais, and P. Grangier, *Energy Distribution and Cooling of a Single Atom in an Optical Tweezer*, *Phys. Rev. A* **78**, 033425 (2008) (see p. 91).

Acknowledgement

I imagine few work experiences are as technically diverse as setting up a new ultra cold quantum gas experiment. I would like to thank the people that have enabled this experience and made it so enjoyable.

Immanuel and Monika for giving me the opportunity to set up a new experiment, even though I had no prior experience in quantum gases. For allowing me to pursue things that are not always relevant to problems we had in the lab. Immanuel for letting me be a part of this group, where everyone is curious, excited and eager to share their knowledge.

The Caesium team, most notably Cesar, Hendrik, Monika, Christian, Julian, and Alex but also the many master and Hiwi students that helped set up the experiment. Cesar for his many ideas on how to proceed in the experiment and for the many beers we shared. Monika, Cesar and Hendrik for patiently explaining things to me, that to them appeared intuitively obvious, and for forcing me to realize that what is obvious to me, it often not so clear and may even be wrong. Hendrik for the many things he taught me about electronics and computers and for the exciting time I had while designing and setting up the experiment. Julian and Cesar for infecting me with their excitement for the things we did in the experiments. Alex and Hendrik for their attention to the critical details, that I tend to gloss over.

My colleagues at the LMU and MPQ for sharing know-how and equipment with me, most notably FermiII, which have an apparently endless supply of lenses to choose from. Bodo, Olivia and Karsten for their support in solving the small and large electronics problems I encountered in the lab. Bodo for his insistence, that I understand the solutions he suggested to those problems, and taking the time to ensure that this is the case. Anton for help and guidance in the mechanical design of our experiment, which probably would never have been assemble-able without his vast experience. Ildiko and Kristina for the administrative support, and their patience with me. The LMU and MPQ workshop for the many small and not-so-small components they milled for the lab.

Alex, Julian, Cesar, Monika and Hendrik for proof reading this thesis.

Christoph, Karen, Julian, Simon and Guillaume for going running with me through the English garden in (almost) any weather. Simon and Leo for inviting me to go climbing and other activities. My family and friends for their support.